Doctoral Thesis

Quantum Emitters for Sensing and Sub-Diffraction Imaging

A thesis submitted in fulfilment of the requirements

for the degree of Doctor of Philosophy

School of Mathematics and Physical Sciences

University of Technology Sydney

Author

Mehran Kianinia

Supervisors

A. Prof. Charlene Lobo

Prof. Milos Toth

Prof. Igor Aharonovich

June 2018

Certificate of Original Authorship

I, Mehran KIANINIA, certify that the work in this thesis titled, 'Quantum Emitters for Sensing and Sub-Diffraction Imaging ' has not previously been submitted for a degree nor has it been submitted as part of requirements for a degree except as fully acknowledged within the text.

I also certify that the thesis has been written by me. Any help that I have received in my research work and the preparation of the thesis itself has been acknowledged. In addition, I certify that all information sources and literature used are indicated in the thesis.

This research is supported by an Australian Government Research Training Program Scholarship.

Signature of Student: Production Note: Signature removed prior to publication.

Date: 12 June 2018

Acknowledgements

The work presented in this dissertation was carried out under the supervision of Associate Professor Charlene Lobo, Professor Milos Toth and Professor Igor Aharonovich at the School of Mathematical and Physical Sciences, University of Technology Sydney, New South Wales, Australia. I sincerely wish to thank them, for their invaluable guidance and support during my PhD study. They provide me an exceptional opportunity for research, scientific discussions, career development and learning in an enjoyable environment.

Dr. Olga Shimoni helped me with her expertise in Bio-Chemistry . I am grateful to Associate Professor Mike Ford, Dr. Carlo Bradac, Dr. Sejeong Kim, Dr. Zaiquan Xu and Dr. Trong Toan Tran. I appreciate technical supports and training from Mrs. Katie McBean, Mr. Geoff McCredie, Mr. Herbert Yuan and Mr. Mark Berkahn.

Valuable knowledge from external Collaborators Dr. Andreas W. Schell from Tokyo University, Bernd Sontheimer from Humboldt University of Berlin particularity improved the quality of the works. Dr. Avi Bendavid from CSIRO measured and analyzed the XPS data presented in chapter 4.

Many thanks to all of my fellow research students and colleagues in the MAU for their contributions, discussions and encouragement. Your friendship made my time at UTS unforgettable. An special thanks to Olivier for assisting me with the proof reading.

Finally I wholeheartedly thank my family for their generous and steadfast support from miles away.

This research was supported by an Australian Government Research Training Program Scholarship and FEI Company.

To the many people that I've mostly likely forgotten thank you too.

Contributing Publications

Publications that contributed to this work:

- Robust, directed assembly of fluorescent nanodiamonds, **M. Kianinia**, O. Shimoni, A. Bendavid, A. W. Schell, S. J. Randolph, M. Toth, I. Aharonovich, C. J. Lobo. In: *Nanoscale*, 8 (2016), pp. 18032-18037.

- Robust Solid-State Quantum System Operating at 800 K, **M. Kianinia**, B. Regan, S. A. Tawfik, T. T. Tran, M. J. Ford, I. Aharonovich, M. Toth. In: *ACS Photonics*, 4.4 (2017), pp. 768–773.

- Super-resolution imaging of quantum emitters in layered materials, **M. Kianinia**, C. Bradac, B. Sontheimer, F. Wang, T. T. Tran, M. Nguyen, S. Kim, Z. Xu, D. Jin, A. W. Schell, C. Lobo, I. Aharonovich, M. Toth. In: *Nature Communications*, (2018).

- Attachment of nano-objects to beam-deposited structures, **M. Kianinia**,Olga Shimoni, Igor Aharonovich, Charlene Lobo, Milos Toth, Steven Randolph, Clive D Chandler. U.S. Patent Application 15/188862, (2017).

Publications not featured in this work containing research undertaken during the PhD program:

- First-principles investigation of quantum emission from hBN defects, Sherif AbdulkaderTawfik , Sajid Ali, Marco Fronzi, **Mehran Kianinia**, Toan Trong Tran, Catherine Stampfl, Igor Aharonovich, Milos Toth and Michael J Ford. In: *Nanoscale*, 9 (2017), pp. 13575-13582.

- Resonant excitation of quantum emitters in hexagonal boron nitride, Toan Trong Tran, **Mehran Kianinia**, Minh Nguyen, Sejeong Kim, Zai-Quan Xu, Alexander Kubanek, Milos Toth and Igor Aharonovich. In: *ACS Photonics*, (2017).

- Single Photon Emission from Plasma Treated 2D Hexagonal Boron Nitride,Zai-Quan Xu, Christopher Elbadawi, Toan Trong Tran, **Mehran Kianinia**, Timothy B Hoffman, Minh Nguyen, Sejeong Kin, James H Edgar, Ziaojun Wu, Li Song, Sajid Ali, Mike Ford, Milos Toth and Igor Aharonovich. In: *Arxiv*, (2017), arXiv:1710.07010.

- Optical properties of implanted Xe color centers in diamond, Russel Sandstrom, Li ke, Aiden Martin, Ziyu Wang, **Mehran Kianinia**, Ben Green, Weibo Gao and Igor Aharonovich. In: *Optics Communications*, 411 (2018), pp.182-186.

- Nanoassembly of quantum emitters in hexagonal boron nitride and gold nanospheres, Minh Nguyen, Sejeong Kim, Toan Trong Tran, Zai-Quan Xu, **Mehran Kianinia**, Milos Toth, and Igor Aharonovich. In: *Nanoscale*, 10 (2018), pp. 2267-2274.

- Nanodiamonds with photostable, sub-gigahertz linewidths quantum emitters, Toan Trong Tran, **Mehran Kianinia**, Kerem Bray, Sejeong Kim, Zai-Quan Xu, Angus Gentle , Bernd Sontheimer, Carlo Bradac and Igor Aharanovich. In: *APL Photonics*, 2 (2017), pp 116103-116112.

Conference presentations

- **M. Kianinia**, et al. "*Robust, directed assembly of fluorescent nanodiamonds*", In: Conference on Optoelectronic and Microelectronic Materials and Devices (COMMAD), 2016, Sydney, Australia.

- **M. Kianinia**, et al, "Quantum emitters in flattland", In: The 8th International Conference on Metamaterials, Photonic Crystals and Plasmonics (META), 2017, Incheon, South Korea.

- **M. Kianinia**, et al. "*Robust, directed assembly of fluorescent nanodiamonds*", In: The 11th Conference on New Diamond and Nano Carbons (NDNC), 2017, Cairns, Australia.

Abstract

A quantum system with discrete, resolvable energy levels is an ideal system for sensing applications, taking into account that it can strongly interact with its environment. Although the strong response with the target properties such as magnetic or electric field is ideal, it can be a disadvantage when the system is interacting with other physical changes (noise) at the same time. However, the benefits of the strong coupling as well as small size of the sensor has motivated many researchers to explore quantum systems for measuring very small physical quantities. For instance, Nitrogen vacancy center in diamond is a unique quantum system enabling sensing of magnetic field from single molecules or electrons at room temperature.

This thesis has focused on two different quantum emitters: NV centers in nanodiamonds and quantum emitters in hexagonal Boron Nitride (hBN). In the first part a new assembly technique based on electron beam induced deposition and crosslinking chemistry is developed. It is demonstrated that fluorescent nanodiamonds containing NV centers can be assembled into arrays of various size and shapes on any substrate. The produced array is ideal for device fabrication due to its outstanding robustness. A potential application of such arrays as magnetic field sensor with high spatial resolution is shown.

The superior properties of quantum emitters in hBN has been studied in the second part of this thesis, where is has been shown that these emitters are not only stable but also maintain their single photon purity at elevated temperature. The highest measured quantum emission at 800 K in this study is the highest reported temperature for a quantum emitter so far, makes them a suitable candidate for temperature sensing. In addition, the level structure of emitters in hBN has been investigated in detail which reveals the unique photophysical properties of a class of these emitters which result in a nonlinear increase in the emission upon co-excitation with two lasers of different wavelength. Finally the photophysic property of these emitters has been employed to introduce a new modality of super-resolution microscopy with resolution down to about 70 nm. These findings will extend our understanding of

quantum emitters in hBN and introduce a new functionality for them which paves the way toward their application in biology and sensing.

Contents

List of Figures

Abbreviations

AFM	Atomic Force Microscope
BSE	Backscattered Electron
QD	Quantum Dot
SQUID	Superconducting Quantum Interference Device
LED	Light Emitting Diode
CVD	Chemical Vapour Deposition
ODMR	Optically Detection Magnetic Resonance
SE	Secondary Electrons
EBID	Electron Beam Induced Deposition
EBIE	Electron Beam Induced Etching
OES	Optical Emission Spectroscopy
RIE	Reactive Ion Etching
ESEM	Environmental Scanning Electron Microscope
MFC	Mass Flow Controller
FCC	Fluorescence Cross Correlation
RESOLFT	Reversible Saturable Optical Linear Fluorescence Transitions
CW	Continuous Wave
ISC	Inter System Crossing
PSF	Point Spread Function
RF	Radio Frequency
NMR	Nuclear Magnetic Resonance
NV	Nitrogen-Vacancy

NV^0	Neutral Nitrogen-Vacancy
NV^-	Negative Nitrogen-Vacancy
PL	Photoluminescence
MW	MicroWave
NA	Numerical Aperture
SCCM	Standard Cubic Centimeters per Minute
STED	Stimluated Emission Depletion
GSD	Ground State Depletion
ZPL	Zero Phonon Line
SPS	Single Photon Source
DFT	Density Functional Theory
EDC	1-ethyl-3-(3-dimethylaminopropyl)carbodiimide hydrochloride
NHS	N-hydroxysuccinimide
FWHM	Full Width Half Maximum
TMP	Turbo Molecular Pump
CNT	Carbon NanoTube
RT	Room Temperature
APD	Avalanche Photo-diode
HBT	Hanbury Brown and Twiss
TCSPC	Time Correlated Single Photon Counting

Chapter 1

Introduction

1.1 Quantum emitters for sensing and imaging

Quantum sources – emitters with sub poissonian emission – are at the center of extensive research in the field of quantum optics. These include quantum dots (QDs) and solid-state emitters for instance color centers in diamonds, point defects in silicon carbide, zinc oxide and hexagonal boron nitride. An emerging application of these emitters in quantum computers and quantum cryptography is hindered through their sensitivity to the local environment such as electric or magnetic field. Hence the need for an ideal emitter is the main focus of many studies. Conversely, the strong interaction of the quantum emitters with their environment is a great potential for sensing very weak physical quantities.

Quantum sensors are a quantum system with discrete, resolvable energy levels which can be initialized and read out [1]. In general, the coherent manipulation of the quantum system reveals its interaction with the external field through shift in its energy levels. In addition, one of the most important property of any sensor is its sensitivity. Quantum sensors are expected to provide strong response to the target physical properties (Signal) while the undesired response to other physical quantities (noise) should be minimal. The main benefit of using a quantum system

as a sensor other than their enhanced sensitivity, is coming from the nanometer size of the quantum system which make it possible to bring the sensor to a very close distance of the source or resolve the physical quantity spatially. A large variety of systems such as Atomic vapors [2], Trapped ions [3], NV centers in diamonds [4] and SQUIDs (Superconducting quantum interference device) [5] can be classified in the definition of quantum sensors.

On the other hand, acquiring the exact location of the quantum sensor is one of the challenges in this field. For quantum emitters this can be done optically but not better than the diffraction limit ($\sim$ 200 nm). Electric microscopes or scanning probe microscopy techniques are capable of producing high resolution images (down to few nanometers), However, in some field such as biology, optical imaging has remained the exclusive technique due to its ability of producing 3D images. On the other hand, Optical illumination of fluorophores in biological samples will produce reactive oxygen species which results in phototoxicity to the living cells. The amount of these species depends on illumination dose and the photochemical properties of fluorophores [6]. In addition, still the resolution of optical techniques are limited, restricting many researches in the field. Among various schemes to overcome optical resolutions, super-resolution microscopy (all optical microscopy beyond diffraction limit) based on fluorescent materials holds a great promise, attracting the attention of many researchers in the field [7]. Although the concepts for super-resolution imaging are well established, exploring different fluorescent systems will help deepen our understanding of the physics and possibility of new applications.

1.2 Aims and motivations

The focus of this thesis is on solid state quantum emitters based on NV centers in diamond and single photon sources in hexagonal boron nitride (hBN). The wealth of previous studies on NV centers has provided the near complete understanding of electron level structures of NV centers which leads to discovery of very weak magnetic

and temperature sensing with unprecedented applications such as single-molecule structural imaging through sensing properties [8]. In this regard a reliable fabrication method, is one of the current challenges for producing scalable devices based on NV centers in diamond. On the other hand, the recent discovery of luminescence point defects in hBN revealed their promising optical properties. Understanding the electronic structure and origin of the defects in hBN, is a necessary information for using them in applications such as sensing. Another application of quantum emitters which does not directly fall into quantum sensing category is the possibility of high resolution imaging of the quantum emitter. This feature apart from the distinct application in bio-imaging fields, is the inevitable requirement for any nanoscale sensitivity applications where the exact location of the quantum emitter (sensor) needs to the determined.

Here, NV centers in diamond and luminescence defects in hBN are described and their properties are reviewed in chapter 2. In addition, the concept of sensing magnetic field with NV centers and current understanding of the physics are also explained. At the end of this chapter, the superresolution microscopy techniques for imaging a quantum emitter are discussed, focusing on the concepts. In chapter 3, the measurement procedures as well as fabrication techniques used in this work are pointed out. Moreover, the fundamental understanding of the measurements or fabrication techniques are included in this chapter. Experimental results and discussions are divided into three chapters: In chapter 4, the developed nanofabrication techniques for assembly of nanodiamonds are presented. It has been shown that nanodiamonds can be arranged in a desired pattern on substrate with strong bonds which makes this robust technique ideal for device fabrication where post processes after positioning of nanodiamonds are required. In addition, magnetic sensing based on produced pattern has been demonstrated. Next, the robust emission from emitters in hBN above room temperature up to 800 K is reported in chapter 5 following with a discussion of the effect of temperature on emission properties. Specifically the study is not only to explore emitters in hBN as a quantum system for sensing high temperature but proposing the suitability of hBN for application above room

temperatures which is a working condition for most devices today. Finally, chapter 6 includes extensive studies of photophyscial properties of quantum emitters in hBN. This study, revealed the nonlinear optical properties in hBN which enables the new modality of super-resolution microscopy. Furthermore, these fundings provides control over blinking of the emitters in hBN with potential application for instance in coherent manipulation of these emitters. Finally, a summary of the achievement in this thesis as well as future directions for the following works are presented in chapter 7.

Chapter 2

Quantum sensing and Imaging

2.1 Solid state quantum emitters

Optically active defects in solids are a vital part of numerous technologies spanning light emitting diodes (LEDs) [9][10], lasers [11][12], sensors[13] and communications[14]. Among them, single photon sources (SPSs) which produce non classical light stand out in the sense that they can emit stream of individual photons. Hence, over the last decade, research into solid state single photon sources (SPSs) – quantum dots (QDs) and color centers – has accelerated dramatically. Quantum dots mostly operate only at cryogenic temperatures because of low carrier binding energies and thermal ionization at elevated temperatures[15][16]. On the other hand, color centers in solids (defects and impurities, also known as artificial atoms) often have deep electronic states that enable SPS operation near room temperature (RT). These impurities, if stable inside the solid matrix, will introduce narrow levels within the bandgap of host crystal. Relaxation from excited state of the defect may produce a characteristic, sharp zero phonon line (ZPL) which is broadened due to transitions to upper electronic-phonon ground states. Often, phonon sidebands are produced upon interaction of transitions in the impurity with lattice. Transitions in the impurity manifold can also exchange momentum with the lattice giving rise to

phonon sidebands. The emitted light can be externally collected if it is not absorbed by the host crystal- i.e. the gap energy is larger than the transition. Examples of SPSs in solids include Nitrogen-Vacancy (NV)[17], Silicon-Vacancy (SiV)[18] centers in diamond, point defects in silicon carbide (SiC)[19] and zinc oxide (ZnO)[20] as well as SPSs in carbon nanotubes (CNT)[21] and hexagonal boron nitride (hBN)[22]. The most studied defect is NV center in diamond which is discussed in detail later in 2.2. The possibility of controlling and reading the electron spins in this system has attracted a lot of researches and has resulted in fascinating applications in quantum computations and quantum sensing. On the other hand SPSs in hBN are promising candidates which have only been discovered recently.

The exploration of nanophotonic phenomena in 2D systems using materials such as transition metal dichalcogenides (TMDCs), phosphorene and hexagonal boron nitride (hBN) has been gaining momentum in recent years [23][24][25][26][27]. Localized nanoscale effects, including radiative decay of interlayer excitons and single photon emission from deep trap-point defects, are particularly interesting and important[28]. The latter, for instance, is key to the practical deployment of scalable, on-chip quantum photonic devices [29]. One of the promising 2D materials, is hBN which can host single photon emitters with bright, fully polarized and photostable emission at room temperature [30] which have a potential to transform applications in sensing and imaging. The current understanding on these sources have been explained in details later in 2.3

2.2 NV centers in diamond

Diamond is a wide bandgap insulator which hosts more than 500 optical centers with luminescence signals from deep ultra violet (UV) to the infrared, originating from various defects and impurities within its crystallographic lattice [31]. Nitrogen is the most common impurity in diamond, particularly because it has a similar atomic size as carbon and is often present during the growth of diamond. Nitrogen

generally appears as a substitutional atom and creates a distortion along the (111) axis with the neighboring carbon atom [32]. NV centers will form when one nitrogen atom resides next to a missing carbon in diamond lattice in a C_{3v} symmetry. The structure of NV center in diamond has been shown in figure 2.1(a). The NV center has two charge states: the negatively charged center (NV^-) with a zero phonon line (ZPL) centered at 637 nm and a neutral center (NV^0) with a ZPL centered at 575 nm[33]. Since only negatively charged state of this defect has been used for sensing applications such as magnetometry[34], this thesis will only focus on NV^- which will be denoted as NV defect for simplicity. Figure 2.1(b) shows a typical PL spectrum of NV defect with phonon side band which is extended to 800 nm. The phonon side band is the result of interaction with the phonons in the diamond crystal.

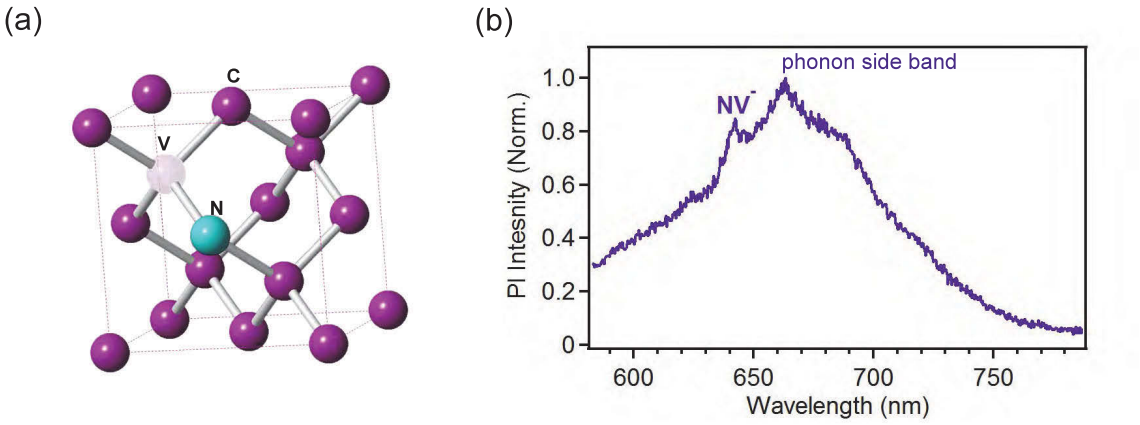

FIGURE 2.1: (a) Crystallography structure of diamond consisting substitutional Nitrogen (blue) next to a vacancy (V). (b) Room-temperature PL spectrum of negatively charged NV centers in diamond with ZPL at 637 nm and prominent phonon side band extending to 800 nm.

NV centers are unambiguously the most studied color center in diamond. Their unique optical and spin properties coupled with the excellent thermal, electrical and mechanical properties of the diamond host, has not only put NV centers at the center of research in quantum computing [35][36] and communication [37][38] but extended their application in quantum sensing [39] and as markers in biology [40][41]. The wide bandgap of (5.5 eV) prevents absorption in large range from ultra-violet to infra-red and the thermal conductivity of diamond provide efficient heat transfer

between the NV center and environment. Most of the superior optical properties of NV center directly arise from its electronic structure shown in figure 2.2. Maximum photon absorption occurs at 575 nm for this center [42], results in excitation of the electron into excited state and release of a single photon at room temperature upon decaying to the ground state.

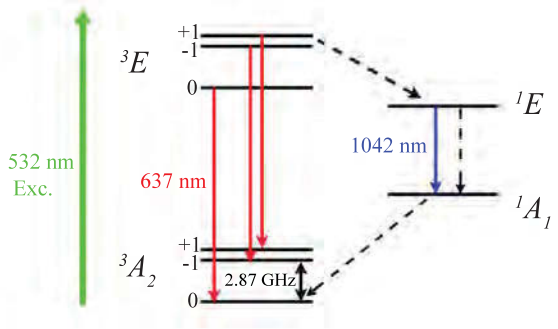

FIGURE 2.2: The ground and excited states are spin-triplets denoted as 0, -1 and +1 corresponding to $m_S = 0$, $m_S = -1$ and $m_S = +1$ respectively. Solid arrows shows radiative transitions with 637 nm (red) as ZPL for NV$^-$. Dashed arrows are non-radiative transitions from excited state (^3E) into ground state ($^3A_2$) though metastable states (^1E and $^1A_1$). Reproduced from [43]

Most importantly the ground state of NV center $^3A_2$ is spin triplet. It is consist of a singlet $m_s = 0$ and a doublet $m_s = \pm 1$ which are separated by 2.87 GHz in the absence of external magnetic field (figure 2.2) owing to the magnetic dipole interaction between the two unpaired electrons [44]. Excited state ^3E is also a triplet similar to ground state where the defect can optically be excited into, through spin conserved transitions ($\Delta m = 0$). PL emission is the result of direct relaxation into ground state, however NV center can also relax non-radiatively through metastable states ^1E and ^1A as indicated by black dashed-arrows in figure (2.2)[43]. The transition into ^1E is spin selective and as a result the rate from $m_s = 0$ into ^1E is much lower compared to transitions from $m_s = \pm 1$. The consequence of lower transitions into non-radiative pathway, is higher brightness in PL when the NV center is excited from $m_s = 0$ in the ground state which means the PL emission of the NV center contains the information regarding the spin of the electron. Now, when applying a resonant

microwave field of 2.87 GHz, the spin of the electron is changed by driving it from $m_s = 0$ into $m_s = \pm 1$ which also results in significant reduction of PL intensity ($\sim 30\%$) also known as Optically Detected Magnetic Resonance (ODMR)[45][34] (figure 2.3(a)). In addition the non-radiative pathway plays a crucial role in spin dynamics of NV center by initializing it into $m_s = 0$. This outstanding property in NV centers is preserved at room temperature. Although this effect has been reported in other systems such as silicon vacancies in SiC , at room temperature, NV centers perform best.

2.2.1 Quantum sensing with NV centers

Beside using nanodiamonds as fluorescent labels in biology applications [46], the ODMR in NV centers has been extensively applied for detecting magnetic field [47][4]. The Zeeman splitting of $m_s = \pm 1$ is sensitive enough to measure very weak magnetic fields from molecules or an electron by bringing the NV center in close proximity considering the comparable size of the sensor (here NV center in diamond)[47]. Figure 2.3(a) shows a typical ODMR measurement with a single NV center in an increasing external magnetic field. In the absence of external magnetic field, there is a dip in fluorescence when the microwave field at 2.87 GHz drives electron from $m_s = 0$ into $m_s = \pm 1$. Upon applying the magnetic field the $m_s = \pm 1$ sublevels are split into different energies with respect to Zeeman splitting of the sublevels, leading into appearance of two dips in the ODMR spectrum denoted by ω_1 and ω_2 in figure 2.3(a). By neglecting the interactions with nearby nuclear spins in the diamond lattice, the ground state spin Hamiltonian of the NV defect is the sum of zero-field and Zeeman terms:

$$H = h[DS_Z^2 + E(S_x^2 - S_y^2)] + g\mu_B B.S \tag{2.1}$$

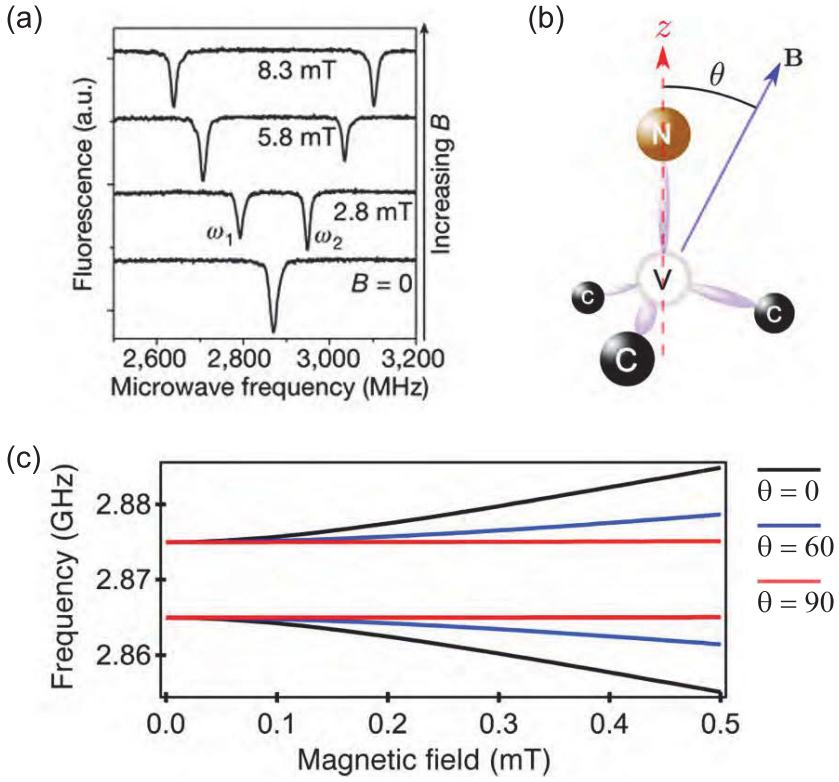

FIGURE 2.3: (a) Scanning of microwave field produces a dip in fluorescence of NV center at 2.87 GHz. Applying an external magnetic field causes Zeeman splitting and changes the ODMR spectrum. Reproduced from [48]. (b) A magnetic field which is applied with angle of θ relative to the z axis of the NV center. (c) Effect of different magnetic field alignment θ with respect to NV axis. Reproduced from [34].

Where z is quantization axis along NV defect, h is Plank constant, D and E are zero-splitting parameters, S_x, S_y and S_z the Pauli matrices, $g \simeq 2$ the Landé g-factor and μ_B the Bohr magneton. D parameter along the z axis of NV center is calculated to be about 2.87 GHz due to the spin-spin interactions of unpaired electrons (figure 2.3(b)). It is also very susceptible to local temperature. In the presence of strain in the diamond matrix, the off-axis zero field splitting E will also affect the splitting of ground state sublevels. It can be as high as 100 MHz in high purity bulk diamond while reduces to few MHz in nanodiamonds [34]. Furthermore, while the presence of external magnetic field cause spliting of the NV center sublevels, the direction of magnetic field relative to the NV axis is also very important. Figure

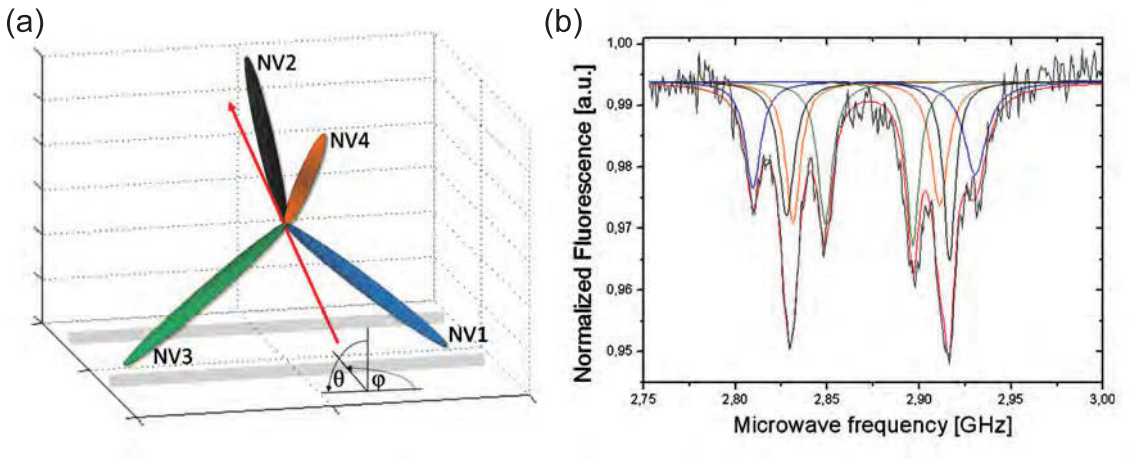

FIGURE 2.4: (a) Four possible orientations of NV centers in the diamond lattice result in different angles between the applied magnetic field and NV axis. (b) ODMR spectrum upon applying $B = 2.7\ mT$ in the direction of red arrow. Reproduced from [49].

2.3(c) demonstrates the theoretical calculation of Zeeman splitting in NV centers when magnetic field is applied in different angles (θ) relative to the NV axis. The maximum splitting occurs when the external magnetic field is applied in parallel (black) to the NV axis. If the external magnetic field is not parallel to the NV axis (blue) the splitting is reduced. However, when the magnetic field is perpendicular to the NV axis (red) there is no effect on Zeeman splitting specially at weak magnetic fields [34].

While so far a single NV defect was used to described the ODMR in diamond, ensembles of NV defects can also be used for detecting magnetic fields. In this case higher magnetic sensitivity is expected due to the amplified fluorescence signal. However, complex structures will appear in the spectrum in the presence of external magnetic fields. As NV centers are aligned randomly into 4 different orientation along (111) crystallographic direction in diamond lattice, applying magnetic field in certain direction, will lift degeneracy of $m_s = +1$ and -1 with different amount for each direction of NV leading to appearance of these complex structures in the ODMR spectrum (figure 2.4(a)). An example of these structures has been shown in figure 2.4(b)[49][50].

2.2.2 Nanofabrication techniques for assembly of nanodiamonds

Assembling fluorescent nanoparticles into macroscopic arrays is required for many applications spanning sensing, photonics, plasmonics and quantum information processing[51][51][52]. Positioning of NV-centers one-by-one with an atomic force microscope (AFM) tip is one of the earliest attempt in assembly of nanaodiamonds and coupling to different structures. In this process, AFM in contact mode is used for manipulating of particles. In a preliminary step the sample is prepared by spin-coating an aqueous solution of diamond nanocrystals onto a glass coverslips. With the help of the AFM tip nanodiamonds can be rotated or moved in desired directions. The process is shown in figure 2.5. A coupled confocal microscope and AFM is needed for optical measurements and nanoscale manipulations. Although the technique provides precise control over the position of nanodiamond, the process is slow and it is limited to only one particle movement which makes it a time consuming technique for fabrication of multiple devices [53].

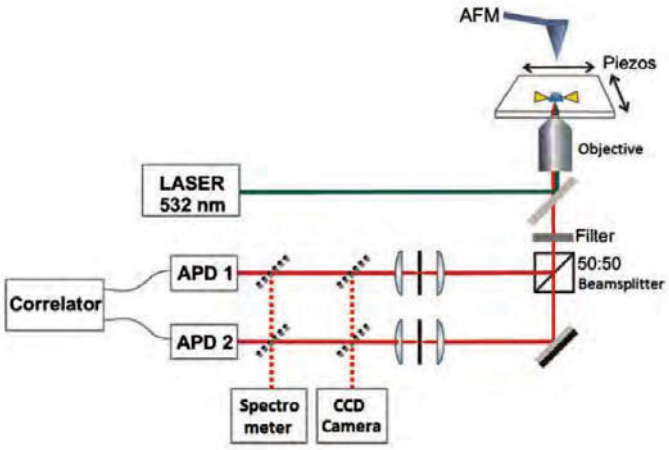

FIGURE 2.5: A confocal setup coupled with and AFM stage enables the manipulation of the NV centers with in situ photoluminescence measurement of the center. Reproduced from [53].

Other techniques for assembly of nanodiamonds are based on combined electron beam lithography (EBL) and self-assembly chemistry. These techniques has been

proposed for positioning of other quantum systems such as quantum dots and has been extended to nanodiamonds [54]. For instance a recent report shows a reusable pads fabricated by EBL for electrostatic self-assembly of nanoparticles. The pads made of Al_2O_3 or other oxide are positively charged on the surface attracting the negatively charged nanoparticles such as silica-clad quantum dots. Carboxylated nanodiamonds are negatively charged on the surface and can be used in this technique [55]. Figure 2.6 shows the schematic of the assembly technique and the produced pattern with nanaodiamonds. This method is capable of positioning of single particles with low efficiency but weak interaction of the particles to pads prevent any further processing after they are positioned.

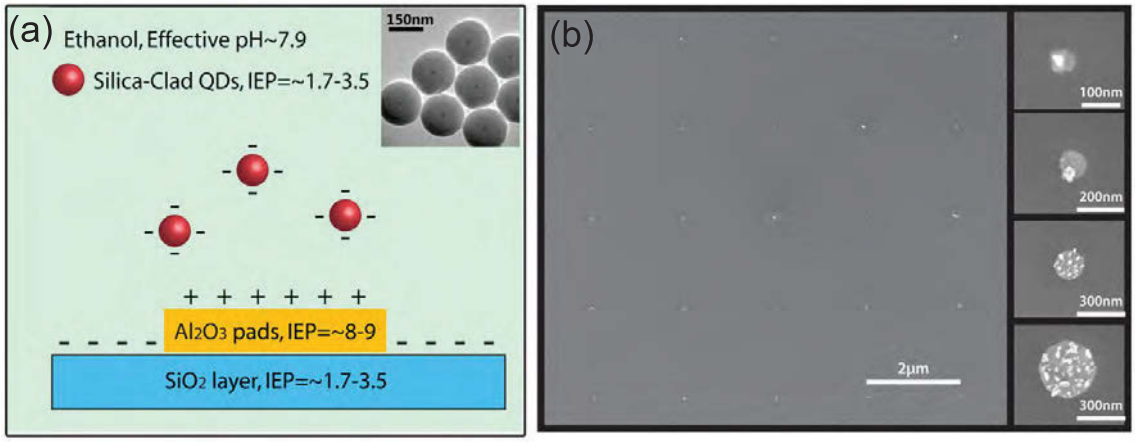

FIGURE 2.6: (a) Schematic of the process showing the negatively charges particles attracted by positively charged pads.(b) Self-assembled nanodiamonds on Al_2O_3 pads. Various number of nanodiamonds from singles to multiple may sit on the pad. Reproduced from [55]

Furthermore, specific fabrication processes such as DNA origami self-assembly for nanodiamonds have been demonstrated with nanometer precision [56]. However, these method are not suitable for positioning nanodiamond on devices and lack the robustness which is required if there is a post processing for device fabrication.

2.3 Quantum emission in hBN

Hexagonal Boron Nitride (hBN) is a Van der Waals layered crystal which belongs to the family of 2-dimensional materials. It is a wide bad gap material ($\sim$6 eV) with favorable thermal, chemical and mechanical properties. Recently a new source of single photons has been realized in hBN which has been attributed to deep trap defects in the material [30]. An example of typical photoluminescence (PL) spectrum of a single emitter in hBN is shown in figure 2.7. PL spectrum (figure 2.7(a)) consist of ZPL at 575 nm and a pronounced side peak at 625 nm. In addition Raman peak for hBN is located at 1367 cm^{-1} while the wavenumber differences between the two peaks (i.e in figure 2.7(a)) is about 1350 cm^{-1}, well close to consider the contribution of first Raman Stokes harmonic in the second peak [57]. Different part of the PL spectrum is also indicated in figure 2.7(a). The Asymmetric shape of ZPL is most probably due to the contribution of low energy phonons from hBN crystal.

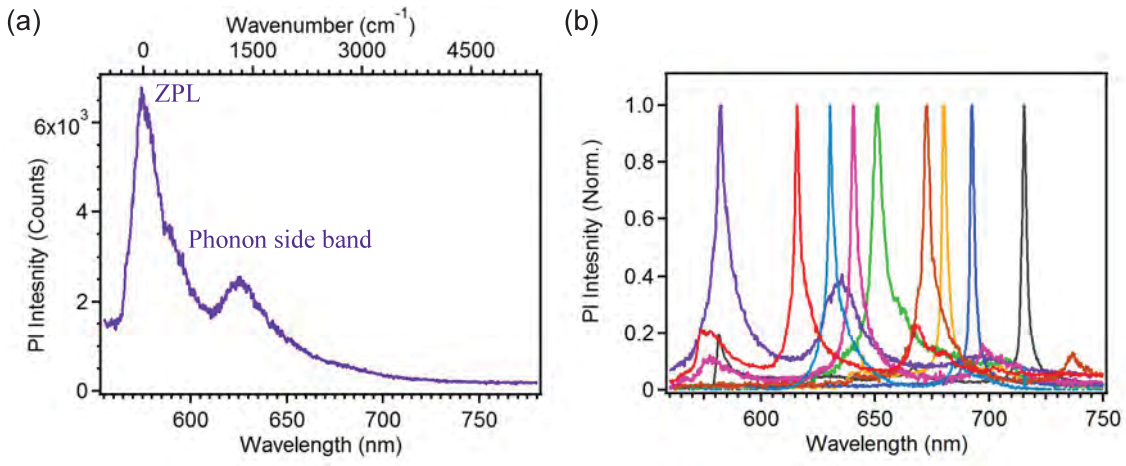

FIGURE 2.7: (a) PL spectrum from a single emitter in hBN with ZPL at 575 nm and PSB seperated at 625 nm. (b) PL spectrum of various emitters in hBN with range of ZPL from 575 to 720 nm.

Quantum emission with energies in UV and visible range has been reported for hBN [57][58][59]. Figure 2.7(b) shows PL spectra of various single emitters with different emission energies in hBN in the visible range. The origin of the defect is still under debate but theoretical studies have suggested few possibilities. In

the first demonstration of single emission from hBN monolayers, a complex defect composed of nitrogen vacancy adjacent to the anti-site nitrogen (N_BV_N) was considered as potential defect based on density function theory (DFT) considering the emission energies and fully polarized emission of the defect [30]. However, later studies bring into attention other possibilities such as B vacancies (V_B)[57], carbon anti-site (C_BV_N) [60][61].The various emission have also been attributed to different local environment of the emitters such as strain as well as different charge states [57][58][62].

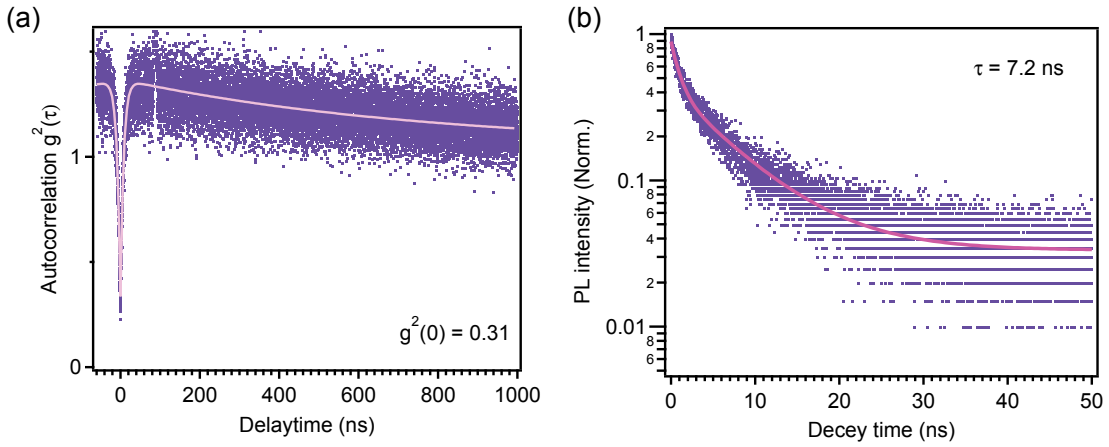

FIGURE 2.8: (a) Autocorrelation measurement from single photon source in hBN. PL spectrum of the emitter is shown in figure 2.7(a). (b) Time-resolved PL measurement of the same emitter with lifetime of 7.2 ns.

Cross correlation measurement depicted in Figure 2.8(a) with a dip of 0.31 at zero delay time proves the quantum emission of the source. Fluorescent cross correlation (FCC) is the main established technique in confocal microscopy for detecting single photon emitters [63]. The principles of the technique will be described in chapter 3.1.3. In brief, in this measurement the probability of detecting photons simultaneously on two arms of collection is evaluated. For a single photon source the probability is less than 0.5 and in ideal case is 0 which is projected in the zero delay time of autocorrelation function. As a result a dip below 0.5 is a signature of single photon source. In addition, hBN emitters usually posses long lived metastable state (μs to ms) which produces bunching at long correlation times in autocorrelation

measurement. In this regard electronic structure of single photon sources in hBN consists of 3-levels: Ground state, Excited state and Metastable state [30]. More details on the level structure of the emitters and associated dynamics will be discussed in chapter 5 and 6. Furthermore, emitters in hBN decay from excited state in few nanoseconds. For this particular emitter, time resolved PL measurement (figure 2.8(b)) indicated lifetime of about 7 ns. In addition, single photon sources in hBN are not only stable at ambient conditions but also very robust. Figure 2.9 summarizes the stability measurements on hBN emitters. Excitation with high energy lasers has been reported to induce instability in some cases. Spectrul diffusion (fluctuation in ZPL position in the PL spectrum) of around 100 nm as well as temporal blinking has been reported under excitation with 405 nm continuous laser. As the result, the near resonant excitation has been suggested to prevent blinking [64]. However, some emitters in hBN are stable even under excitation with high energy lasers (figure 2.9(a)). Figure 2.9(b) is an example of emission from a single source under continuous excitation with 532 nm (300 μW) over acquisition of 40 minutes at room temperature. Furthermore, the robustness of the emitters was investigated by annealing them in various gases environments. Annealing at 500 $^{\circ}C$ in Argon (Ar), Hydrogen (H_2), Oxygen (O_2) and ammonia (NH_3) didn't have any effect on the emission spectrum of hBN single photon source as shown in figure 2.9(c) [58].

2.3.1 Fully polarized emission from hBN

Regardless of emission energies, all single emitters in hBN have similar features, namely high brightness and fully polarized emission. The polarization measurement on emitters in hBN revealed fully polarized emission which indicates emission dipole is within the hBN flake (figure 2.10). Thanks to the 2D nature of the host material the dipole is always aligned perpendicular to the excitation and collection path and as a result polarization measurement always result in fully polarized emission [66][30][65][68]. However, this is not the case for absorption (excitation) polarization.

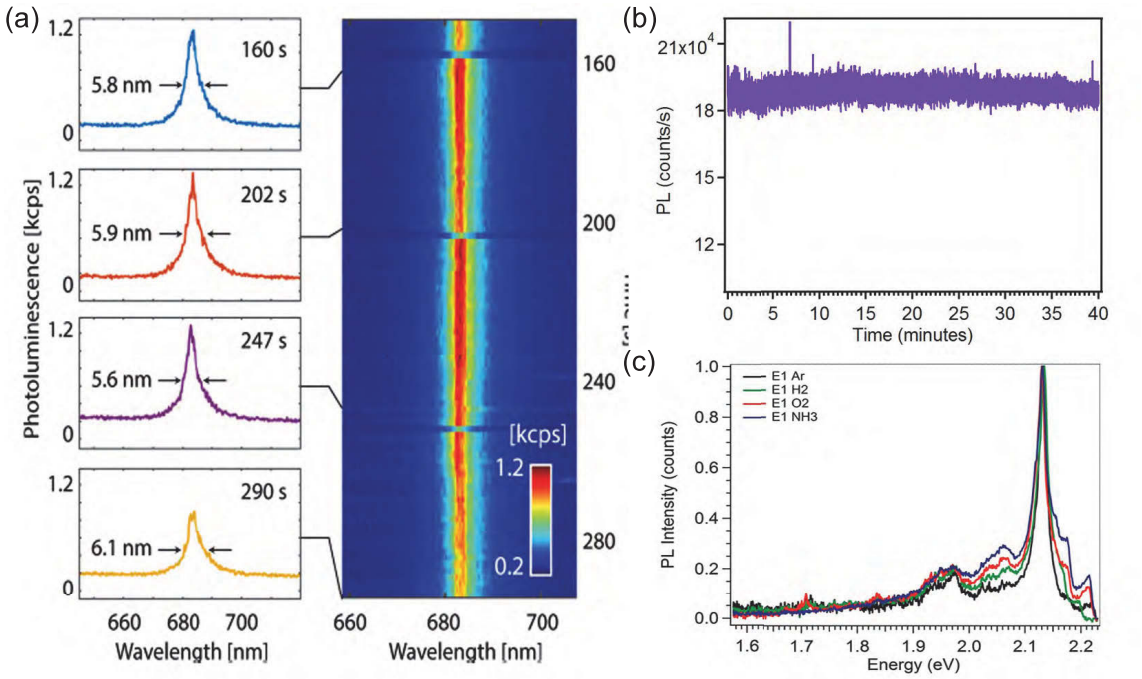

FIGURE 2.9: (a) PL emission from an emitter in hBN under continuous excitation with 405 nm laser (10 mW). The integration time per spectrum is 1 s, and the spectral resolution is 1 nm.The dark traces every 30 s are the result of periodic refocusing of the objective. Reproduced from [64]. (b) Stability of the emission from single photon source in figure 2.8 over 40 minutes under excitation with 532 nm (300 μW). (c) Robustness of single photon sources in hBN has been shown by comparing the PL spectrum of the same emitter after annealing at various environment as indicated at 500 $^{\circ}C$ for 30 minutes. Reproduced from [58].

Examples of absorption and emission polarization misalignment have been shown in figure 2.10(a) and (b). In figure 2.10(a) the absorption is fully polarized but does not match with the emission dipole while in figure 2.10(b) the absorption is not polarized compared to the emission. Figure 2.10(d) summarizes the misalignment between absorption and emission polarization for various emitters in hBN with different ZPL energies. This plot emphasizes the fact that the distribution of misalignment between the excitation and emission for different emitters is broader when they are excited with higher energies relative to the ZPL energy. Therefore, the mechanism can be described by considering an intermediate electronic state (figure 2.10(d)). When excitation energy is close to the ZPL (i.e $\Delta E < 200\ meV$) the polarization behavior follows Huang-Rhys model [69] where the polarization selection rules for

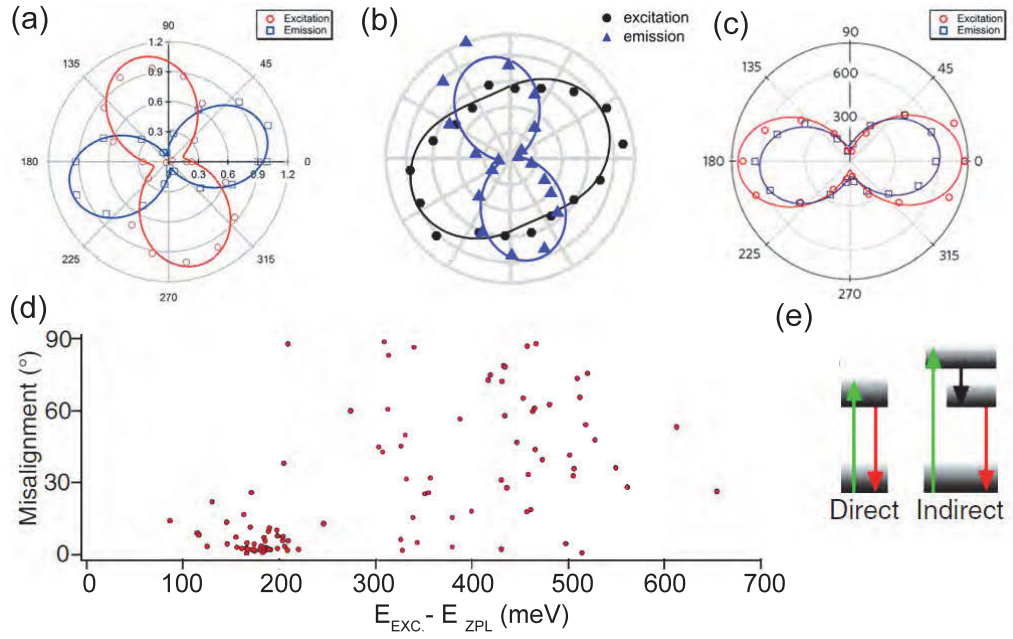

FIGURE 2.10: (a) Misaligned absorption and emission polarization, (b) Not fully polarized absorption and (c) Aligned absorption and emission of single photon sources in hBn. Reproduced from [65][66][30]. (d) Misalignment angle between absorption and emission polarization measured for 106 single photon sources in hBN as a function of difference between ZPL energy and excitation energy. The excitation energy was fixed at 532 nm. (e) Energy level diagram describing the absorption and emission mechanism in hBN single photon sources. Reproduced from [67].

absorption and emission are symmetric and identical polarization behavior is predicted for both absorption and emission (direct absorption). On the other hand when higher excitation energies are used (i.e $\Delta E > 200\ meV$) excitation may occur with the aid of intermediate states (indirect absorption). In this condition the same polarization angle for absorption and excitation is not anticipated [67].

2.4 Super-resolution far-field imaging

Based on Abbe's diffraction limit, the resolution of optical microscopes cannot exceed $\lambda/(2nsin\alpha)$ in the focal plane and $\lambda/(nsin^2\alpha)$ along the optical axis where λ,

α and n denote the wavelength, the semi-aperture angle of the lens and the refractive index, respectively. Development of electron and scanning probe microscopy techniques address the resolution issues of optical systems in many research areas. However, in biology and life science optical techniques take advantage of transparency of the cell enabling nondestructive imaging of the interior of the cells. As a result despite the low resolution, still more than 80% of studies in these field are being done by conventional optical microscopes. Several approaches such as confocal microscopy [70][71] and two-photon excitation fluorescent microscopy [72], have been proposed in order to improve resolution in optical microscopes. In practice, the resolution after applying these techniques still is not impressive and remains larger than $\lambda/2 \simeq 200nm$. Another fundamental problem in optical microscopy arise with the limitation of resolution in the optical axis (z) specifically in 3D imaging. Resolution in this direction is worse compare to the resolution in the imaging plane due to the fact that a lens cannot produce a complete spherical focal spot unless it is made spherical too. The numerical aperture of the lens reflects this issue which can be increased to 1.4 in oil immersion lenses. In mid 1990s, pioneer works by S. Hell [73] showed that diffraction limit can be broken by super resolution optical microscopy techniques such as Stimulated Emission Depletion (STED) [74] or Ground State Depletion (GSD) [75]. All of these techniques are based on the fact that Abbe's diffraction does not apply on spectrally separated features. Moreover, the coordinate of a single point source can be arbitrary approximated with high precision (down to 1 nm) in an optical system [76]. Therefore, to break diffraction limit in a densely packed and similar emitters within any distance $< \lambda/2n$, sequential recording of the area can reveal sub-diffraction features by excitation of one emitter (switch-On) while keeping the rest in the dark state (switch-Off). Various mechanisms utilizing deliberate switching on and off an emitter. Figure 2.11 summarizes super resolution techniques and their underlying mechanism to achieve on or off state of an emitter in chronological order. The immediate approach to switch off an emitter would be use of a laser which facilitate a transition into a dark state for the emitter (depletion laser). This family of super-resolution optical microscopy techniques are known as

Reversible saturable optically linear fluorescence transitions (RESOLFT) and their practical resolution is approximated by:

$$\Delta r \simeq \frac{\lambda}{2nsin\alpha\sqrt{1 + I_{\max}/I_s}} \tag{2.2}$$

I_s defines as the intensity which fluorescence reaches 50% of its maximum, is saturation intensity and I_{max} is the intensity of the depletion laser. Equation 2.2 implies that there is no barrier for the resolution as when $I_{\max}/I_S \to \infty$ then $\Delta r \to 0$.

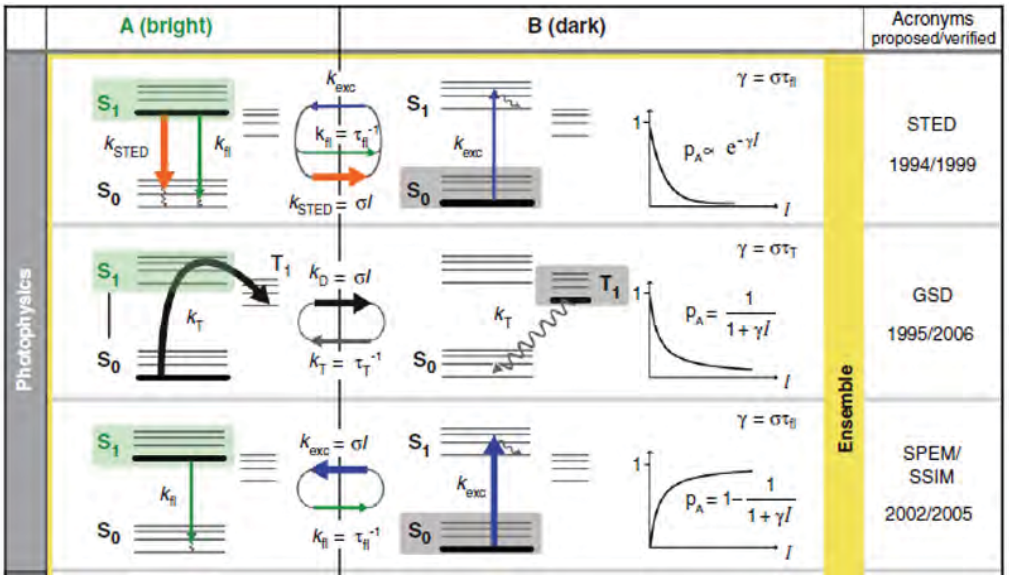

FIGURE 2.11: Three mechanisms for inhibition of the emission based on photophysics of an emitter is demonstrated. S_0: ground state, S_1: excited state, σ: adsorption coefficient, k: decay rate, τ: decay time. Reproduced from [7].

STED microscopy which is regarded as the first concept of RESOLFT type, uses of the basic idea of inhibition of *spontaneous* emission in the diffraction-limited area by de-excitation through *stimulated* emission [74][77] as shown schematically in figure 2.11. As predicted by Einstein, the light can induced transitions from ground state to the excited state ($S_0 \to E_0$) as well as from excited state to the ground state ($E_0 \to S_0$) with the same probability [78]. Similar in a situation in laser medium, the population of both levels can only be equilibrate which means only half of a fluorescence emission is suppressed through stimulation. Fortunately, the thermal

relaxation (k_{vib}) is occurring with much faster rate compare to the spontaneous fluorescent rate ($k_{vib} > k_{fl}$) which means the E_n immediately depopulates which prevent stimulating of the emission from this state. On the other hand, stimulating the emission from E_0 has to happen before the spontaneous decay rate (k_{fl}). This gives the important condition on the length of the STED pulse (τ_{STED})[74][79][80]:

$$k_{vib}^{-1} \ll \tau_{\mathrm{STED}} \ll k_{fl}^{-1} \tag{2.3}$$

In its initial proposal, 10-100 ps pulses was used as an STED beam considering the fact that spontaneous emission rate is in the order of ns. However, it was shown later that it is possible to use continuous wave (CW) lasers for STED microscopy if certain conditions are met [81].

High resolution imaging with STED has been performed on a number of systems including quantum dots [82], up-conversion nanoparticles [83] and color centers in diamond [84]. However, to date among solid state single photon sources, STED has only been demonstrated with NV centers in diamond. Although PALM and STORM imaging techniques use blinking or bleaching behavior of fluorescence organic emitters to their advantage, specifically in STED applications this become a major problem where high intensities of STED beam is desirable to achieve better resolution following equation 2.2. For this reason photostability of defect centers in diamonds offers better opportunity for exploring STED microscopy and its application in bio imaging [46]. In the first report of high resolution imaging of NV centers with STED, the resolution of 8 nm upon applying of 3.7 GW cm^{-2} STED beam intensities was achieved[84]. An example of STED microscopy on NV centers and its comparison with confocal image have been shown in figure 2.12 where individual centers have been resolved.

Stimulated emission is not the only mechanism to inhibit the fluorescence. Most of the emitters consist of additional metastable states which transition through them

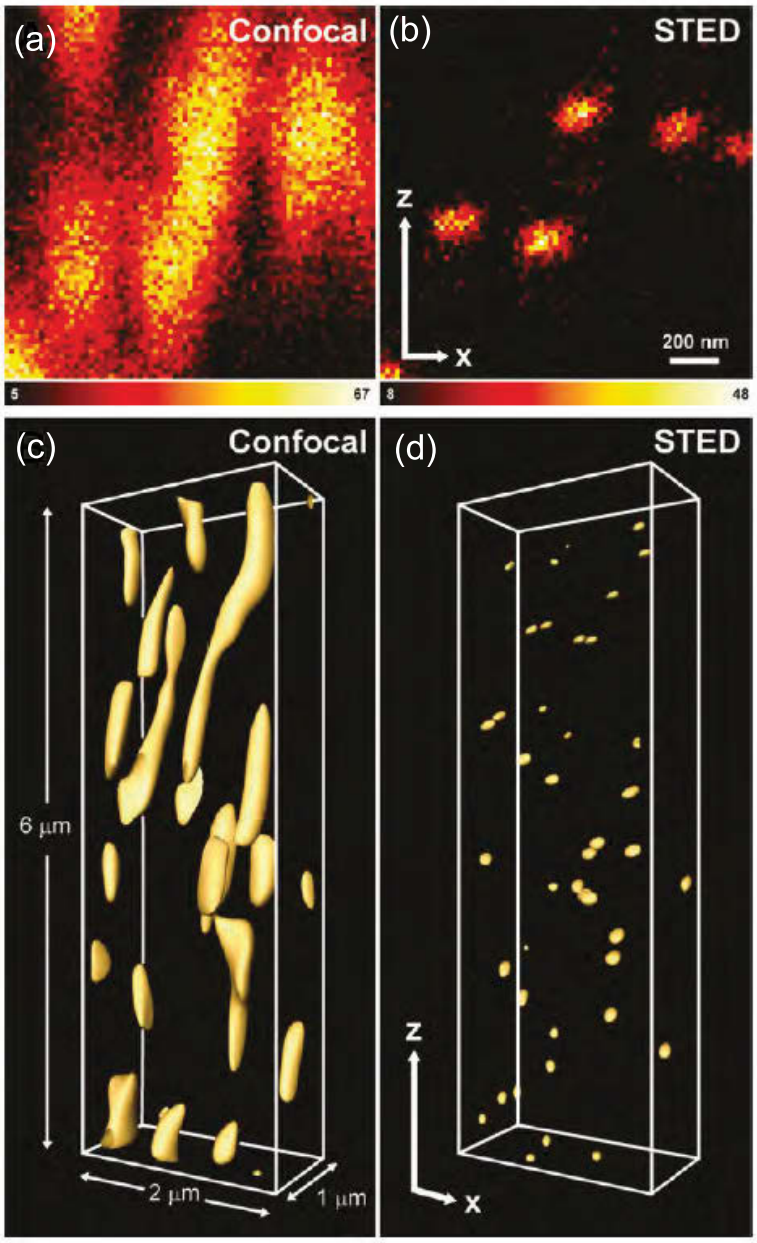

FIGURE 2.12: (a) 2D confocal scan of NV centers in diamond (b) STED image of the same area revealing individual NV centers.(c) 3D scan of bulk diamond contatining NV centers. (d) 3D STED imaging of the same area. Reproduced from [85].

is non-radiative. GSD takes the advantage of inter system crossing (ISC) to inhibit the fluorescence by transferring into metastable states which can be achieved at lower intensities compare to the intensities required for STED [86][75][73]. The concept for GSD has been sketched in figure 2.11. Assuming the very fast thermal

relaxations (k_{vib}) for all states, the population probability equations under excitation with photon flux of h_{exc} for vibrationally relaxed states (S_0 , E_0 and T_0) can be written as[75]:

$$\begin{aligned}
\frac{dn_S}{dt} &= -h_{ext}\sigma n_S + k_{fl}n_E + k_{ph}n_T \\
\frac{dn_E}{dt} &= h_{ext}\sigma n_S + k_{fl}n_E - k_{isc}n_E \\
\frac{dn_T}{dt} &= k_{isc}n_E - k_{ph}n_T
\end{aligned} \tag{2.4}$$

The rates between different states (k_{fl}, k_{ISC} and k_{ph}) are reciprocal values of the lifetime of that particular state. When exciting with continuous wave laser, it is reasonable to assume that the system reaches an steady state where the population probabilities will not change anymore ($\frac{dn}{dt} = 0$). Considering $\Sigma n_i = 1$ the population of each state can be calculated as follows:

$$\begin{aligned}
n_S &= \frac{k_{ph}.(k_{fl} + k_{ISC})}{D} \\
n_E &= \frac{h_{exc}\sigma.k_{ph}}{D} \\
n_T &= \frac{h_{exc}\sigma.k_{isc}}{D}
\end{aligned} \tag{2.5}$$

with $D = (h_{exc}\sigma + k_{fl}).(k_{ph} + k_{isc}) + k_{isc}(k_p h - k_{fl})$. The rate equations for a single photon source can be solved based on power dependence measurement of autocorrelation functions [87]. In hBN the decay rates of 440.7, 17.73 and 45 MHz have been reported for k_{fl}, k_{isc} and k_{ph} respectively, based on autocorrelation power dependent measurement with excitation with 532 nm laser [30]. The same method yielded values of 41.7, 2 and 1 MHz for NV centers in diamond [88]. Figure 2.13 shows the population probabilities of each state as a function of excitation intensities for 2.13(a) single photon sources in hBN and 2.13(b) NV centers in diamond.

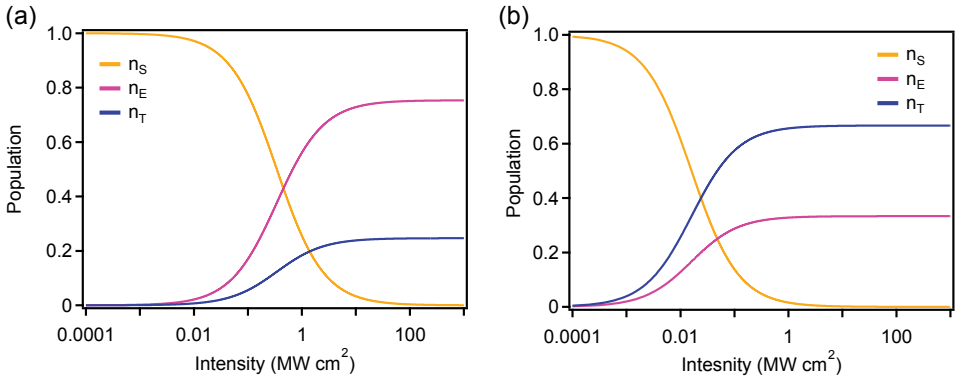

FIGURE 2.13: (a) hBn (b) NV

Plots in figure 2.13 indicates that under excitation higher than 100 MWcm^{-2} about 80% of the time the hBN emitter is in excited state and 20% in the metastable state and ground state is depleted. Similarly for NV center in diamond, under excitation of 1 MWcm^{-2} while the ground state is depleted, around 70% NV center is in metastable state and 30% in the excited state. An intuitive interpretation is that when the emitter is excited with high powers, at each cycle of excitation, a fraction of $k_{isc}/k_{isc} + k_{fl}$ is caught in the long-lived metastable state, ultimately resulting in depleting the ground state. The ground state remains depleted for the average period of τ_{ph} as long as excitation beam in on.

In GSD, excitation at intensities much higher than saturation intensities (I_s) produce an steep in the saturation curve which modifies point spread function (PSF) of the system. If an emitter is illuminated with a beam featuring zero intensities at the center such as doughnut-shaped beam (I_r) the point spread function (PSF) of the system (h_{psf}) can be expressed by:

$$h_{psf}^{GSD}(r, I_m) = h_{det}(r).\eta(I(r)) \tag{2.6}$$

with I_m the intensity at the crest of the doughnut, h_{det} the detection PSF and $\eta(I)$ saturation behavior of the emitter. Under excitations higher than saturation, h_{det}

can be ignored and FWHM of the h_{PSF}^{GSD} (resolution in GSD) can be approximated as [89][90]:

$$\Delta \approx \lambda(\beta\pi n)^{-}1\sqrt{\epsilon + I_s/I_m} \tag{2.7}$$

In this equation β quantify the steepness of the minimum, n is the refractive index and ϵ is the ratio of the minimum to maximum in the doughnut-shaped beam .One of the main concerns with GSD is the higher chance of photobleaching due to excitation to even higher states. Again based on photostability of the color centers in diamond, NV centers have been subjected to high resolution imaging with GSD technique [90]. Figure 2.14 shows the fluorescence emission from a NV center in diamond under excitation intensities beyond saturation.

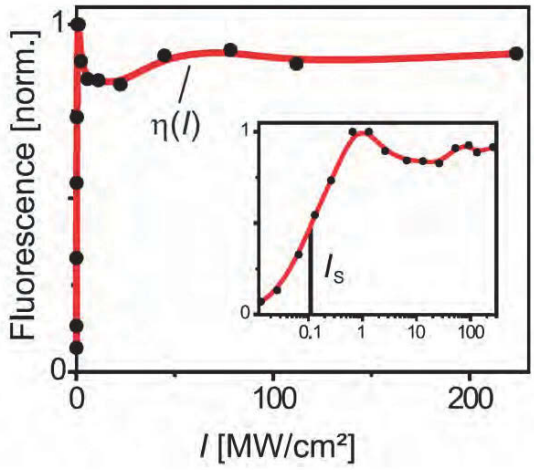

FIGURE 2.14: Stable emission beyond saturation power, enables GSD super resolution microscopy. Reproduced from [90].

The saturation intensity for transitions from ground state into excited state ($^3A \rightarrow {}^3E$) can also be estimated based on optical cross-section ($\sigma = 10^{-16} cm^2$) and lifetime ($\tau_{fl} = 12\ ns$) by the following equation:

$$I_s = \frac{hc}{\lambda\sigma\tau_{fl}} \tag{2.8}$$

with h denoting the Planck's constant and c vacuum speed of light. The saturation intensities for NV is obtained to be around 110 kW/cm^2. The scan of the NV center with a doughnut-shaped beam will also feature a minimum in the center where the NV is in the dark condition. This minimum corresponds to the location of the NV center with sub-diffraction resolution, hence named as "Negative GSD". The recorded GSD images of a NV center under increasing excitation intensities are demonstrated in figure 2.15(a). The resolution of the GSD with NV also is well described by equation 2.7.

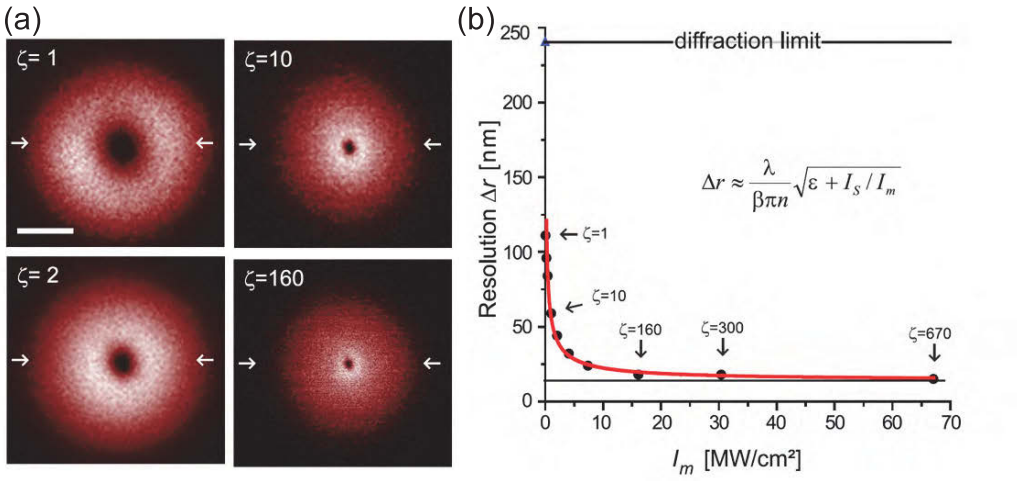

FIGURE 2.15: (a) Imaging of the NV center at excitation beyond saturation power: The factor ξ is the ratio of saturation to excitation intensity for each image. (b) Resolution of the GSD image as a function of excitation power following the proposed equation for GSD. Scale bar is 150nm. Reproduced from [90].

Although GSD produced the negative imprint of the emitter, it is possible to get the direct image through a simple image processing (deconvolution) or by aligning a second Gaussian laser in the middle of the doughnut-shaped one. Deconvolution of the negative GSD is being done by removing the high resolution details of the negative image and then subtracting it from the negative GSD image [91]. In general the image processing step is easier to implement, however, getting direct images from GSD requires control over transitions to and from metastable state. This is possible for example for NV centers in diamond as shown in figure 2.16 [92].

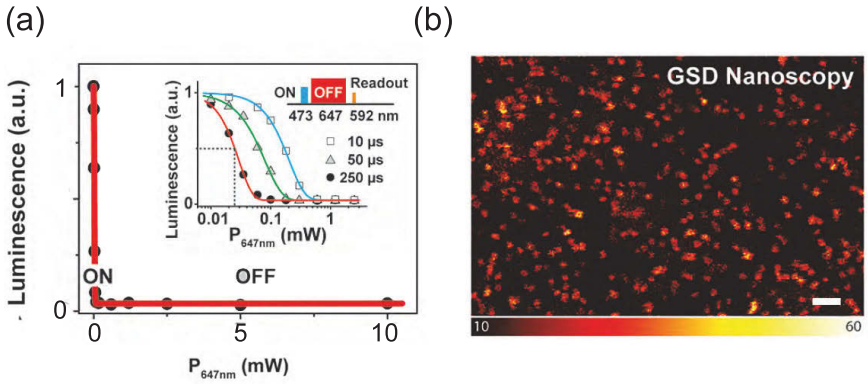

FIGURE 2.16: (a) Inhibition of emission from the NV center through repopulating the metastable state using pulses of 641 nm laser. The effect of pulse duration on inhibiting of emission is shown in the inset. (b) Direct GSD images of dense NV centers in bulk diamond. Scale bar is 100 nm. Reproduced from [92].

Chapter 3

Experimental methods

3.1 Optical measurements

The basic concept of confocal microscopy was originally developed by Marvin Minsky in the mid-1950s at Harvard university. The aim in confocal microscopy is to collect the light from one point and reject the *background* light from any other points in the imaging plane to improve the contrast of the system. Confocal microscopy uses the very same component of normal optical microscope with addition of pinhole to reject background light. Here a brief overview of the basic operation principle and properties of optical microscopes is given following by the confocal microscopy concepts and method for measurement of a single photon sources. Finally the modification in confocal microscopy which enables supreresolution measurement is explained.

3.1.1 Optical microscopy

Normal optical miscorscope is consist of three main components: the illumination source, the objective lens and the eyepieces. A different variant of optical microscope uses a detector to collect the light which is mostly used in investigation of low

intensity fluorescent materials such as single photon sources. In any case, the most important component is the objective or the lens which both focus and collect the light on the target area of the sample. The main property of the objective which determines its collection efficiency in collecting the photons is the numerical aperture (NA). The NA is given by :

$$\mathrm{NA} = n \sin \alpha \tag{3.1}$$

with n being the refractive index of the medium and α the maximum angle with optical axis that light from the focal point can still be collected. The increase in the NA result in more collection efficiency. With refractive index of air being 1 and according to equation 3.1 the maximum theoretical NA for a lens is 1 however the commercially available lenses uses mediums with higher refractive index to achieve the NA of 1.4 for oil immersion lenses. On the other hand, the resolution is another important factor in any microscopy technique. In the fluorescent microscopy, resolution is depend on the illumination wavelength (λ) and NA of the lens with the following equation:

$$resolution = 0.61 \frac{\lambda}{NA} \tag{3.2}$$

Equation 3.2 is calculated based on geometry in an optical system. A point like source can be well approximated with Airy disk. As shown in figure 3.1 radius of the Airy disk is considered for calculating the resolution leading to equation 3.2 [93].

3.1.2 Confocal microscopy

The resolution can be improved slightly in confocal microscopy, however the success of this type of microscopy is specifically due its the higher contrast. Contrast is the noisy reality of the real measurements that limits the ability to use the available

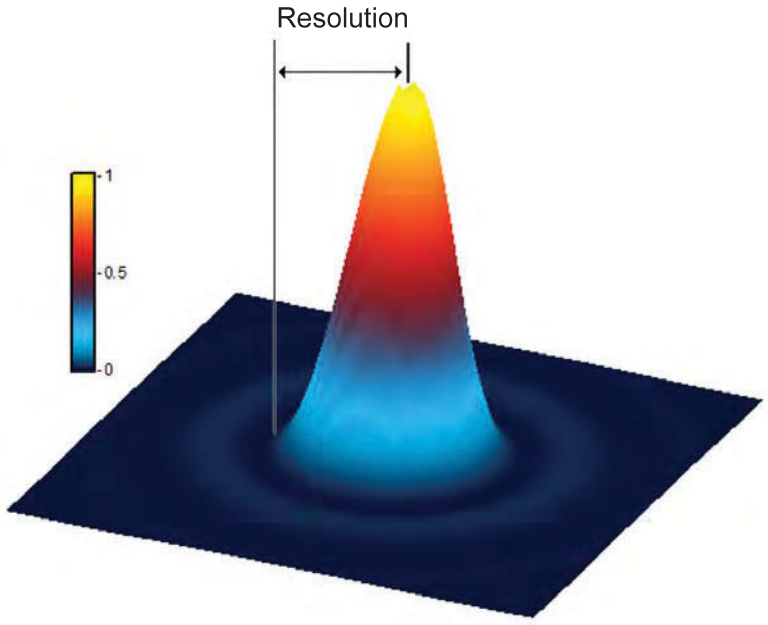

FIGURE 3.1: Airy disk function describing the emission from a point source.

resolution. The principle of a confocal microscope has been sketched in figure 3.2. The illumination source which is, commonly a laser, is focused by an objective lens and the focal point is imaged into the detection by another lens. Inserting a pinhole in front of detection will block any collected light from outside of the focus point and only let the light from the excited region to reach the detector. In this scheme, the illumination and detection will be from the same focus spot. The optimal diameter of the pinhole ($d_{pinhole}$) is calculated based on maximum background light rejection and maximum light transmission from the focal point at the same time. This will be obtained from Airy disk intensity distribution of a point source (figure 3.1). Considering the magnification of the objective lens (m) it can be calculated as follows:

$$d_{pinhole} = \frac{1.22.\lambda.m}{NA} \tag{3.3}$$

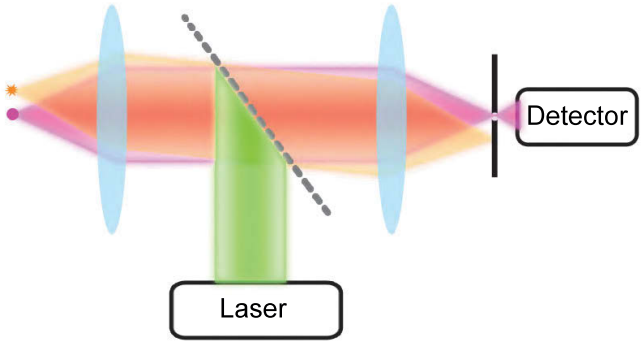

FIGURE 3.2: Inserting a pinhole in front of detector will reject the emission from outside of the focus spot.

This configuration will provide information from a single focus spot on the sample at each illumination event. In order to acquire an image from an area of the sample, it needs to be scanned. As a result confocal microscopy is used as fluorescence confocal microscopy where illumination source is a laser which excites the emitter and only the fluorescence is collected. In this thesis, scanning fluorescent microscopy was used to investigate solid state emitters in diamond and hBN. In order to scan the sample, scanning mirror was used otherwise is stated. For this purpose a doublet lens is equally placed between the objective lens and Piezo controlled mirror. Scanning the sample can be done by deflecting the beam using the mirror.

3.1.3 Measurement of single photons

When a single molecule (or an emitter) has absorbed a photon it cannot absorb and emit a second photon until it has returned to the electronic ground state. Thus the photons exhibit an antibunching phenomena with a time constant defined by the fluorescence lifetime and excitation power. Current advances in technology, has provided avalanche photodiode (APD) detectors with high signal to noise ratio with capability of detecting very low intensity of light such as a single photon. However, these detectors cannot operate as the same speed of emitters decay rate. This means that while an emitter is producing stream of photons, the detector after each

detection event requires a recovery time during which no detection is happening (dead time). As a result correlation cannot be done with a single detector [94]. The solution to this, is the use of Hanbury Brown and Twiss (HBT) interferometer and photon statistics. Figure 3.3 shows the schematic of HBT setup for single photon measurement. The collected photons are splitted with a 50:50 beam splitter and conducted into two arms of detection. Using a time-tagger instrument, each photon is time tagged and recorded.

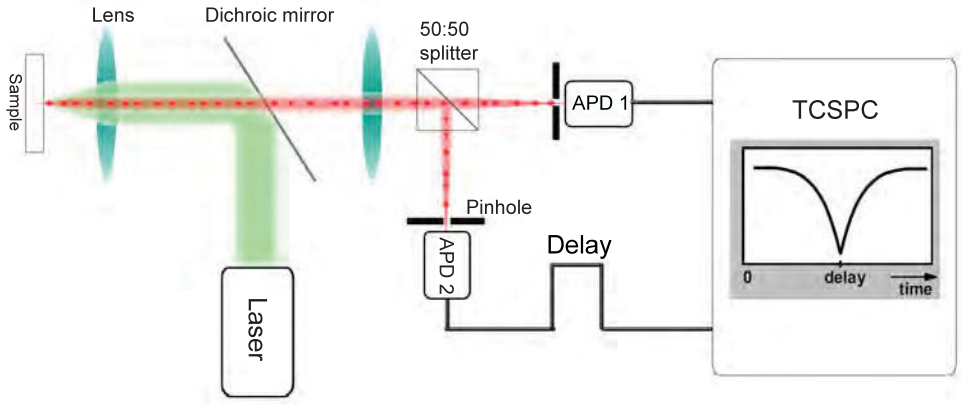

FIGURE 3.3: The quantum nature of the light is revealed through time-correlated single photon counting (TCSPC).

The photon statistics is described by autocorrelation function ($g^2(\tau)$) of the emitted light which is the second order autocorrelation function of intensity of light and it is defined as:

$$g^2(\tau) := \frac{<: I(t)I(t+\tau) :>}{< I(t) >^2} \tag{3.4}$$

with $I(t)$ the intensity operator, τ the time difference, :: normal ordering of the operators and $< ... >$ indicating time average [95]. In the case of a fluorescence source, autocorrelation function indicates the probability of detecting a photon after a certain time $t + \tau$ if a photon has been emitted at a time t. Evaluation of equation 3.4 for a time difference of $\tau = 0$ results in:

$$g^2(0) = \begin{cases} 2, & \text{for thermal light} \\ 1, & \text{for coherent light} \\ 1 - \dfrac{1}{n}, & \text{for a n-photon number state} \end{cases} \tag{3.5}$$

Therefore, it can be used to determine the source type. For a thermal source the possibility of emitting photon is higher when the intensity is higher, as a result autocorrelation at zero delay time is larger than 1 ($g^2(\tau = 0) > 1$). A perfect coherent wave has constant amplitude and phase, therefore, the autocorrelation function for this wave will be perfectly flat and the number of photon pairs will be independent of τ ($I(t) = I(t + \tau)$). For a single photon emitter, as only one photon is arriving at the beam splitter (n=1), the autocorrelation at zero delay time is zero ($g^2(\tau = 0) = 0$) [94]. This phenomena is known as antibunching and photon sources which shown antibunching phenomena are called quantum emitters. In addition, in solid state emitters apart from the radiative transition from excited state into ground state, there is a non-radiative transition through metastable state(s). The presence of this long-lived level produce bunching in longer time scale in the autocorrelation function [17][96]. An example of bunching in autocorrelation measurements from single NV center in diamond is shown in figure 3.4(a).

On long time scales the spontaneous decaying from excited states is occurred and only the effect of slower transitions between levels are left. If the inter system crossing rates are smaller than the spontaneous rate from excited state, the solution for autocorrelation can be approximated by solving the population dynamic equations for a 3-level system [97] (based on the notations shown in figure (3.4(b))):

$$\frac{d}{dt}\begin{pmatrix} n_1 \\ n_2 \\ n_3 \end{pmatrix} = \begin{pmatrix} -k_{12} & k_{21} & 0 \\ k_{12} & -k_{21} - k_{23} & k_{32} \\ 0 & k_{23} & -k_{32} \end{pmatrix} \cdot \begin{pmatrix} n_1 \\ n_2 \\ n_3 \end{pmatrix} \tag{3.6}$$

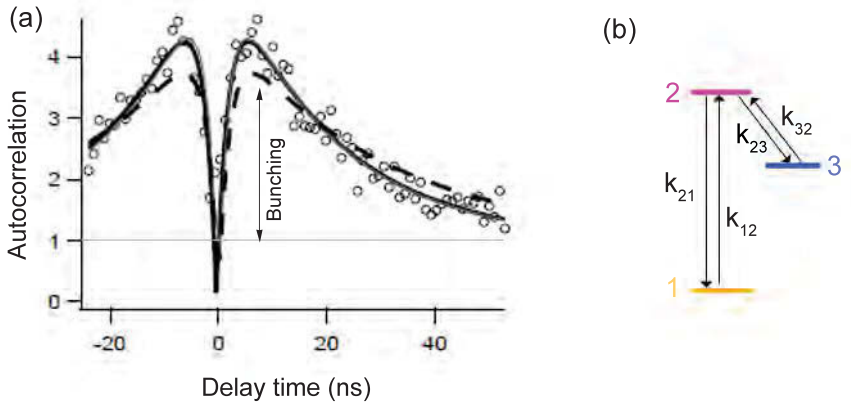

FIGURE 3.4: (a) Bunching and antibunching effect in autocorrelation measurement of a single NV center. The antibunching is due to the presence of long-lived metastable sate (state 3) shown in (b).

For such a system the instantaneous emission probability of a photon is then proportional to $n_2(t)$, and an analytical expression for second order correlation can be obtained by normalizing $n_2(t)$ to $n_2(t \to \infty)$. Assuming the nonradiative transitions from metatable state to ground state (k_{31}) can be neglected the autocorrelation for a 3-level system can be expressed by:

$$g^2(\tau) = 1 + c_2.exp(-\frac{\tau}{\tau_2}) + c_3.exp(-\frac{\tau}{\tau_3}) \tag{3.7}$$

where the decay times and coefficients are given by:

$$\begin{aligned} \tau_{2,3} &= 2/(A \pm \sqrt{A^2 - 4B}) \\ c_2 &= \big(1 - \tau_2 k_{32}\big)/\big(k_{32}(\tau_2 - \tau_3)\big) \\ c_3 &= -1 - c_2 \end{aligned} \tag{3.8}$$

with

$$A = k_{12} + k_{21} + k_{32} + k_{23}$$
$$B = k_{12}k_{23} + k_{12}k_{32} + k_{21}k_{32} \tag{3.9}$$

Similarly, this model can be extended to 4 or more level systems where more than one long-lived metastable state exist. In this case, additional exponential decays will be inserted in the analytical expression of second order autocorrelation, corresponding to the number of long-lived metastable states in the system [17][94][96][97]. In Chapter 6, the four-level model we used for fitting autocorrelation data. Three decay rates are considered for the excited state ($1/\tau_{exc}$)and two metastable dark states ($1/\tau_1$ and $1/\tau_2$). The equation used for fitting the data is as follows:

$$g^2(\tau) = 1 - (1 + a_1 + a_2)exp(\frac{\tau}{\tau_{exc}}) + (a_1)exp(\frac{\tau}{\tau_1}) + (a_2)exp(\frac{\tau}{\tau_2}) \tag{3.10}$$

3.1.4 ODMR

Measurement of ODMR for NV centers has been done with the same confocal microscopy configuration. The only required modifications is the consideration for conveying the microwaves to the NV center. More sophisticated implement of ODMR measurements is being done with a pulse sequence of laser and microwave such as Ramsey sequences adopted from spin echo measurement in nuclear magnetic resonant (NMR) field [98][99]. The main benefits of using pulse sequences is to achieve higher sensitivity specifically for alternating magnetic fields [47]. As in this work, only static magnetic field is demonstrated and moreover high sensitivity measurement was not the objective of the work here on NVs, ODMR measurement using CW excitation is only explained.

• ODMR measurement using CW laser.

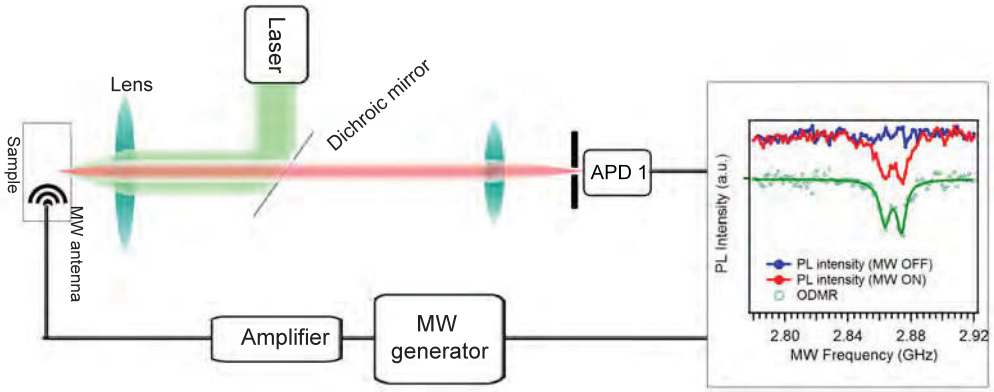

FIGURE 3.5: The microwave generator produces pulses of microwaves which is synchronized with the detector. Fluorescence is recorded when the microwave is on or off and the ODMR signal is calculated by subtracting the two recorded fluorescent.

This is the simplest method of measuring ODMR effect of NV centers in diamond. ODMR measurements were conducted on the patterned nanodiamonds using a microwave (MW) generator coupled to a 20 W amplifier. The microwave field is transferred from a 30 μm copper wire placed very closed to the targeted NV center. Then a 50 μW continuous green laser (523 nm) focused using a 0.9 NA objective lens, has been used to excite NV centers in nanodiamond. Photoluminescence was collected with and without microwave excitation at frequencies ranges from 2.78 to 2.95 GHz to avoid any possible measurement artifacts such as thermal drifting. The different of the PL intensities between these two conditions will produce the ODMR signal. The data is fitted using Lorentzian curves. Figure 3.5 shows the schematic of the measurements. An example of raw data where PL signal is recorded when microwave was on (red curve) or off (blue curve) is also demonstrated in the plot in figure 3.5. The ODMR signal (green curve) was calculated by subtracting the PL signal when microwave was on from the one when microwave was off.

3.1.5 Super resolution far field imaging

In order to implement the concept of super resolution imaging, a confocal setup is used. The excitation beam profile is then modified to satisfy the conditions required for super resolution microscopy. In conventional confocal microscopy the ideal excitation beam has a Gaussian profile. However, for super resolution microscopy the depletion beam features intensity difference, usually a local zero within the focal spot. In the first introduction of high resolution concept, this was achieved using combination of lenses to mismatch the depletion laser focus spot from the excitation one [75]. Although not perfect, it was enough to prove the concept. However, it is possible to produce a beam with a local zero within the diffraction spot. The so-called doughnut-shaped beam is an optical vortex which is commonly produced almost perfectly using spiral phase plate [100], spatial light modulators or holograms [101]. Optical vortices are a peculiar type of beam that has torus-like (doughnut-like) intensity profile and an azimuthal phase dependence ($exp(il\theta)$) with respect to the beam axis which is a helicoidally shaped wavefront. This kind of beam profile also can be produced directly by lasers as an intrinsic transverse mode or by diffraction from fork-shaped intensity masks [102].

In this work, spiral phase plate was used to convert the Gaussian profile into doughnut-shaped one. The phase plate structure is composed of entirely of spiral or helical phase steps, whose purpose is to control the phase of the transmitted beam and produce the first order of the Bessel beam. This beam will have a phase distribution such that the phase changes continuously from 0 to 2π around the optical axis in the pupil plane. Since the distribution has a phase difference of π at a symmetric position with respect to the axis, the electric field completely cancel on the axis and doughnut-shaped intensity profile on the focal plane is produced [103].

To produce the doughnut-shaped beam, first the laser was coupled into the single mode fiber to produce a fully Gaussian beam. The polarization of the beam was also purified into linear polarization using a polarizer beam splitter (Thorlabs -Polarizing

beam splitter cubes). Then, the laser beam was transmitted across the phase plate. Doughnut-shaped beam was made by adding a phase retarder plate ($\lambda/4$) to produce a fully circularly polarized light. Most importantly, consideration needs to be made to avoid changes in the polarization of the light after passing through the other optic components such as mirrors and dirchoric. In this regard, the vertical polarized light was changed into circular just before the objective lens. Schematic of the setup is shown in figure 3.6.

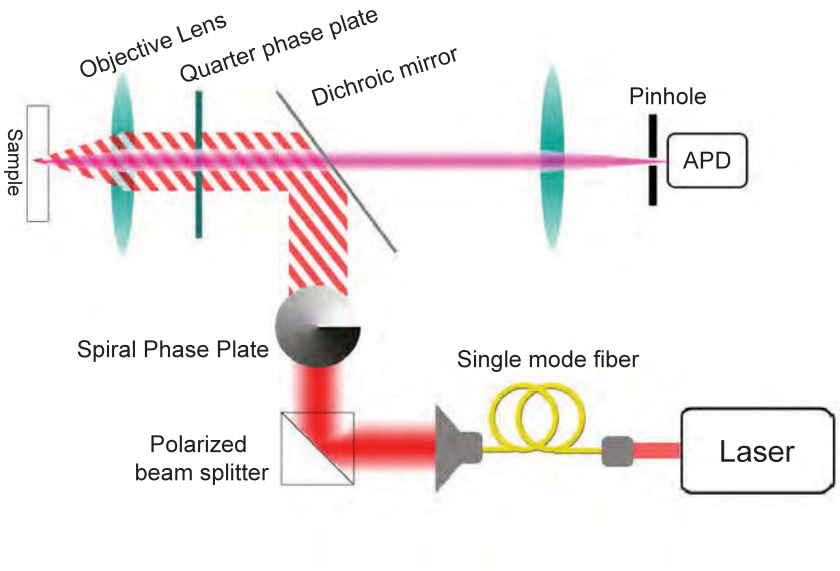

FIGURE 3.6: schematic of high resolution setup

For super resolution imaging in this work, Sample was mounted onto a XYZ piezo stage (Physik Instrumente-Nanocube P-611) with positioning resolution of 0.2 nm. Excitation was performed using different laser sources: Ti:saph (M-squared, 700-750 nm), Supercontinuum (NKT photonics, Fianium WhiteLase supercontinuum laser) equipped with Acousto-optic Tunable Filter (AOTF, 400-550 nm), 532 nm laser (Shanghi dreamlasers, 532nm low noise CW laser), 675 nm laser (PiL051XTM, Advanced Laser Diode Systems GmbH). Doughnut-shaped beam, was produced by directing the beam through a vortex phase plate (RPCphotonics, VPP-1b for 708 nm or VPP-1c for 532 nm lasers) and combination of polarizer beam splitter and quarter-wave plate as explained earlier. The 708 nm and 532 nm lasers were guided to the sample using a long-pass filter (Semrock 785nm EdgeBasic) and a Dirchoic mirror

(Semtock 532 nm dirchoic), respectively, and were focused on the sample through an aberration-corrected objective lens (Nikon 100X, NA = 0.9). The emission collected from the same objective was filtered using a notch filter (Semrock, 785 nm StopLin notch filter) and a 780 nm long-pass filter (Thorlabs, long pass color filter) and then coupled to the fiber which was connected to a spectrometer (Acton Spectra ProTM, Princeton Instrument Inc.) equipped with a 300 $lines/mm$ grating and a charge-coupled device (CCD) detector with a resolution of 0.14 nm, or splitted into 50:50 in a Hanbury Brown and Twiss (HBT) interferometer for autocorrelation measurement using two avalanche photon detectors (Excelitas Technologies TM) and a time correlated counting module (Picoharp300TM, PicoQuantTM).

3.2 Self-assembly of nanodiamonds

In this section the principles of techniques used for direct assembly of nanodiamond in a desired pattern is described. These techniques include deposition of carbon with Electron beam induced deposition, amine functionalization with ammonia plasma treatment and finally self assembly of nanodiamond through chemical bonding.

3.2.1 Electron beam induced deposition

Direct write technologies with focused electron beams, focused ion beams or photon offer unique advantages over classical resist-based processes [104][105][106]. Among them Focused electron beam induced process is capable of in situ deposition, fabricating three dimensional structures and etching nanostructures with nanometre scale size resolutions [107][108]. It was first reported by Steward in 1934 [109] as a source of contamination in electron bombardment system and became a fabricating technique for growing different materials later. The process involves the electron induced dissociation of gaseous precursor molecules adsorbed to the surface into volatile and non-volatile fragments which is known as electron beam induced etching

(EBIE) and deposition (EBID), respectively. The process is analogous to localized chemical vapour deposition (CVD) except that high energy electron beam involved dissociation of the precursor material. Organometallic CVD precursors with different carbon-containing ligands are commonly used. The resulting deposit is not pure and contain carbon in the structure which is mainly introduced from carbon present in the precursor composition. One of the major advantages of beam induced processing is that the pattern can be define on flat as well as topographical surfaces. Low growth rates compare to lithography techniques and carbon contamination are typical disadvantages of the EBID. Removing the carbon impurities has been the main challenges in electron beam induced researches [104][110][105].

Electron beam induced processes are illustrated in figure 3.7. In general, Scanning electron microscopes equipped with a gas delivery system (GIS) can be used for this purpose. Differential vacuum pressures in the column and chamber is possible through using an aperture and a pumping scheme as shown in figure 3.7(a). The electron beam is passed through the column in high vacuum and reached the sample in the presence of gaseous molecules. Gas molecules adsorbed on a surface is dissociated under the influence of electron beam. In case of deposition (figure 3.7(a)), the non-volatile fragment of the precursor adhere to the substrate and form a deposit. The reaction occurs only locally at or around the irradiated area. The energy for precursor dissociation is supplied by primary (PE), secondary (SE) and backscattered (BSE) electrons. However SEs with energies less than 50 eV are considered to play the main role on dissociation of precursor molecules [111] as the probability that an electron breaks a bond, depends on the electron energy and is expressed by the cross section. The larger the cross section, the larger the probability that a bond in the molecule will be broken. Since the contribution of each electron species cannot be determined, there is no consensus yet on this subject. On the other hand, various interactions between substrate, precursor and electron beam is happening during the process which result in many factors involved in the deposition process

[104][112]. Apart from deposition or etching, electron beam irradiation in the presence of a gaseous environment has been used for surface processing. An example of such process is changing the surface termination of diamond with fluorine which induced charge switching and photochromism of NV centers [113].

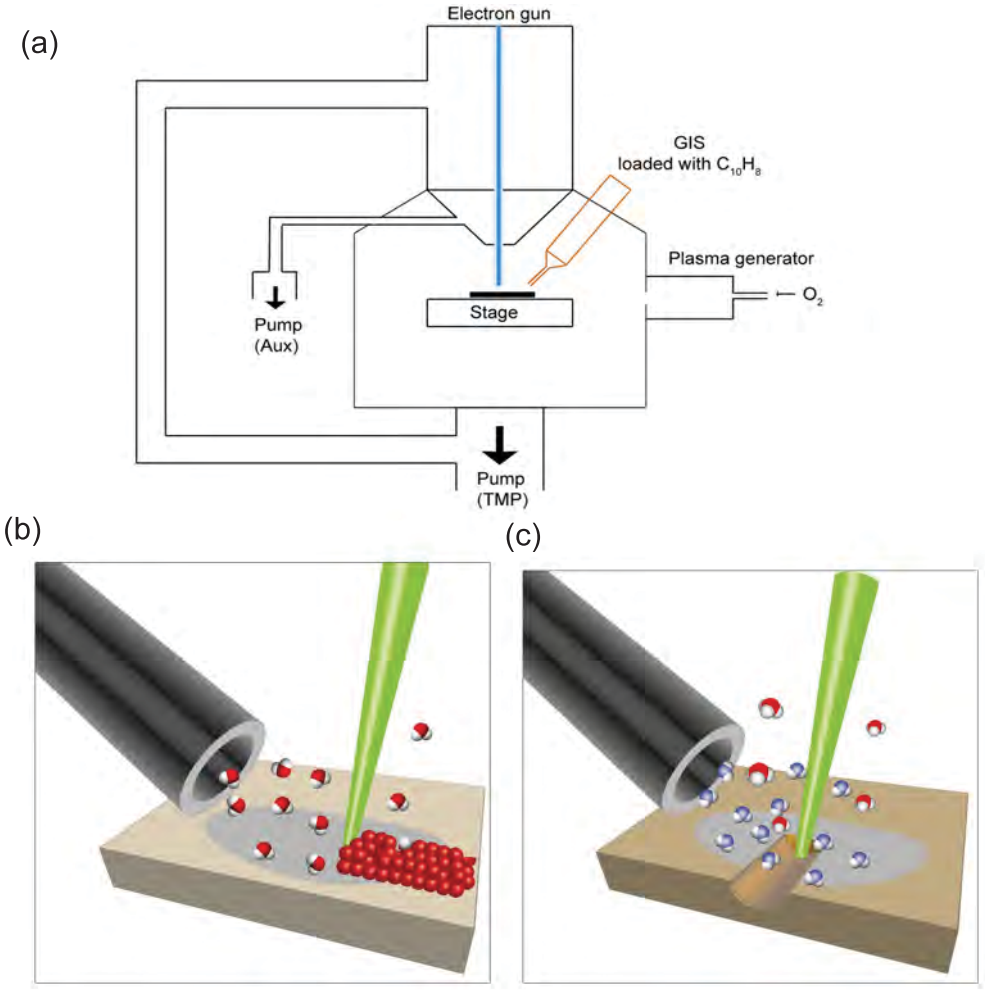

FIGURE 3.7: (a) Schematic of an environmental electron microscope with differential pumping which enables keeping the column at high vacuum while gas molecules from precursor are delivered by GIS into the chamber at lower vacuum conditions. (b) Dissociation of gas molecules by energy of the electron beam result in deposition (EBID). (c) Dissociation of the gas molecules by the energy of electron beam can produce reactive species which etch the substrate (EBIE).

Apart from major issues in electron beam deposition of metals, carbon deposition is possible using organic precursors such as Naphthalene, Ethanol or Benzene. The

resulting carbon is mainly amorphous and has found application in clamping of nanostructures or as template for mask repair or AFM tip fabrication [114][115].

Here, Naphthalene was used as precursor for carbon deposition with EBID. Prior to deposition, substrates were cleaned by sonication in Acetone and Isopropyl alcohol (IPA) for 10 minutes following by immersing in Piranha solution (3:1, H_2SO_4:H_2O_2). The substrates were then transfered into the vacuum chamber of a FEI Sirion XL30-FEG environmental scanning electron microscope (ESEM) and exposed to an oxygen plasma (50 W, 1 $Torr$) for 2 hours to remove any residual contamination. For deposition of carbon, Naphthalene precursor ($C_{10}H_8$, Sigma Aldrich, 99%) inside the Gas injection system (GIS) was heated to 30 $°C$. The gaseous precursor was delivered into the ESEM chamber through a needle with diameter of 500 μm positioned 200 μm above the surface.

3.2.2 Ammonia Plasma processing

Ammonia plasma has been implemented in various applications as a means of modifying surfaces of polymers to improve their adhesion [116], creating ultrathin nitride passivation layers on semiconducting devices such as polycrystalline silicon [117] and GaAs [118] and extensively to deposit amorphous hydrogenated silicon nitride (with mixture of silane) [119]. In many ammonia-based plasma systems, Amine radicals (NH_2^-) is considered an important intermediate. In general, modification is caused by implantation of nitrogen containing functionalities. Both NH^{2-} and NH_2^- radicals have been observed in these systems using optical emission spectroscopy (OES) and it is proposed that the interaction of NH_x species with the polymer surface can lead to implantation of the desired nitrogen containing moieties [120]. In OES measurement, the NH_2 is identified through its high intensity fluorescence band in the region around 600 nm. By applying appropriate laser light with respect to the fluorescent band of NH_2 and collecting fluorescence spectra, it is possible to determine the identity of the fluorescing species and avoid unwanted signals in the spectrum.

Fisher et al. [121] reported on the NH_2 laser induced fluorescence intensity as function of radio frequency (RF) plasma power. In their studies plasma was created from 100 NH_3 with 13.56 MHz RF power, ammonia flow rate of 20 sccm and pressure of 65 mTorr at plasma source. The data is presented in figure 3.8. Formation of NH_2 in a pure ammonia plasma increases with RF power and reaches to its maximum at around 100 W, after which the concentration is decreased with further increase of RF power. This decrease is being related to fragmentation of NH_2 radicals at higher plasma power [122].

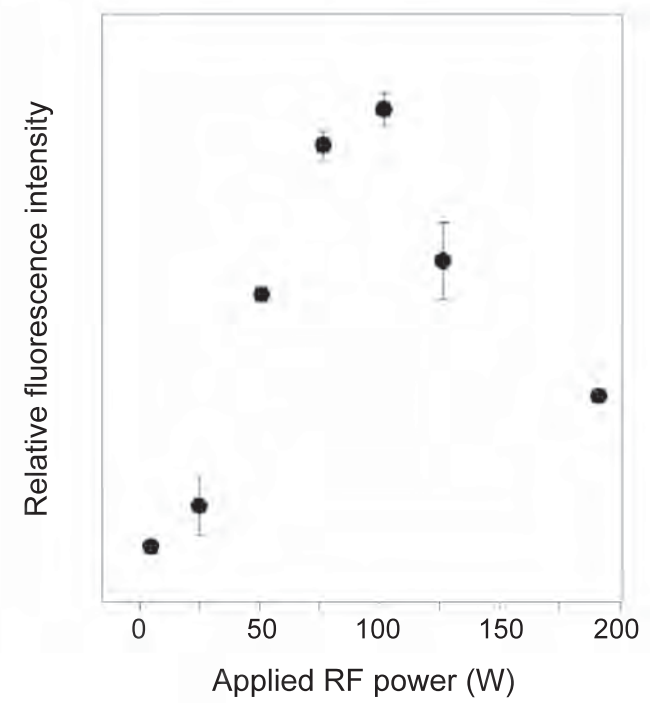

FIGURE 3.8: Reproduced from [122].

Ammonia plasma process here was done with Vacutec reactive ion etching (RIE) system. A Turbo molecular pump (TMP) provided a vacuum of around 1×10^{-6} mTorr in the chamber. Sample was loaded in the chamber directly after EBID process. Before running plasma, chamber and gas delivery lines were pumped to the base pressure. Then, Ammonia was delivered into the chamber using a mass flow controller (MFC) with 20 sccm flow rate which resulted in the increase of pressure to 5×10^{-2} mTorr in the chamber. During the gas delivery, the TMP was set to

stanby mode which run the pump with 60% of its efficiency to avoid damaging the pump but still keep the system on continuous pumping. Ammonia was run for 15 minutes to reach a steady vacuum pressure in the chamber. RF plasma was run at a power of 100 W for 45 seconds to create amine functional groups on the carbon surface.

3.2.3 EDC crosslinking

Creating conjunction between molecules using cross-linking agents is a well known method in chemistry and biology. The smallest available reagent systems for bio-conjugation are the so-called zero-length cross-linkers. These compounds mediate the conjugation of two molecules by forming a bond contacting no additional atoms. Thus, one atom of a molecule is covalently attached to an atom of a second molecule with no intervening linker or spacer [123]. 1-ethyl-3-(3-dimethylaminopropyl)carbodiimide (EDC) is a well-established zero-cross linker which has been used to covalently attach proteins onto different material such as carbon nanotubes (CNTs). The conjugation reaction occurs in two steps (figure 3.9). EDC first reacts with carboxyl group, forming an amine-ractive O-acrylisourea intermediate which finally reacts with an amine group to produce stable amide bond. However, the O-acylisourea intermediate is not stable and is susceptible to hydrolysis which results in poor conjunction efficiency. Higher efficiency is obtained by adding N-hydroxysuccinimide (NHS) or its more water soluble analogue Sulfo-NHS. Addition of these materials to the solution stabilized the intermediate by converting it to a semistable amine-reactive NHS ester. 10-20 fold increasing in conjuction efficiency has been reported by adding NHS [124][125]. EDC has been widely used for conjunction of proteins to carbon nanotubes (CNTs). Huang et al. [126] used EDC first time to functionalize CNTs by bovine serum abumin (BSA) and this method has became a common process for immobilization of protein on carboxylated CNTs [127][128][129]. The functionalization process can be done in single or two step procedure. In single step functional

group (proteins), CNTs and EDC are mixed at once. However, in this procedure there is a high chance of aggregation and inter-crosslinking between the species in the solution. To avoid these problems, two-step procedure has been developed in which CNTs and EDC are mixed in the presence of NHS (or Sulfo-NHS) to produce a semistable amine reactive NHS-ester. In the second step functional group (proteins) is added to the solution, after removing the excess EDC by washing off or deactivating by adding mercaptoethanol. In this way inter crosslinking between functional groups (proteins) is prevented [130].

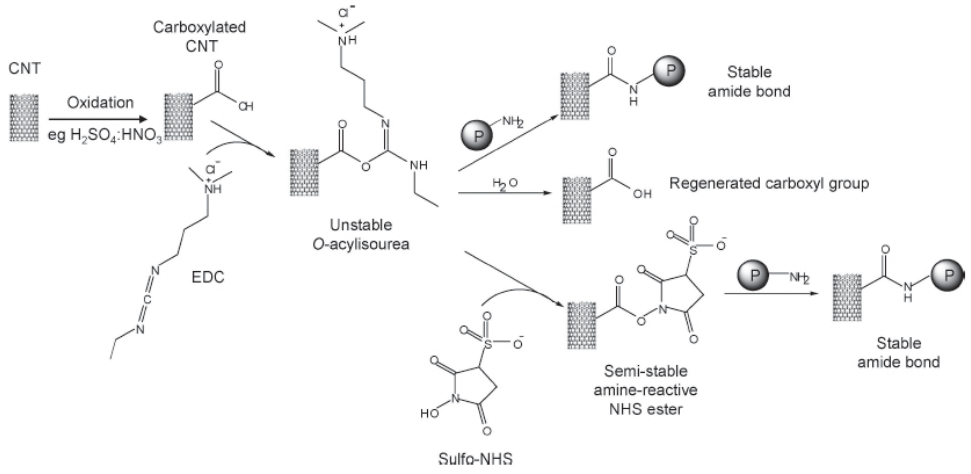

FIGURE 3.9: First EDC reacts with carboxyl groups to form active easter. The active easter can react with amine group and produce a covalent before hydrolysis occurs by water molecules. The unwanted hydrolisis effect can be hindered by adding sulfo-NHS which increase the bonding efficiency significantly. Reproduced from [130].

In this thesis, the conjugation of amine and carboxyl groups with EDC was done in H_2O in a one step process. An annealing step is required to activate the NV centers in diamond which usually is done in oxidizing atmosphere, produces carboxyl groups on diamond surface. A solution of EDC in water was prepared freshly and nanodiamond solution and substrate were added into the solution immediately. Substrates were kept for 6 hours in the solution then washed with water and blast gently with N_2.

Chapter 4

Self-assembly of fluorescent nanodiamonds

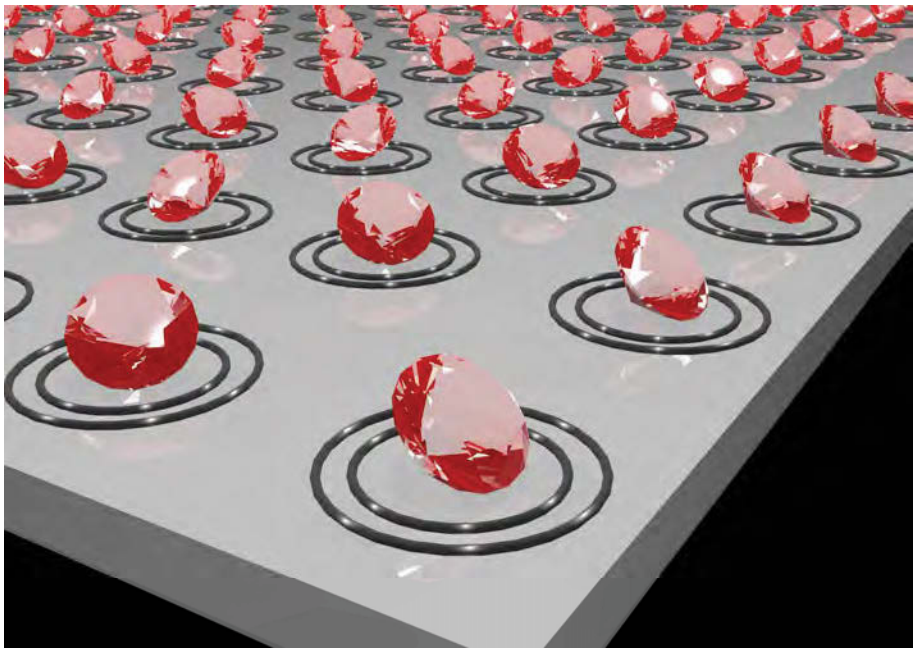

Arrays of fluorescent nanoparticles are highly sought after for applications in sensing, nanophotonics and quantum communications. Here, a simple and robust method of assembling fluorescent nanodiamonds into macroscopic arrays is presented. The yield of this directed assembly process is greater than 90% and the assembled patterns withstand ultra-sonication for more than three hours. The assembly process is based on covalent bonding of carboxyl to amine functional carbon seeds and is applicable to any material, and to non-planar surfaces. These results pave the way to directed assembly of nanodiamond for sensing and nanophotonics devices.

4.1 Introduction

Assembling fluorescent nanoparticles into macroscopic arrays is required for many applications spanning biosensing [49][131] , photonics, plasmonics and quantum information processing [132][52][36]. To achieve this goal several top down techniques, including lithography [133][134] or dip-pen techniques [135][136], as well as bottom up methods using patterned self-assembled monolayers [137], electrostatic self-assembly [55] and DNA origami[138][56] have been developed. While these methods are capable of high resolution patterning of nanoparticle arrays, the assembled components are only weakly bonded to the substrate and cannot undergo further wet chemistry processing steps (eg sonication) or subsequent lithography. Such processing is often required for device applications where the fluorescent nanoparticles act as active components in microfluidic devices [139][51], as sensing probes [13] or photon sources in which they are coupled to plasmonic structures or other optical elements [140].

In particular, there is a great interest in controlling and positioning fluorescent nanodiamonds that host nitrogen vacancy (NV^-) defects, which can then be employed as nanoscale sensors for detection and imaging of weak magnetic fields[49][4][8], thermal imaging or thermometry [141][142][143] and quantum measurements [144][145][146].

Moreover, there is a great interest in assembling arrays of nanodiamonds [147][148] that can subsequently be used to couple to plasmonic waveguides to realize quantum plasmonics circuitry [149][150]. However, unlike gold nanoparticles, which can be assembled into arrays using SAMs and block copolymer templates [151], to date there is no robust method of accurately positioning nanodiamonds in arrays that can be subjected to further processing steps necessary for device fabrication. Here we realize a facile, robust method for high resolution self-assembly of nanodiamonds which enables their use in sensing, photonic and quantum devices. We employ nanoscale seeds that are fabricated in a single step by a mask-free electron beam induced deposition (EBID) technique [104], terminate the seeds with amine groups, and self-assemble nanodiamonds into arrays defined by the seed positions. The technique is not limited to any specific substrate and can be used to position nanodiamonds on arbitrary materials and non-planar surfaces. Finally, the technique offers high stability, which is demonstrated by subjecting the fabricated nanodiamond arrays to multiple sonication steps of up to 12 hours total duration.

4.2 Self assembly of nanodiamonds

The nanodiamond patterning process is illustrated in figure 4.1(a) and described in detail in chapter 3.2. In step 1, electron beam induced deposition (EBID) in a variable pressure SEM was used to fabricate nanoscale carbonaceous seeds using the organic precursor naphthalene ($C_{10}H_8$). Carbon seeds were deposited in arrays on a silicon substrate using a stationary defocused electron beam (15 keV, 300 pA, 30 s), resulting in disks of approximately 90 nm diameter and 20 nm height, as seen in figure 4.1(b) and (c). In step 2, the EBID seeds were amine-functionalized by 45 s exposure to an ammonia plasma generated in a Reactive Ion Etching (RIE) system operating at 100 W and 6 Pa pressure of NH_3. These conditions have been reported to produce the highest concentration of NH_2^- groups in the plasma [152]. The extent and nature of amine groups created in the surface carbon was

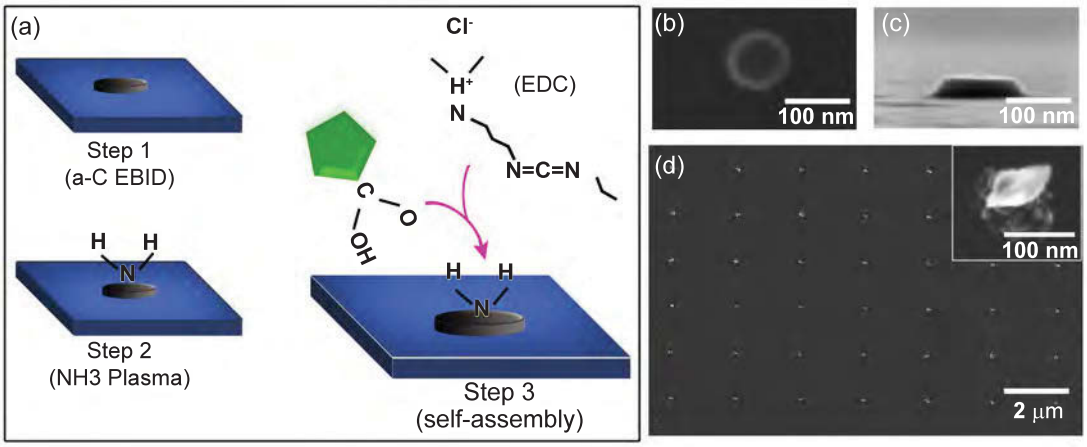

FIGURE 4.1: (a) Schematic of the process composing of three steps: deposition of carbon, ammonia plasma treatment and self-assembly of nanodiamonds. (b) and (c) Plan and side view SEM images of amorphous carbon disks, respectively, deposited by EBID in the first step. (d) SEM image of patterned area after nanodiamond attachment. The inset in (d) is a high magnification SEM image of an carbon disk with attached nanodiamonds.

assessed by X-ray photoelectron spectroscopy and discussed in section 4.6. The final step involves covalent attachment of 35 nm nanodiamonds to the EBID seeds using 1-Ethyl-3-(3-dimethylaminopropyl)carbodiimide (EDC). The presence of dangling bonds at the nanodiamond surface allows them to be functionalized with a variety of ligands [153][154]. The preparation of the nanodiamonds used in the present study are described is detail elsewhere [155]. The surfaces of these nanodiamonds are terminated with carboxylic acid ($-$COOH) groups, enabling their attachment to amine-terminated surfaces through carbodiimide coupling chemistry. Conjugation was achieved by immersing the EBID-seeded Si substrate in an aqueous solution of EDC and varying concentrations of nanodiamonds for 6 hours. Samples were then washed with Deionized (DI) water and dried with gentle blast of N_2. Figure 4.1(d) shows the resulting patterned array of nanodiamonds (the inset shows a high resolution image of a single EBID seed with several nanodiamond crystals attached to it).

4.3 Optical characterization of assembled nanodiamonds

To ascertain the nanodiamond attachment yield and selectivity of the assembly technique, a confocal microscopy was applied to obtain photoluminescence maps and spectra of the fabricated arrays. For the optical measurements, a home built confocal microscope with a high numerical aperture objective (100x, 0.9 NA), used for both excitation and collection of the emitted light was employed. A 532 nm continuous wave laser was used for excitation, and all measurements were done at room temperature under ambient conditions (details in chapter 3.1. Figure 4.2(a) and (b) show a SEM image of a nanodiamond array and the confocal map of the same array, respectively. The bright fluorescent spots correspond to the emission from nitrogen vacancy (NV^-) centers in the nanodiamonds. Variations in PL intensity seen in figure 4.2(b) are caused primarily by the number of nanodiamonds attached to each carbon seed and different population of NV centers within each nanodiamond. Figure 4.2(c) is the histogram obtained from confocal scan of figure 4.2(b), representing the variation of fluorescence in a pattern produced with this method. Figure 4.2(d) shows the spectrum recorded from each spot, demonstrating that 32 out of 35 locations have the characteristic emission of the NV^- centres, equating to a 92% yield for the attachment process. Note that no nanodiamonds were attached in between the EBID seeds, giving the technique 100% selectivity.

4.4 Efficiently of the aseembly technique

IN this work, the effect of the nanodiamond concentration on the attachment yield was also studied. Figure 4.3(a) shows a clear dependence of the yield on the initial

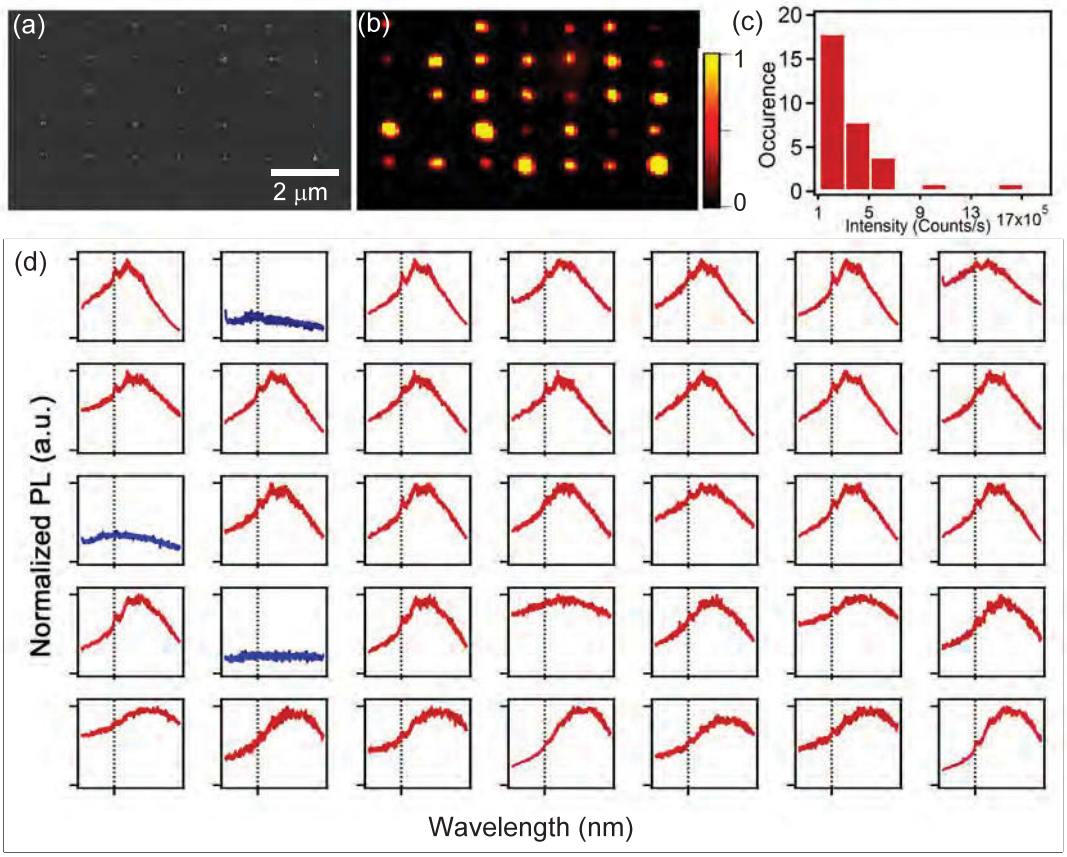

FIGURE 4.2: (a) SEM image of a nanodiamond pattern. (b) Color-coded confocal photoluminescence map of the same nanodiamond pattern in (a). (c) Histogram of the PL intensities from each spot in the confocal map. (d) Corresponding normalized PL spectrum from each individual spot in the confocal map showing the NV^- emission at 637 nm (red curve). The NV zero phonon line is marked with a vertical dashed line for clarity. The adjacent broad emission is the phonon sideband. Only three locations in the patterned array did not show the emission from NV (blue curves).

concentration of fluorescent nanodiamonds in the solution. Increasing the nanodiamond concentration resulted in higher attachment yield. At a nanodiamond concentration of 2.5 $\mu g/ml$ the attachment yield was less than 5% which increased to 50% at a concentration of 12.5 $\mu g/ml$. The optimum concentration was found to be 25 $\mu g/ml$, resulting in more than 92% attachment yield, with only a few spots having no nanodiamonds. A higher concentration of nanodiamonds resulted in agglomeration with no increase in the attachment yield. The probabilities were deduced by analysis of confocal maps recorded under the same conditions as in figure 4.2

(and shown for each data point in figure 4.3(a)). For all experiments, the ratio of EDC:nanodiamonds in the solution was fixed at 10:1.

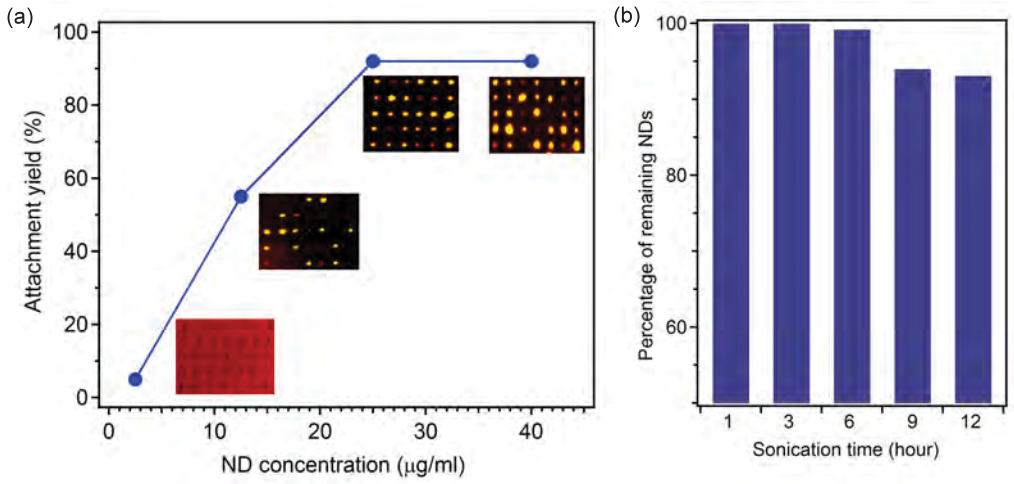

FIGURE 4.3: (a) Effect of nanodiamond concentration on the attachment yield. The yields were calculated from confocal maps shown next to each data point. (b) Percentage of the nanodiamonds which remained on their spot after sonication. Pattens consist of 49 carbon disk with attached nanodiamond were examined and in all cases nanodiamonds remained on their position after 3 hours of sonication.

The effectiveness of the assembly method relies on covalent bonding between the amine and carboxyl functional groups on amorphous carbon and nanodiamond surfaces in the presence of EDC. Therefore, it is expected the attached nanodiamonds to withstand further processing and treatment, as is required for many device applications. To examine the robustness of the technique, the assembled nanodiamonds were sonicated in a powerful ultrasonic bath (Bransonic 185 W Ultrasonic cleaner 221). Figure 4.3(b) shows the percentage of nanodiamonds remaining on their position after multistep ultra-sonication for up to 12 hours. After three hours of sonication, all the nanodiamonds that were initially assembled were still attached to the substrate. Even after 12 hours, more than 90% of the self-assembled nanodiamonds remained on the surface, proving the unprecedented robustness of the assembly technique.

4.5 Assembly of nanodiamond on Si_3N_4

In order to investigate the possibility of extending the technique to other substrates, the process was tried with silicon nitride (Si_3N_4). As nanodiamonds conjugate to the carbon surface on top of substrate surface, in general, the proposed process can be extend to other substrates. The only restriction from EBID step is the limitation of using insulating substrates inside the SEM. To explore this, the assembly of nanodiamonds on Si_3N_4 substrates was done following the same procedure. Although Si_3N_4 is an insulator, it is possible to image a very thin film of this material. A 50 nm thick Si_3N_4 substrate were loaded into the SEM and patterned with carbon disks via EBID. Assembly of nanodiamonds was achieved in 25 $\mu g/ml$ of nanodiamond solutiona after amine functionalization step with Ammonia plasma process. An SEM image of assembled nanodaimond is shown in figure 4.4 proving that the process can be extended to other substrates and even other materials.

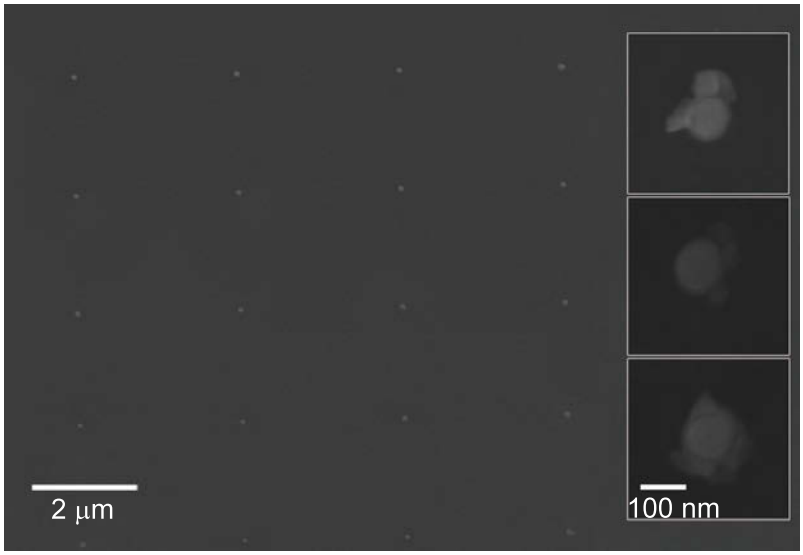

FIGURE 4.4: SEM image of nanodiamond on Si_3N_4 substrate patterned with the proposed process. The insets show high resolution image of representative carbon disk with attached nanodiamond. Note that low quality of the SEM images from Si_3N_4 is due to the charging effect during SEM imaging of the samples.

4.6 Selectivity of the assembly process

The selectivity of the nanodiamond attachment was tested in large area assembly as well. Although EBID step is a localized process, the plasma step is affecting the whole sample. Therefore, it is important to realize the selectivity of the plasma process. If this step causes Amine-terminated surfaces both on the carbon and oxide layer (native oxide layer on silicon), it is not possible to developed patterns with nanodiamonds with 100% selectivity. Figure 4.5 shows the assembly of nanodiamonds on larger scale. Carbon was deposited using sputtering and hard masks. SEM images of two samples with after assembly process are shown in figure 4.5(a) and (b). Confocal mapping of a representative area of the sample shows the attachment of nanodiamonds only occurred on carbon and the surface of silicon remained free of nanodiamond attachment (figure 4.5(c)). The presence of nanodiamonds on carbon coated area was also confirmed with charachterisic emission of NV centers in nanodiamond shown in figure 4.5(d).

X-ray photoelectron spectroscopy (XPS) was used to establish the effectiveness of the plasma process for amination of the carbon surface. The chemical bonding of the surfaces were assessed by using a Specs 150 SAGE instrument operated with a Mg K_α X-ray source (Mg anode operated at 10 keV and 10 mA). The $C1s$ peak at 284.6 eV was used as a reference to compensate for any surface charging. Figure 4.6 shows the XPS measurement from the ammonia plasma treated carbon layer on top of silicon substrate.

An oxidized silicon substrate was sputtered with carbon and the sample was exposed to NH_3 plasma for 30 seconds. XPS measurement was performed on both the clean SiO_2/Si and carbon- coated surface. Figure 4.6 shows the deconvolution of the XPS $C1s$ peaks obtained from the surface modification of sputtered carbon without (figure 4.6(a)) and with (figure 4.6(b)) ammonia plasma treatment, along with the XPS $N1s$ peak (figure 4.6(c)), which was observed only for the sputtered carbon after ammonia plasma treatment. The $C1s$ spectrum of both samples show four

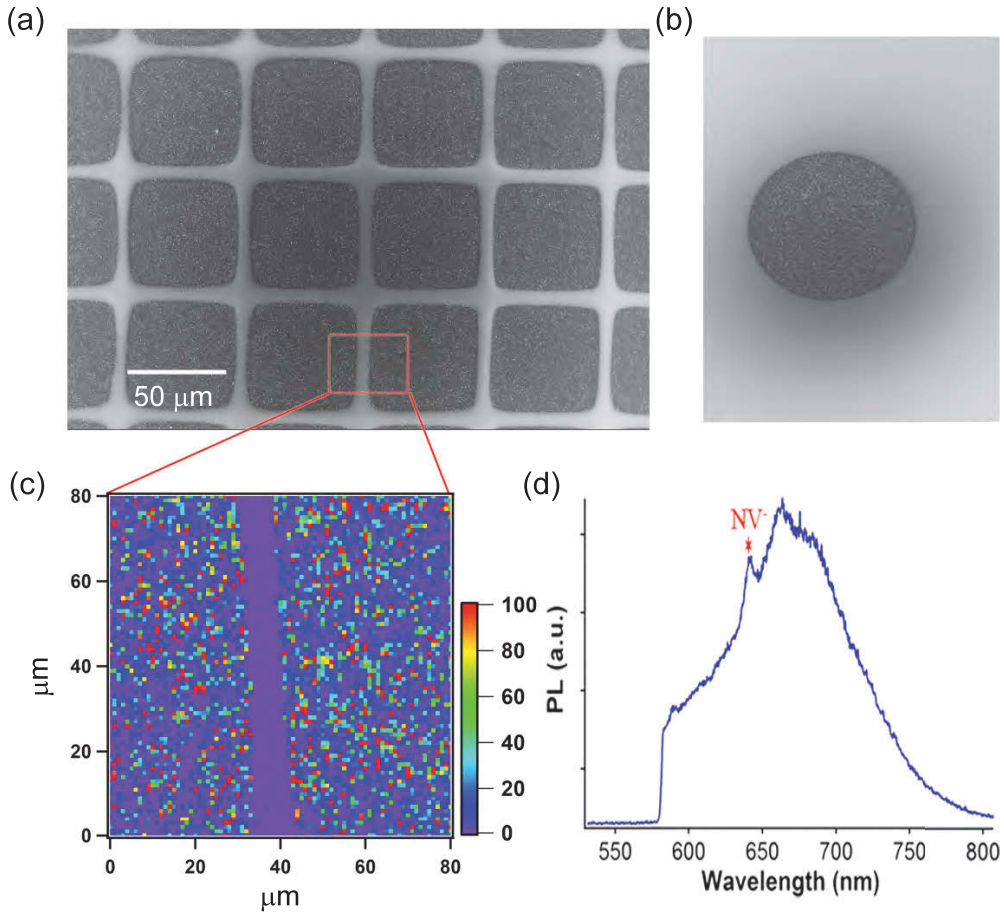

FIGURE 4.5: (a) and (b) SEM image from assembly of nanodiamond on large areas. (c) confocal map of an area of the sample as indicated by red box in SEM image shown in (a). No fluorescene was detected from silicon surface. (d) PL spectrum from bright spots on the carbon area revealed the characteristic emission of NV centers confirming the assembly of nanodiamond on carbon coated area.

peaks with bonding energies of 284.6 eV, 285.2 eV, 287.9 eV and 290.1 eV, which were assigned to C-C, C=C, C=O and C–F, respectively. For both samples a single $F1s$ peak was also observed at 686 eV (data not shown), which is consistent with the C–F bond and likely results from prior processing under fluorine gas in the same chamber). The $N1s$ spectrum after ammonia plasma treatment clearly shows the presence of amino groups at the surface of the plasma treated carbon. The XPS data demonstrates that this procedure is highly selective, resulting in amine functionalization only of the sputtered carbon, while the surrounding SiO_2/Si surface remains oxygen-terminated. In addition, XPS reveals that the ammonia plasma

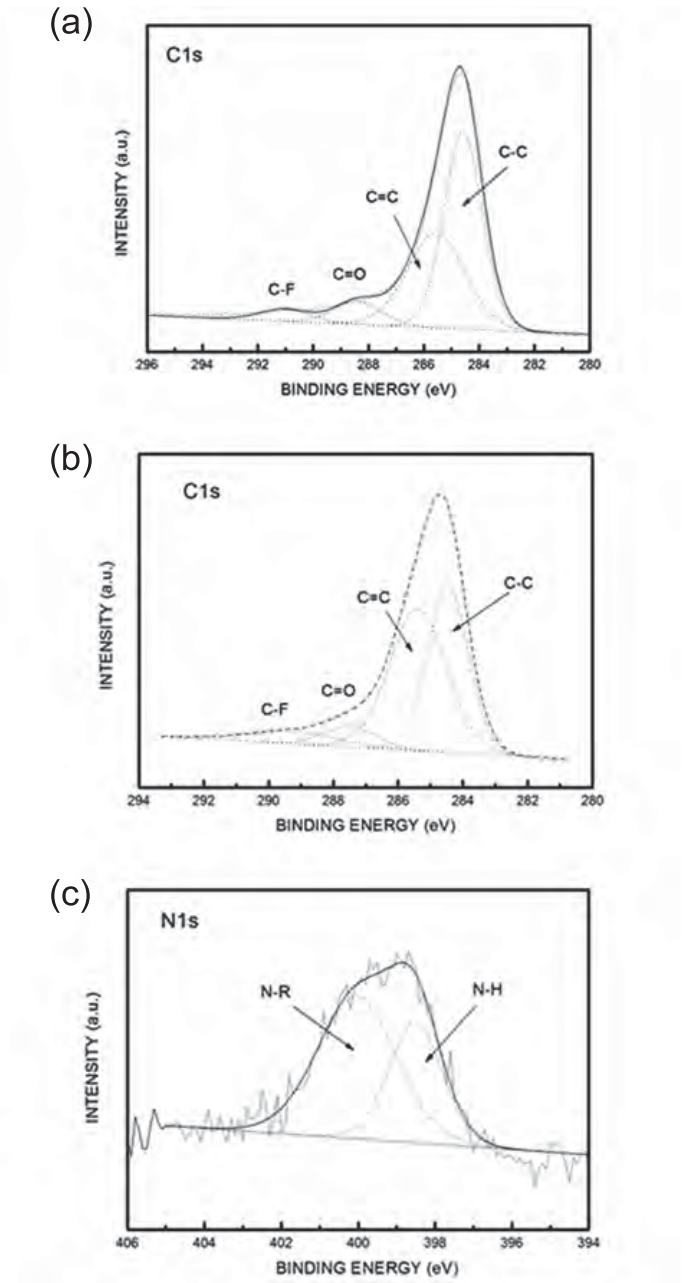

FIGURE 4.6: (a) and (b) $C1s$ XPS spectrum of deposited carbon before and after plasma process, respectively. (c) $N1s$ XPS spectrum of deposited carbon after ammonia plasma treatment.

treated carbon contains both amine and amide groups, both of which are suitable for coupling to carboxyl groups on the nanodiamond surface using carbodiimide conjugation.

4.7 Power broadening in ODMR measurement

Increasing the microwave power or excitation power in general can results in better signal to noise ratio which in turn can improve the sensitivity of the ODMR measurement. However, higher excitation power will cause broadening of the lines. The broadening of the lines can be reduced significantly using pulses scheme [99]. figure 4.7 shows the effect of microwave power in broadening of the ODMR lines in the absence of magnetic field. Fit to the curves has been done using multiple Lorentzian as a guide for the eye. Splitting of the ODMR peaks are the results of local strain in the structure which affect differently the NV centers with random orientation in the structure, causing the complex ODMR peaks.

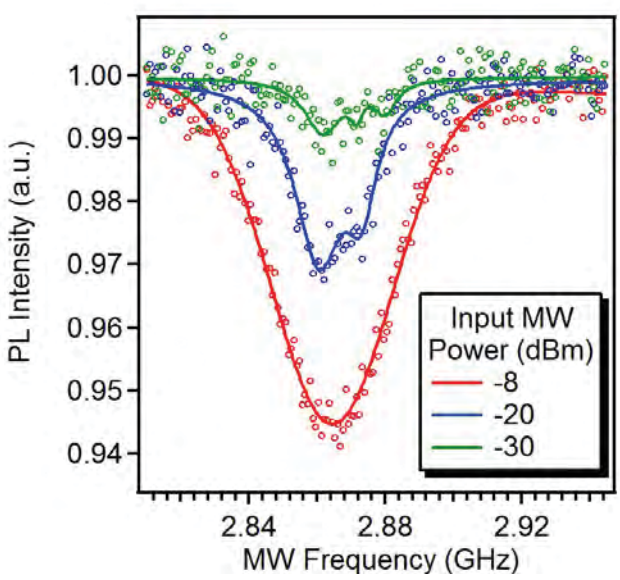

FIGURE 4.7: Brodening of the ODMR signals in the absent of magnetic field due to the microwave power.

4.8 Magnetic field sensing

Finally, it was demonstrated that the formed array can be used as a high-resolution magnetic field sensor, where each element in the array can serve as an individual

pixel. Here, a microwave is guided through a 30 μm wire and the NV centers spin states were read out optically (so-called optically detected magnetic resonance, ODMR, described in 2.2 (Figure 4.8(a)) [45]. Such sensing of magnetic fields in ambient environments is one of the most prominent applications of the NV-centre. Figure 4.8(b) is a confocal map of the array of NV centers used for sensing magnetic field. Figure 4.8(c-e) shows three examples of ODMR measurements from randomly selected pixels in the array (marked with green circles). The red curves are nearly identical for all pixels and correspond to zero magnetic field. The green and the blue curves show the ODMR under 1 mT and 3 mT magnetic field. Each pixel shows a distinct ODMR signal that can then be used to deduce the local magnetic field in the proximity of the pixel. Note that since the measurement is done with an ensemble of nanodiamonds, the signal is broadened, with each dip comprising several lines from different NV centers at each spot in the array (see chapter 2.2). This technique is ideal to test for local absorption of metal nanoparticles or the presence of foreign para- and ferromagnetic metals. In principle, this technique can also be applied to nanodiamonds with single emitters, which are advantageous for quantum photonic applications.

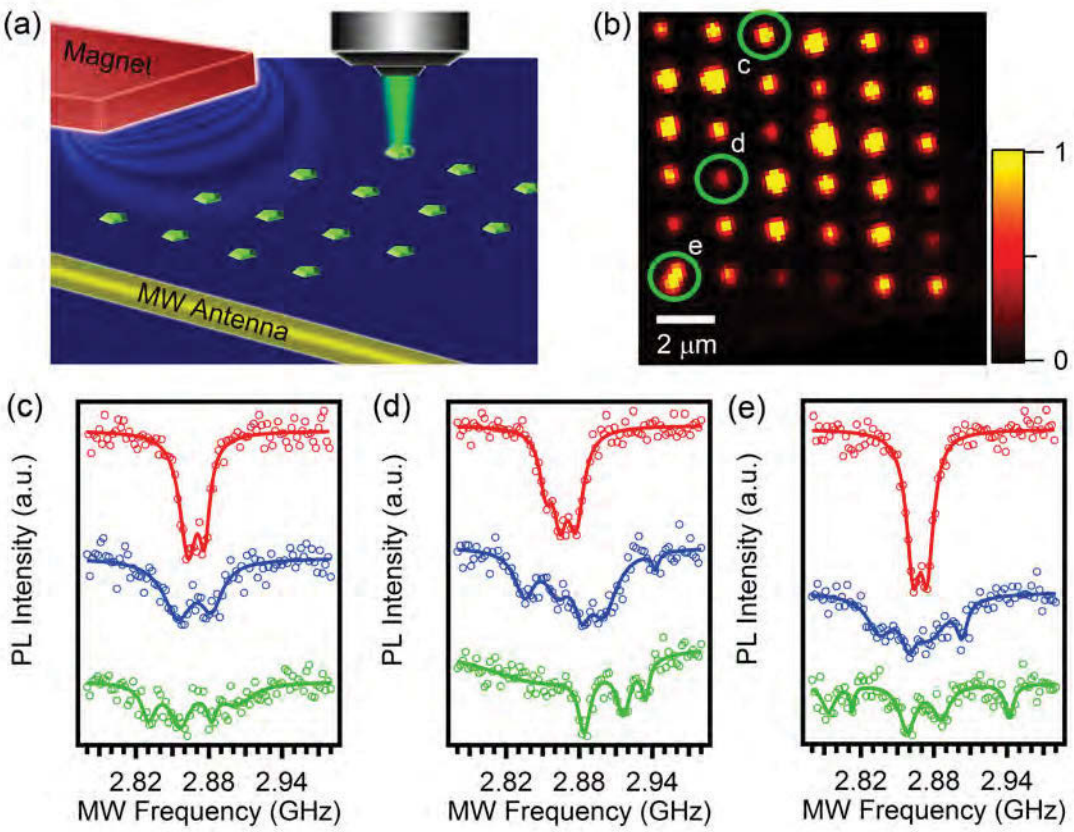

FIGURE 4.8: (a) Schematic of the measurement. Microwave is guided through a 30 μm wire and electron spins are read out optically from individual nanodiamond (sensor pixel). (b) confocal map of the nanodiamond assembly into an array. (c-e) Optically detected magnetic resonances (ODMR) signal recorded from different representative pixels marked by green circles. Red curve is ODMR under zero external magnetic field while blue and green curves correspond to 1 and 3 mT fiels, respectively.

4.9 Conclusion

In conclusion, a facile, generic technique for directed assembly of fluorescent nanodiamonds into robust arrays has been developed. The assembly technique has greater than 90 percent efficiency. Moreover, the nanodiamonds are covalently bonded and stay in their positions even after repeated ultrasonication treatments, making the technique very attractive for practical device applications. Finally, a proof of principle sensing measurement of various magnetic fields has been performed to show that each pixel in the array can be used as an independent magnetic field sensor. This method paves the way to realization of scalable platforms for sensing or integrated quantum photonics, where there is a real need for large area assembly of fluorescent nanoparticles. It is important to note that while applied to nanodiamonds in this work, the technique is versatile and can be used to assemble other nanoparticles on arbitrary surfaces.

Chapter 5

hBN quantum emitters for high temperature applications

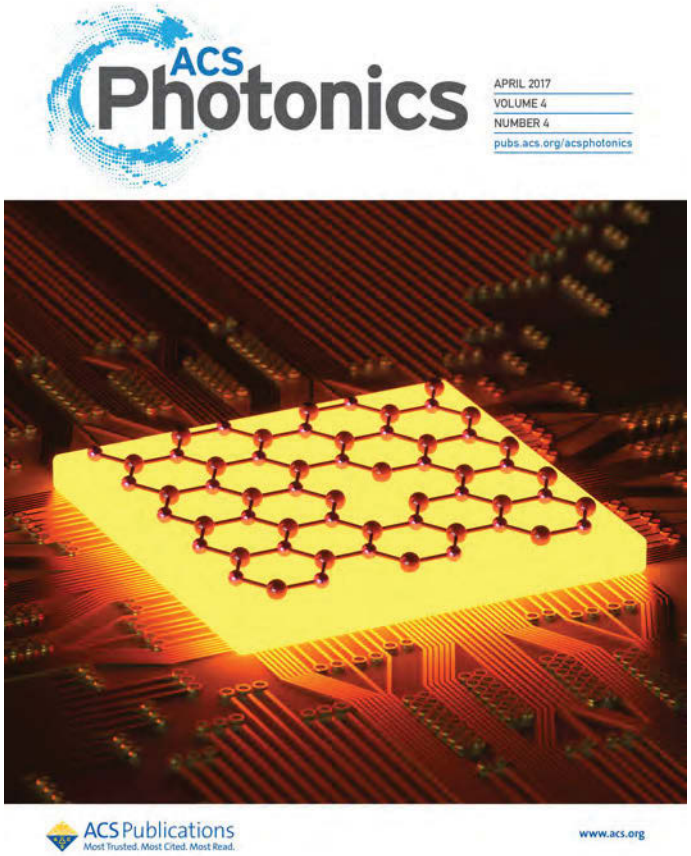

Realization of Quantum information and communications and sensing technologies requires robust, stable solid state single photon sources. However, most existing sources cease to function above cryogenic or room temperature due to thermal ionization or strong phonon coupling which impede their emissive and quantum properties. Here, an efficient single photon source is presented based on a defect in a van der Waals crystal that is optically stable and operates at elevated temperatures of up to 800 K. The quantum nature of the source and the photon purity are maintained upon heating to 800 K and cooling back to room temperature. The report of a robust high temperature solid state single photon source constitutes a significant step towards practical, integrated quantum technologies for real-world environments.

5.1 Introduction

Modern light-based technologies require sophisticated materials growth and device engineering techniques to achieve optimum performance under ambient conditions. Optically active defects in solids are a vital part of numerous such technologies spanning light emitting diodes (LEDs)[9][10], lasers [11], sensors [13] and communications [14]. An emerging application of localized individual defects is their use as single photon sources (SPSs) in integrated nanophotonics and quantum information processing schemes that utilize individual photons as information carriers [35][156][157]. For such applications to become a reality there is an urgent need for robust SPSs. Furthermore, these sources should withstand temperature variations and be optically active at elevated temperatures that are typical of high density integrated circuits. Hence, over the last decade, research into solid state SPSs – quantum dots (QDs) and color centers – has accelerated dramatically. Quantum dots mostly operate only at cryogenic temperatures because of low carrier binding energies and thermal ionization at elevated temperatures [15][16]. On the other hand, color centers in solids (defects and impurities) often have deep electronic states that enable SPS operation near room temperature (RT)[158][17][159]. However, both QDs and color centers

typically suffer from efficient coupling between electrons and lattice phonons that results in an overall reduction of brightness at higher temperatures. In this chapter, a solid state SPS that operates at temperatures as high as 800 K is reported. The SPS maintains its quantum nature during a high temperature thermal cycle – that is, the photon purity (defined as the fraction of single photon emission events) does not decrease upon heating, and the SPS optical properties are preserved after heating up to 800 K and cooling back to room temperature. The SPS is a deep trap defect in layered hexagonal boron nitride (hBN) – a van der Waals crystal with a wide indirect bandgap of about 6 eV [160] and favorable thermal, chemical and mechanical properties [161][162]. The recently-discovered SPSs in hBN are extremely bright, chemically stable, fully polarized, and exhibit a broad range of emission colors. Given the two dimensional (2D), layered nature of hBN and the extreme thermal stability of the SPSs demonstrated here, fabrication of hybrid photonic systems is a promising potential path to high density integrated circuits designed to withstand heating that occurs during operation at RT [163][157][23].

5.2 Properties of the single photon source

A schematic illustration of hBN on a hot substrate is shown in figure 5.2(a). The sample consists of a few-layer flake of atomically thin hBN bonded by van der Waals forces. Atomic force microscopy scans are demonstrated in the figure 5.1. The average thickness of the flakes is 4 nm which is equivalent to about 10 layers considering the thickness of hBN monolayer is 0.42 nm [164]. The hBN flakes (Graphene Supermarket) were dropcast onto a silicon wafer and annealed in a tube furnace at 850 $°C$ for 30 minutes under 1 $Torr$ of Argon to activate the single photon sources (SPSs) [30]. To perform the heating experiments, a purpose-built vacuum chamber with a thin quartz window and a long working distance, high numerical aperture (0.7) objective was used which is shown in figure 5.2(b). Design and details of the champer used in this study are provided in appendix A. The samples were mounted

on a pyrolitic boron nitride heater, and the temperature was measured using a thermocouple fixed to the silicon substrate. Having the thermocouple a few millimeters away from the hBN on top of a silicon substrate in vacuum yields a temperature uncertainty of approximately 5 degrees. The system was let into equilibrate at each temperature set point to ensured that the temperature did not drift during data acquisition. A turbo molecular pump was used to achieve a base pressure of $\sim 1 \times 10^{-6}$ $mBar$, and a 532 nm laser was used as the excitation source in the confocal photoluminescence setup. For all measurements except time-resolved photoluminescence, the laser power was fixed at 3 mW (measured before the window of the chamber, the laser spot is $\sim$ 900 nm with the power density of 4.7 $mW/\mu m^2$). The collected light was filtered using a 532 nm dichroic mirror and an additional long pass filter. The collected light was sent either to a spectrometer (Acton Spectra ProTM, Princeton Instrument Inc.) equipped with a 300 $lines/mm$ grating and a charged-coupled device (CCD) detector with a resolution of 0.14 nm or to a Hanbury Brown and Twiss setup for single photon correlation measurement (figure 5.2(c)). The emitted light was coupled to an optical fiber and split to two paths into avalanche photodiodes in order to perform correlation measurements using a time correlated single photon counting module (Picoharp 300, PicoQuantTM). Lifetime measurements were done with a 510 nm pulsed laser excitation source at 30 μW power with a 100 ps pulse width and 10 MHz repetition rate (details in Chapter 3.1).

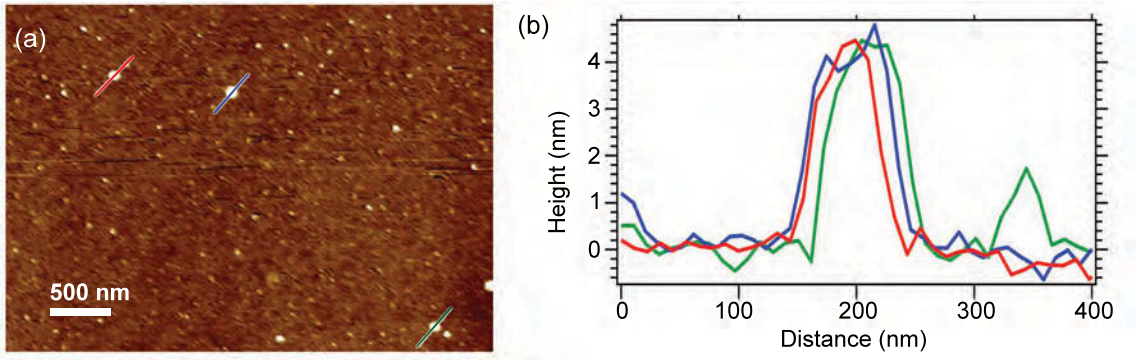

FIGURE 5.1: (a) AFM image from hBN flakes on silicon after annealing. (b) High resolution line scan of 3 flakes marked with red, blue and green color in (a).

Two SPSs in different hBN crystals were studied in this work. Figure 5.2(d) shows RT photoluminescence (PL) spectra recorded from the SPSs. The spectrum from SPS #1 consists of two peaks at $\sim 1.94\ eV$ and $\sim 1.78\ eV$ attributed to the zero phonon line (ZPL) and the phonon side band (PSB), respectively [58]. SPS #2 has a sharper ZPL centered at $\sim 1.75\ eV$, and a negligible PSB (the emissions beyond $\sim 1.8\ eV$ are background). These particular two emitters were selected for the present study because their spectra are representative of the emission spectrum diversity that has been observed previously in hBN (2.7) in terms of ZPL width and position, and PSB intensity [58].

5.3 Operation of SPSs at high temperatures

After reliable SPSs were identified, the heating experiment were performed inside the designed chamber. The temperature-dependence of each SPS was characterized by measuring its photophysical properties at 100 K increments during a 300 K – 800 K – 300 K thermal cycle. Figure 5.3 (a), (b) and figure 5.3 (c), (d) show autocorrelation functions and normalized PL spectra obtained from SPS #1 (blue data set) and SPS #2 (red data set) obtained during the heating phase of the thermal cycle, respectively.

Equivalent data acquired during cooling are shown in figure 5.4. The single photon emission persists all the way to 800 K, and the $g^2(0)$ values are independent of temperature, as is discussed below. The data show unambiguously that both sources are stable and can operate during and after exposure to temperatures as high as 800 K. The spectra red shift and broaden with increasing temperature, and the changes are reversible upon cooling back to RT (figure 5.4), demonstrating that the SPSs are not compromised by the thermal cycle. At 800 K, the ZPLs are centered at ~ 1.90 eV and 1.72 eV, and have a FWHM of $\sim 80\ meV$ and 70 meV for SPS #1 and SPS #2, respectively.

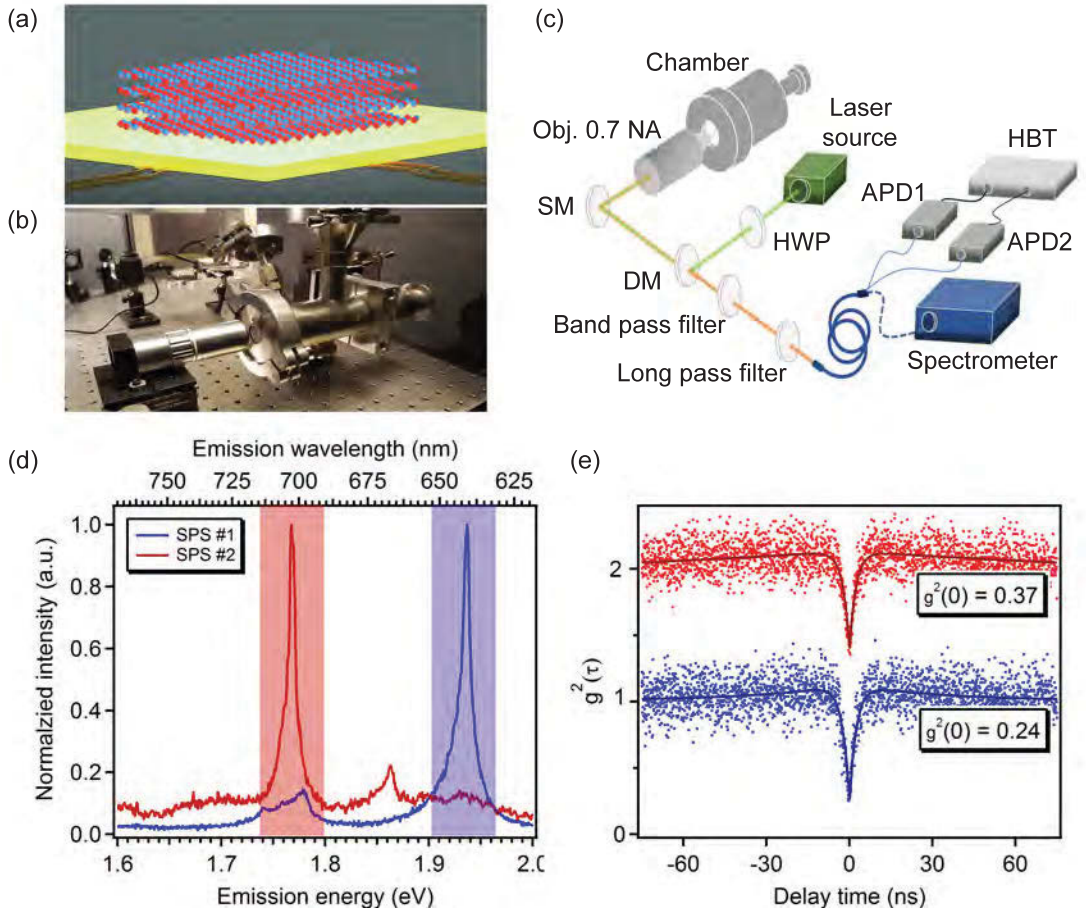

FIGURE 5.2: (a) Schematic illustration of hBN crystal hosting a single photon source atop a heated substrate. (b) Purpose-build vacuum chamber setup used in this study. (c) Hanbury Brown and Twiss setup equipped with vacuum chamber used in this study. The band-pass filter was selected to match the ZPL energy and was used only for coincidence measurements. (d) Room-temperature PL spectra acquired from two representative SPSs in hBN. The shaded areas represent the filtered regions used to record correlation data. (e) Antibunching behavior of the sources demonstrated by autocorrelation function with $g^2(\tau = 0)$ values of 0.24 and 0.37 for SPS #1 (blue) SPS #2 (red), respectively, confirming the quantum nature of the emission. The $g^2(\tau)$ from SPS #2 was offset for clarity. The data were fitted with a three-level model (solid curves).

To characterize the photon emission statistics and show the quantum nature of the SPSs, second order autocorrelation functions, $g^2(\tau) = (< I(t)I(t+\tau) >)/ < I(t) >^2$, were acquired using a Hanbury Brown and Twiss (HBT) interferometer. The shaded rectangles in figure 5.2(d) represent the filters used to collect the photons in the autocorrelation measurement. Figure 5.2(e) shows the $g^2(\tau)$ curves recorded

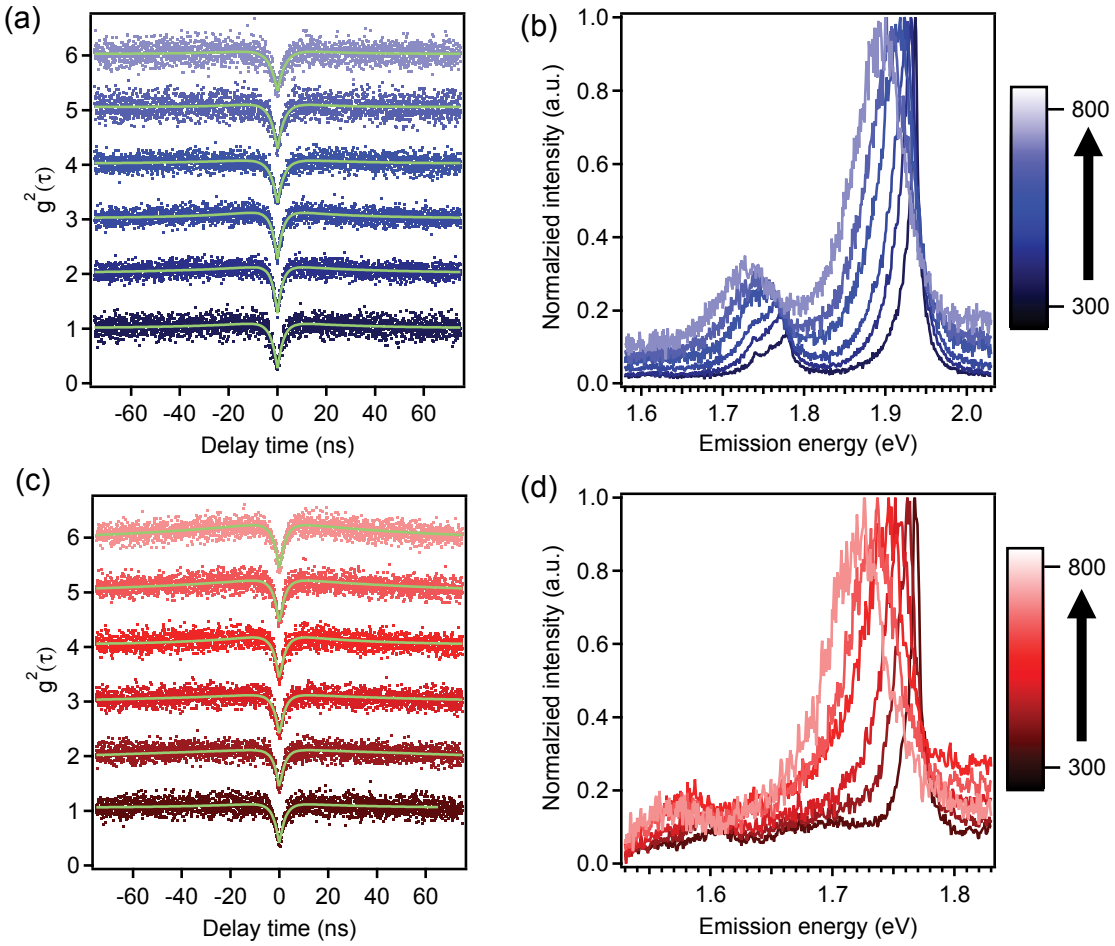

FIGURE 5.3: (a) Autocorrelation curve and (b) normalized PL spectrum measured from SPS #1 at 100 K intervals between 300 and 800 K. (c) and (d) are Equivalent data from SPS #2. The autocorrelation data in (a) and (c) were offset for clarity. Green solid curves are fit obtained using a three-level model.

from each source at RT and fitted using a three level model (this model is commonly used to describe quantum emitters, including the ones from hBN [30]). The anti-bunching dip below 0.5 at zero delay time ($\tau = 0$) constitutes proof for the quantum nature of a photon source. The raw (uncorrected) values of $g^2(0)$ are 0.24 and 0.37 for SPS #1 and SPS #2, respectively. The autocorrelation data were background corrected using the procedure described in reference [165]. Signal to background ratios (S/B) were calculated based on the counts acquired when the excitation laser was focused on the source and when it was focused on the adjacent silicon substrate. The signal and background were measured at each temperature and the corrected

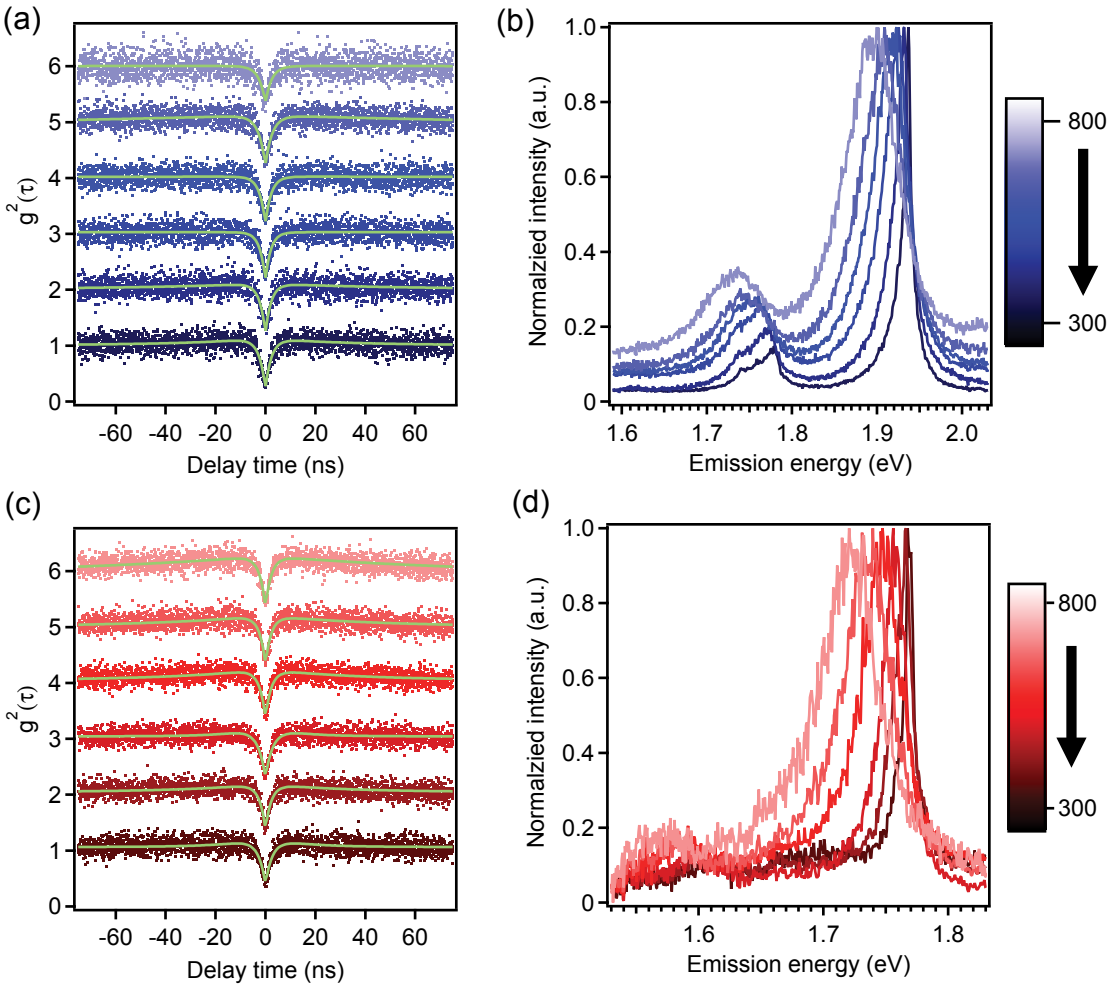

FIGURE 5.4: (a) Autocorrelation curve and (b) normalized PL spectrum measured from SPS #1 at 100 K intervals between 300 and 800 K. (c) and (d) are Equivalent data from SPS #2. The autocorrelation data in (a) and (c) were offset for clarity. Green solid curves are fit obtained using a three-level model

coincidence (g_c^2) was obtained using the equation, $g_c^2(\tau) = (g^2(\tau) - (1-\rho^2))/\rho^2$, where ρ is the signal-to-noise ratio $S/(S+B)$ and $g^2(\tau)$ is the uncorrected photo-coincidence. The background corrected autocorrelation data suggest that the deviation from $g^2(0) = 0$ in raw values is due to residual background. The excited state lifetime was measured using a pulsed laser, and fitted with a single exponential function. The individual measurements and fitted data is discussed later in 5.5. The lifetime value remained almost the same, around 3.6 ns, at all temperatures for both sources (figure 5.5(a) and (c), suggesting new none radiative channels are not

created. In addition, both sources were stable and no blinking was observed at any temperature during heating to 800 K or cooling back to RT (figure 5.5(b) and (d).

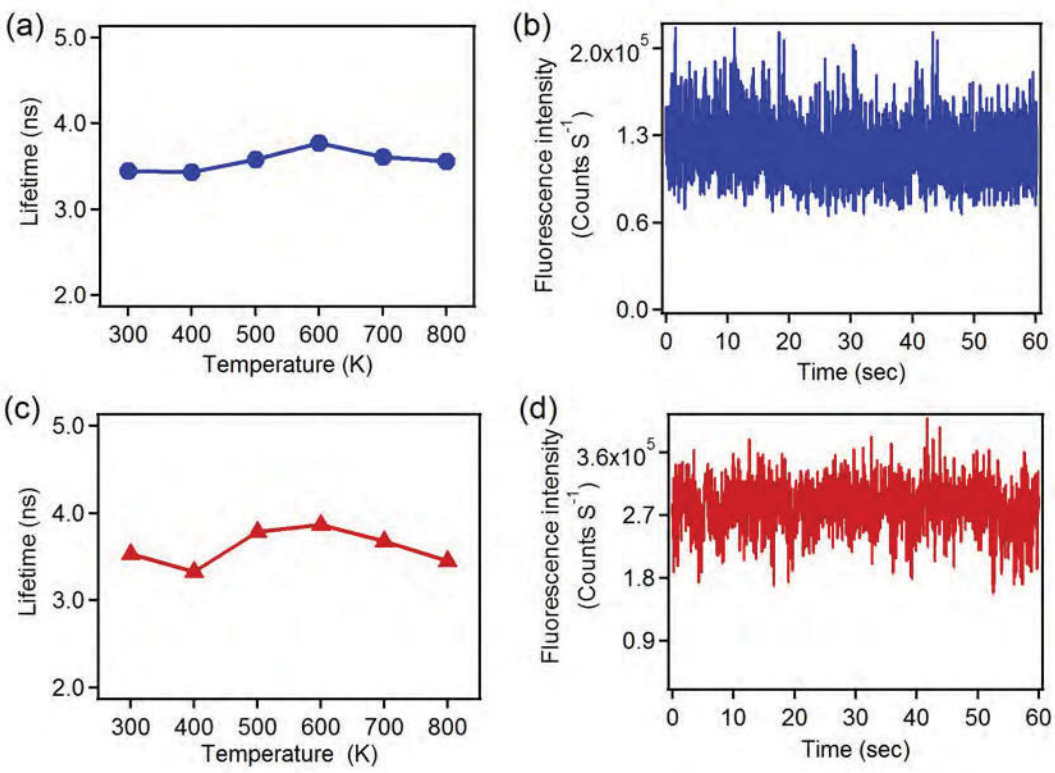

FIGURE 5.5: (a) Fluorescence lifetime of SPS #1 measured at 100 K increments between 300 and 800 K. A 30 μW, 510 nm pulsed laser was used as the excitation source. (b) Normalized fluorescence of SPS #1 at 800 K for 60 s showing the photostability of the source. (c) and (d) Equivalent data for SPS #2.

5.4 Efficiency and purity of single photon source

To analyze the efficiency and purity of the sources, $g^2(0)$ is plotted as a function of temperature for SPS #1 and SPS #2 in figure 5.6(a) and (d), respectively. The data were collected during both the heating (full symbols) and cooling ("+" and "×" symbols) phases of the thermal cycle for each SPS. The results show that the photon purity is constant over the entire temperature range. The background-corrected $g^2(0)$ for each source (light blue, and light orange) is also constant across the entire temperature range and remains below 0.1. To the best of my knowledge,

these temperatures are the highest reported for a stable, operating quantum system, surpassing other materials systems, such as gallium nitride, by more than 400 K [166][167]. It must be noted that the scatter in the raw $g^2(0)$ values seen in figure 5.6(a) and (d) is caused by thermal drift (and hence drift in the background intensity) during data acquisition.

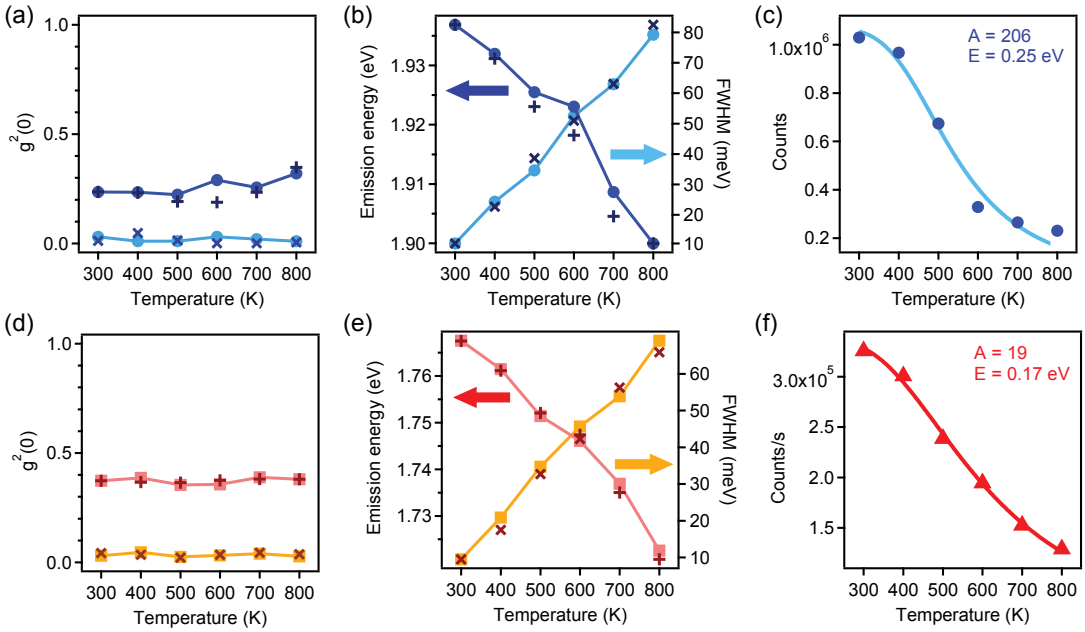

FIGURE 5.6: (a) Coincidence counts at zero delay time, $g^2(0)$ (blue circles), and the background-corrected values (light blue circles) obtained for SPS #1 as a function of temperature during the heating phase of thermal cycle. Corresponding values obtained during the cooling phase are shown as "X" and "+" symbols. (b) Zero phonon line (ZPL) position (left) and width (right) plotted as a function of temperature during heating and cooling . In (a) and (b) the solid lines are guides to the eye. (c) ZPL intensity versus temperature for SPS #1 (blue circles). The data are fit using equation 5.1 (solid curve). (d),(e) and (f) Equivalent data for SPS #2. Marker size represents $g^2(\tau = 0)$ uncertainties

To further analyze the effects of temperature on the optical properties of both SPSs, the ZPL energy, linewidth, and intensity as a function of temperature are recorded. The ZPL position of each source red shifts by $\mu 40\ meV$ upon heating to 800 K (figure 5.6(b), (e). A red shift is expected and attributed primarily to expansion of the substrate lattice upon heating, and electron-lattice interactions [168]. In principle, these SPSs can be used for wide range temperature sensing with high

spatial resolution. The ZPL linewidth broadened at a linear rate of 0.13 $meVK^{-1}$ and 0.11 $meVK^{-1}$ for SPS #1 and SPS #2, respectively (figure 5.6(b) and (e), which is caused primarily by interactions with lattice phonons [68]. The ZPL red-shift and broadening are reversible upon cooling back to room temperature, as shown by "×" and "+" symbols in figure 5.6(b) and (e).

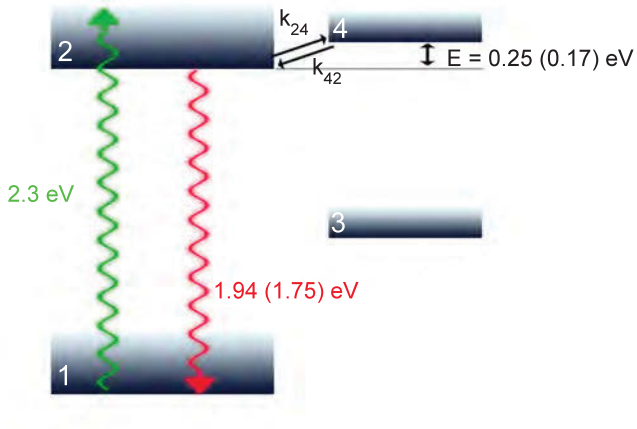

FIGURE 5.7: The ground and excited states are labeled 1 and 2, 2.3 eV is the excitation energy used in the experiment, 1.94 eV (1.75 eV) in the ZPL energy of SPS #1 (SPS #2), E is the activation barrier in equation 5.1, which equals 0.25 eV (and 0.17 eV) for SPS #1 (SPS #2), and k_{24} and k_{42} signify transition rates between states 2 and 4. The nonradiative recombination pathway proceeds through states 2,4 and 3.

The ZPL intensity decreases by a factor of 5 and 2 upon heating to 800 K for SPS #1 (figure 5.6(c)) and SPS #2 (figure 5.6(f)), respectively. A decrease is expected due to an increase in the efficiency of competing non-radiative recombination pathways with increasing temperature. Assuming one nonradiative pathway with activation energy E, the dependence of ZPL intensity (I) on temperature (T) can be described by [169]:

$$I = \frac{I_0}{(1 + exp(-E/K_bT))} \tag{5.1}$$

Here, I_0 is the emission intensity at 0 K, A is a system-specific pre-exponential factor related to the nonradiative transition rate in the limit $E \rightarrow 0$, and k_b is

Boltzmann's constant. Figure 5.7 shows a four level system used to explain the temperature-dependence of SPS #1 and SPS #2 in the framework of equation 5.1. The experimental data from each source can be fit well using equation 5.1 (solid lines in figure 5.6(c), (f) only if both E and A are varied. The activation barriers are high in both cases ($E \sim 0.25\ eV$ and $\sim 0.17\ eV$ for SPS #1 and SPS #2, respectively) as expected, since bright luminescence is observed from both sources even at 800 K. However, the barriers do not explain the difference between the quenching rates of the two SPSs seen in figure 5.6(c) and (f) which is instead caused by a large difference in the pre-factor A which is related to the transition rates k_{24} and k_{42} shown in figure 5.7 (~ 206 and ~ 19 for SPS #1 and SPS #2, respectively). The cause of the large difference in A is likely related to the diversity of emission spectra observed from SPSs in hBN (exemplified by the spectra in figure 5.2(d)), which is not fully understood, but has been suggested to be caused by variations in local dielectric environment, strain defect charge state or defect structure [58][68][64].

5.5 Lifetime measurements of the SPSs

PL emission lifetime was measured for each SPS using a 510 nm pulsed laser excitation source at 30 μW power with a 100 ps pulse width and 10 MHz repetition rate. For each SPS the time resolved PL was obtained at each temperature during heating and fitted with double exponential function to extract the lifetime values. The first component of the double exponential function was fixed as a system response of about 500 ps. The second component of the double exponential function was attributed to the SPSs lifetime. Time resolved PL data and lifetime values for SPS #1 have been shown in figure 5.8 at each temperature. Figure 5.9 depicts equivalent data for SPS #2. Both sources have lifetime of about 3.5 ns at all temperatures.

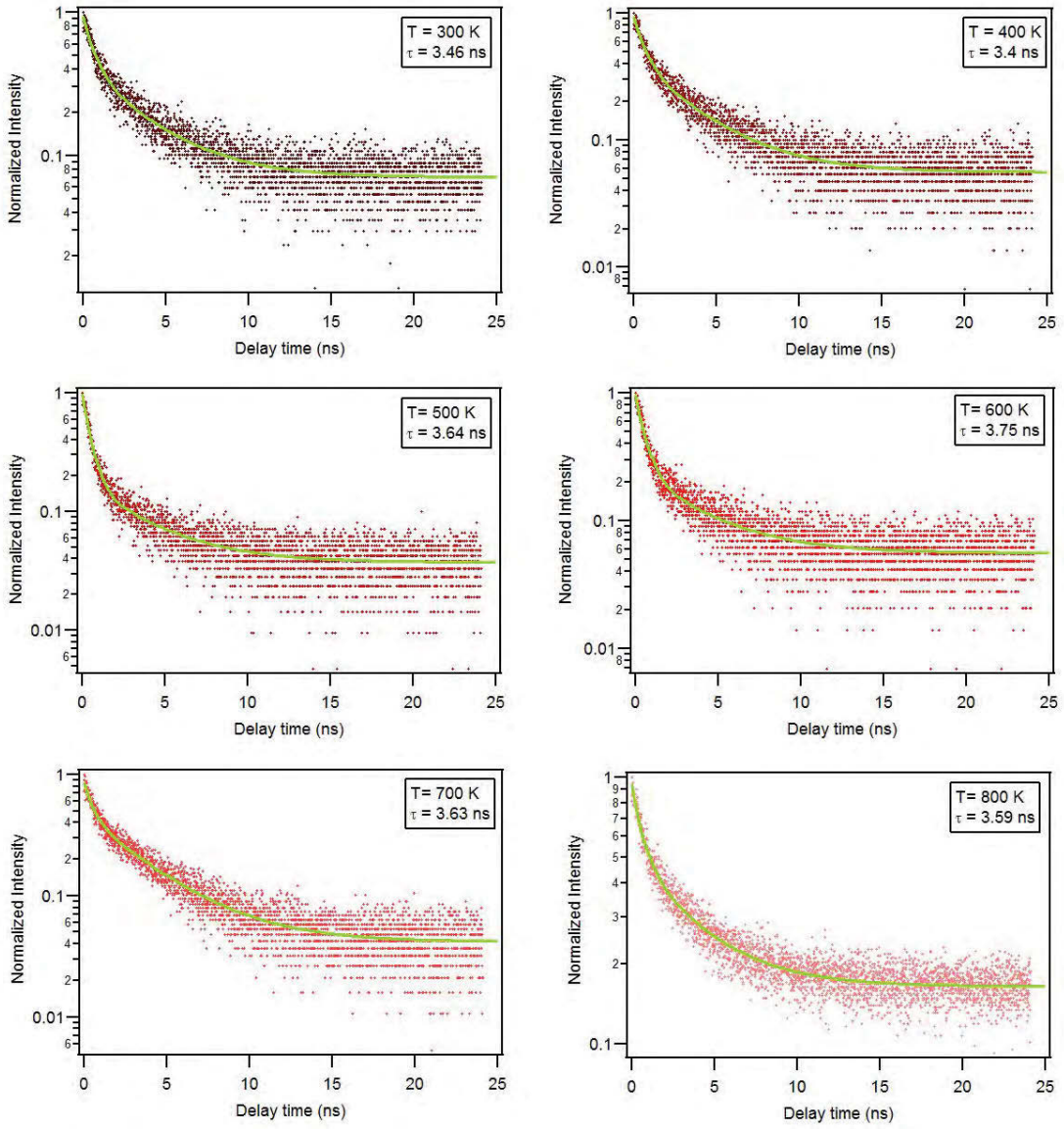

FIGURE 5.8: The lifetime values and temperatures are labeled at each plot. Lifetime values were obtained by fitting with double exponential function while the first exponential term kept fixed at 500 *ps* during fitting. Green curves represent the fit at each temperature.

5.6 Quantum emission at high temperature in air

Although the temperature dependence measurements have been done in vacuum conditions, the SPSs in hBN are also stable at high temperatures even in air. Initially the measurements were conduced in vacuum due to the limitation for operating the

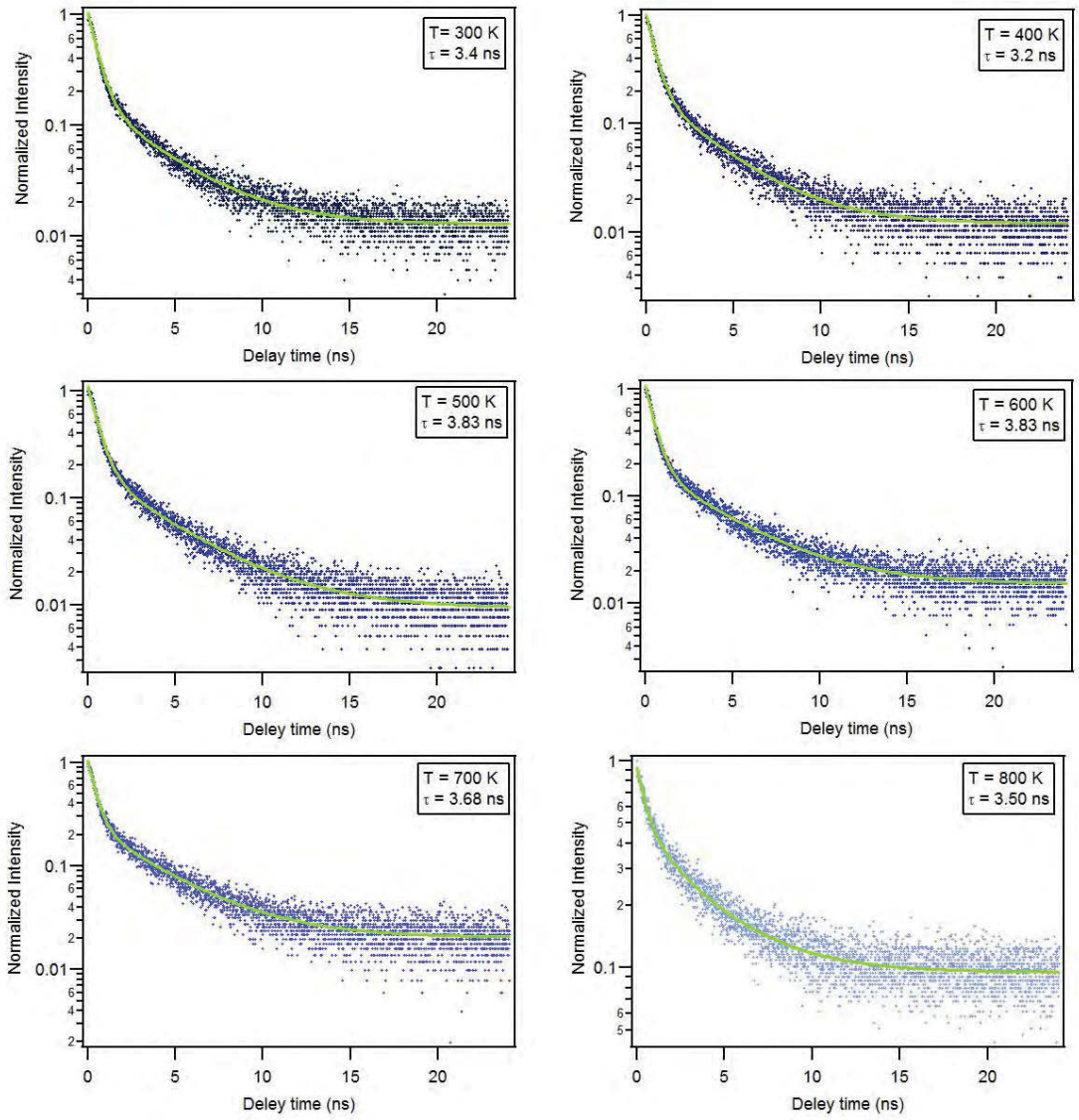

FIGURE 5.9: The lifetime values and temperatures are labeled at each plot. Lifetime values were obtained by fitting with double exponential function while the first exponential term kept fixed at 500 *ps* during fitting. Green curves represent the fit at each temperature.

heater used in the chamber in air or oxidizing environment. A SPS in hBN was subjected to heating in air and photoluminescence of the source was measured from 300 up to 625 K. Figure 5.10 shows high temperature measurement of the SPS in air. Autocorrelation data measured at each temperature was fitted with a 3-level model (figure 5.10(a)). Photoluminescence spectrum showed similar changes as the ones measurement in vacuum conditions. Figure 5.10(c) and (d) summarizes the change

in the $g^2(0)$ values, as well as ZPL energy and FWHM changes in PL spectrum as a function of temperature, respectively. Single photon purity which is $g^2(0)$ values, remained constant at all temperatures (figure 5.10(c)), ZPL red shift and broadened as the temperature increased (figure 5.10(d)). In addition, performing the measurement in vacuum is not considered as a limitation in real applications as the emitters can potentially be protected or encapsulated by a thin and stable material.

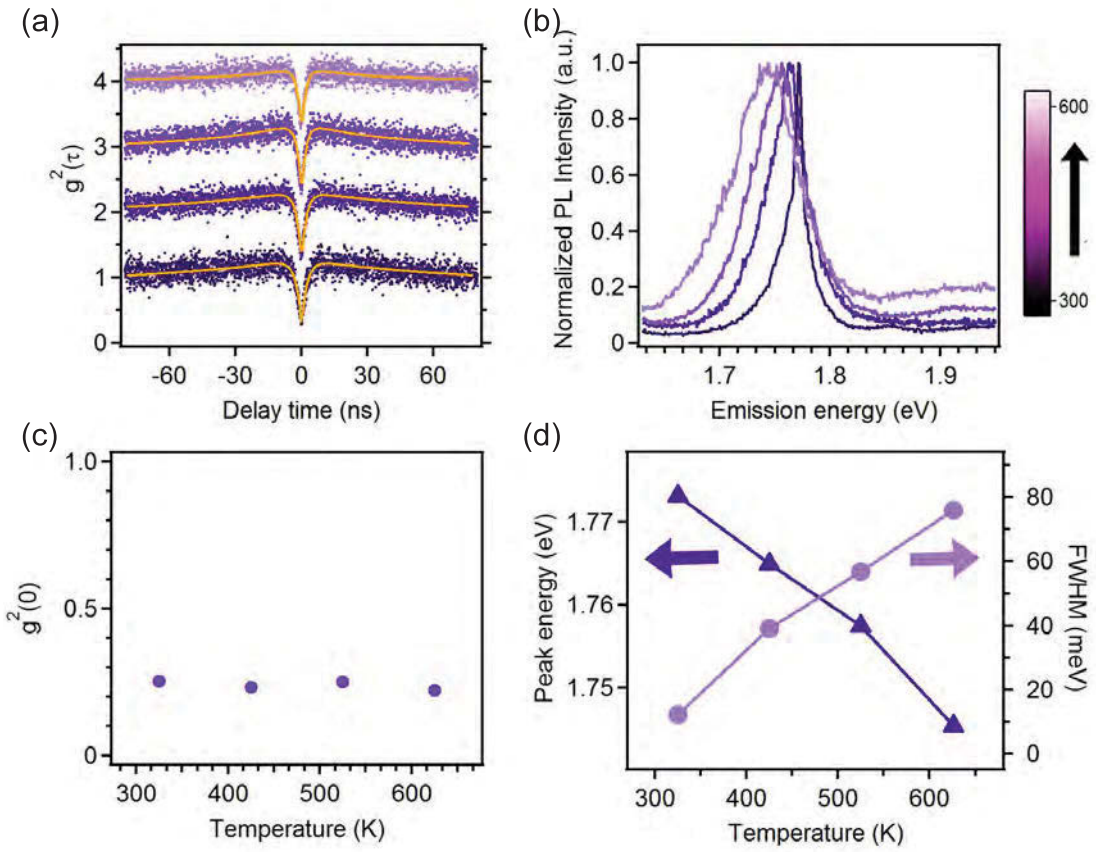

FIGURE 5.10: (a) Autocorrelation curve and (b) normalized PL spectrum measured at 100 K intervals between 300 and 600 K. The autocorrelation data in (a) are offset for clarity and green solid curves are fit obtained using a three-level model. (c) Coincidence counts at zero delay time, $g^2(0)$ as a function of temperature during the heating in air. (d) Zero phonon line (ZPL) position (left) and width (right) plotted as a function of temperature during heating and cooling. Solid lines are guides to the eye.

5.7 Change in the hBN emitters at high temperature

SPSs investigated were completely stable during heating and cooling as discussed earlier in 5.3. However, some of the emitters were find to be unstable during heating. Figure 5.11 shows an example of emitters in hBN which underwent changes during heating. In this particular case, although autocorrelation measurement at room temperature revealed antibunching behavior, the $g^2(\tau = 0)$ value was above 0.5 confirming the presence of more than on emitter in the confocal spot. Increasing the temperature resulted in increase in the $g^2(\tau = 0)$ value and ultimately antibunching behavior vanished at 500 K (figure 5.11(a)). The effect was permanent and remained after cooling back to room temperature as shown with the pink curve in figure 5.11(a). Figure 5.11 confirms the presence of the emitters during the measurement. However the intensity of the peak at 630 nm increased during heating. The intuitive explanation is the diffusion of defects within the confocal spot which brought the emitters closer together and resulted in increase higher contribution of the emitter at 650 nm. Figure 5.11(c) is the change in $g^2(\tau = 0)$ of this emitter during heating. Finally, the effect was permanent and the emission spectrum of the emitter modified after cooling back to room temperature (figure 5.11(d)).

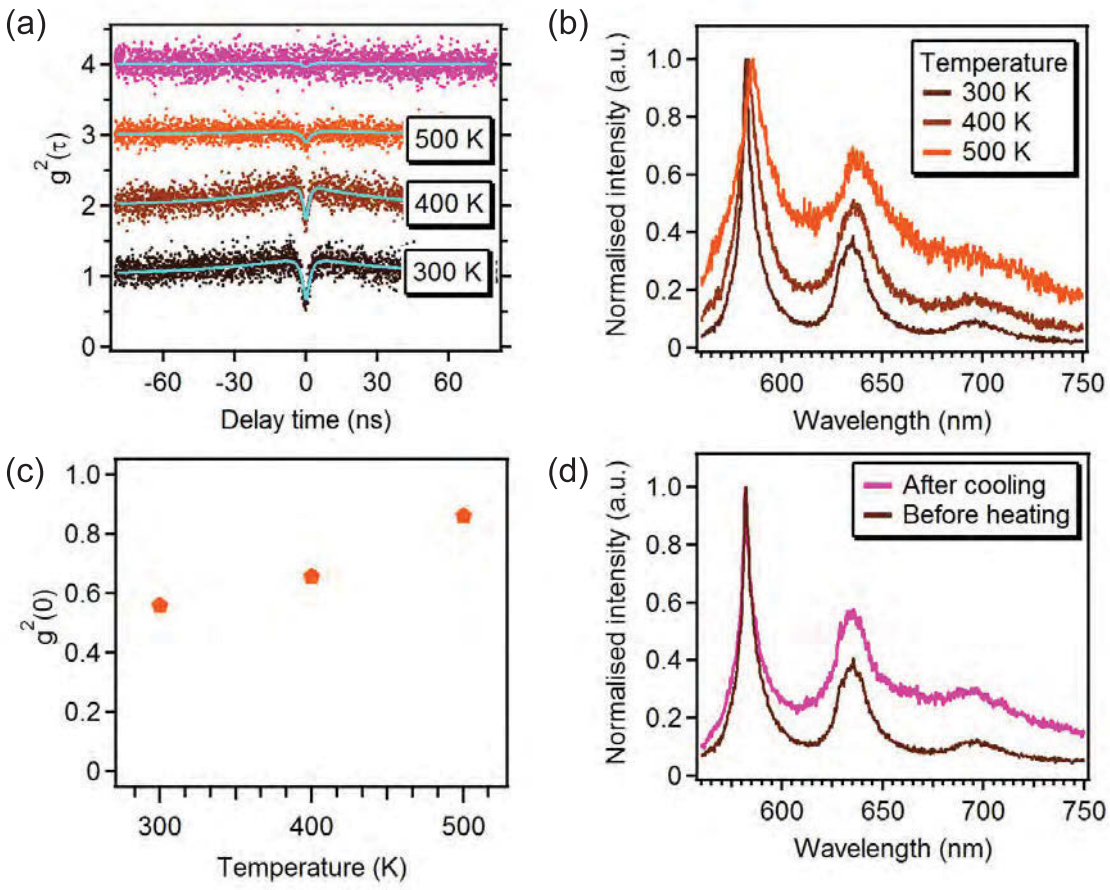

FIGURE 5.11: (a) Autocorrelation curve and (b) normalized PL spectrum measured at 100 K intervals between 300 and 500 K. The autocorrelation data in (a) are offset for clarity and blue solid curves are fit to the data. (c) Coincidence counts at zero delay time, $g^2(0)$ as a function of temperature during the heating. (d) PL spectrum of the same emitter at ambient condition, before heating and after cooling to room temperature.

5.8 Conclusion

In conclusion, our work demonstrates robust SPSs that can operate at elevated temperatures of up to 800 K. The results open up exciting new possibilities to integrate hBN SPSs with large scale, on-chip quantum photonic devices that work under ambient conditions or or elevated temperatures, and localized temperature sensing with high spatial resolution. Our results also provide vital information on stability and photophysical properties of defects in layered materials, stimulating further research in this area.

Chapter 6

Super resolution microscopy with hBN

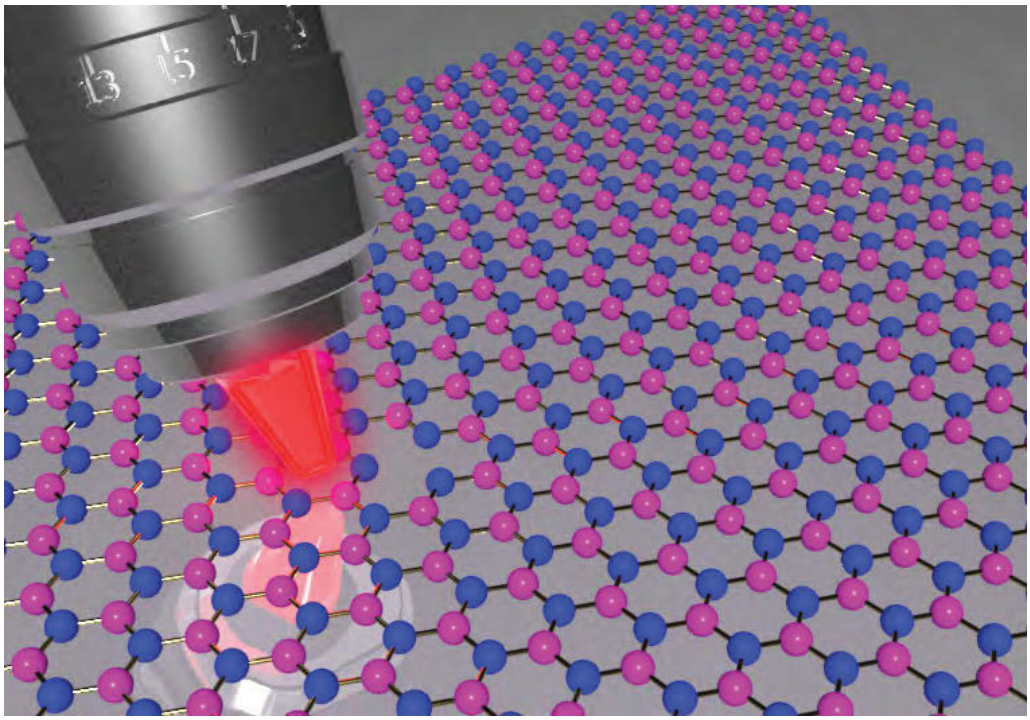

Layered van der Waals materials are emerging as compelling two-dimensional (2D) platforms for studies of nanophotonics, polaritonics, valleytronics and spintronics, and have the potential to transform applications in sensing, imaging and quantum information processing [170][171][172][23].Amongst these, hexagonal boron nitride (hBN) is known to host ultra-bright, room-temperature quantum emitters, whose nature is yet to be fully understood 3. Here, a set of measurements which give new insight into the photophysical properties and level structure of hBN quantum emitters is presented. Specifically, i) we report the existence of a class of hBN SPEs with a fast-decaying intermediate and a long-lived metastable state accessible from the first excited electronic state; ii) by means of a two-laser repumping scheme, highly nonlinear emission of these emitters has been shown which results in enhanced photoluminescence and reduced excitation power needed to saturate the emission intensity by up to approximately one order of magnitude. To demonstrate the utility of the unique photo-physics of these quantum emitters, a new modality of far-field super-resolution imaging has been utilized, which adds to the suite of Reversible Saturable Optical Fluorescence Transitions (RESOLFT) techniques. These findings expand current understanding of the photo-physics of quantum emitters in layered hBN and show new potential ways of harnessing their nonlinear optical properties in sub-diffraction nanoscopy.

6.1 Introduction

The exploration of nanophotonic phenomena in 2D systems using materials such as transition metal dichalcogenides (TMDCs), phosphorene and hexagonal boron nitride (hBN) has gained considerable momentum in recent years [23][24][25][26]. Localized nanoscale effects, including radiative decay of interlayer excitons and emission of anti-bunched photons from deep trap point defects, are particularly interesting and important [22][173][28]. The latter, for instance, is key to the practical deployment of scalable, on-chip quantum photonic devices [157][29]. In this context,

2D-layered hBN has shown great promise owing to its ability to host fully polarized, ultra-bright and narrow-linewidth color centres which act as photostable quantum emitters at and beyond room temperature . Their nature is still under dispute, as is a convincing explanation for the large distribution of observed zero-phonon line (ZPL) energies (ranging from the ultraviolet to the near-infrared) and for the photodynamic properties of the emitters 3. In this work, a series of systematic experiments have been carried out to shed light onto the level structure and photodynamics of quantum emitters in hBN. Room-temperature, off-resonant excitation was performed at different wavelengths, as well as second order autocorrelation and saturation measurements. By employing two-laser excitation, an entire class of hBN emitters were identified which possess unique photo-dynamics, allowing the emitters to be reverted from the intermediate state to the excited state(s) by means of optical repumping. This leads to a strong nonlinear enhancement of photoemission, as well as a reduction of the excitation power that is needed to saturate the emission intensity. This highly nonlinear behavior wa exploited to propose and demonstrate a new scheme for super-resolution imaging.

6.2 Emitter properties

A schematic of the hBN atomic lattice hosting the atomic defect is shown in figure 6.1(a), with blue and pink corresponding to the nitrogen and boron atoms, respectively. The atomic structure of the center is a matter of debate, and a number of vacancy-related defects have been proposed to be the origin of the quantum emission [22][60][61]. First, the emitter was characterized using a conventional confocal, optical microscope and a Hanbury-Brown and Twiss (HBT) interferometer (more details in chapter 3). Figure 6.1(b) shows the room-temperature photoluminescence (PL) spectrum of the emitter when excited with a 675 nm wavelength laser. The emitter has a zero phonon line (ZPL) at 778 nm and a negligible phonon sideband. The inset

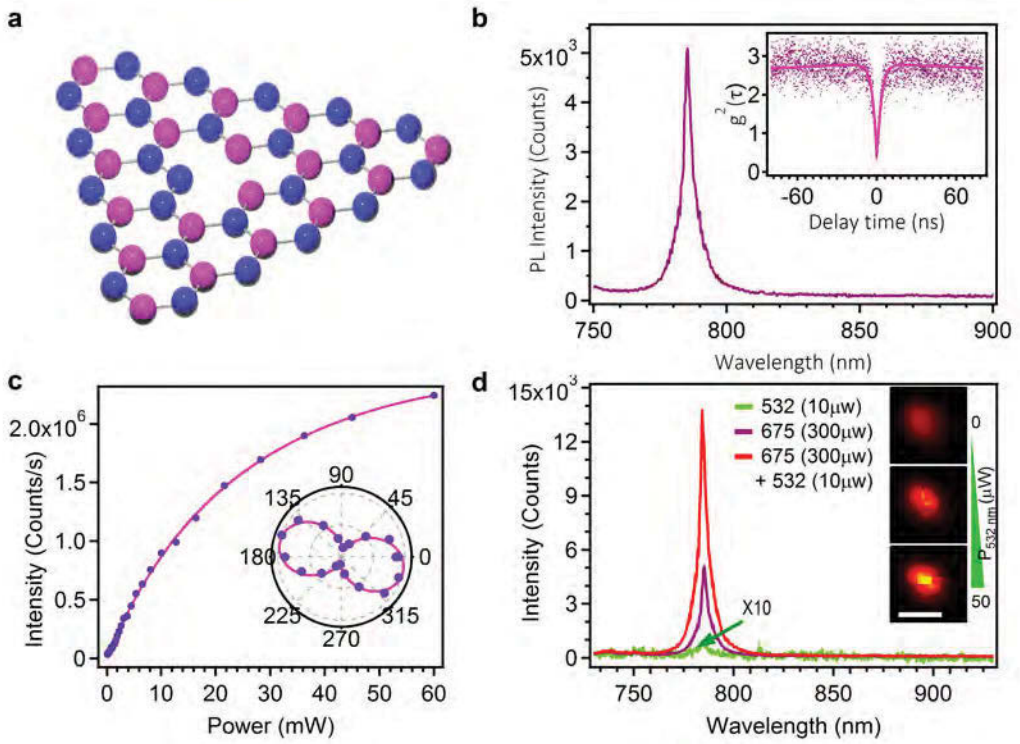

FIGURE 6.1: (a) Two-dimensional hBN hosting a fluorescent defect. (b) Photoluminescence spectrum of the single defect in hBN under 675-nm excitation. Inset: second order autocorrelation measurement ($g^{(2)}(\tau)$) of the defect with a dip at $g^{(2)}(\tau = 0) \simeq 0.25$, indicating single photon emission. c) Saturation curve of the emitter under excitation with a 708-nm laser. The solid line is the fit to $I = (I_\infty \times P)/((P + P_{sat})$, according to which the 50% of the saturated emission occurs at 14 mW. Inset: emission polarization curve of the emitter. The emission dipole is in the plane of the layered host crystal. (Note: the 708-nm laser was used in lieu of the 675-nm one for measurements requiring high power). d) Photoluminescence spectra of the single defect under three excitation conditions: low-power (10 μW) 532-nm laser [green trace], high power 675-nm laser [purple trace] and coincident excitation with both lasers [red trace]. Note that the spectrum under excitation with the 532-nm laser [green trace] has been multiplied tenfold for display purposes. Inset: nonlinear increase of the emitter brightness upon a linear increase in the power of the 532-nm excitation laser coincident with the 675-nm excitation laser. Scale bar is 500 nm.

displays the second order correlation function, $g^{(2)}(\tau)$, which indicates that the emission is predominantly from a single defect: $g^{(2)}(\tau = 0) \simeq 0.25$, well below 0.5 at zero delay time (the correlation data are not background-corrected). Figure 6.1(c) shows the saturation behaviour of the emitter, excited with a 708-nm laser. The data has been fitted to the equation $I = (I_\infty \times P)/((P + P_{sat}))$; accordingly, the 50%

value of the saturated emission intensity occurs at 14 mW. Emission polarization measurements of the emitter (figure 6.1(c), inset) reveal that the emission is fully polarized, as expected from a dipole located in-plane within the layered host crystal.

After confirming the quantum nature of the emitter, a second laser was introduced to look for nonlinearities in the photoluminescence (PL). Figure 6.1(d) displays the emission intensity for the reference emitter upon excitation with: i) a 675-nm laser [purple trace], ii) a 532-nm laser [green trace] and iii) the simultaneous pair of 675-nm + 532-nm lasers [red trace]. The emitter was excited with 10 μW of power for the 532-nm laser and 300 μW for the 675-nm laser. The 532-nm excitation yielded a negligible fluorescence intensity – note that the corresponding PL spectrum in Figure 6.1(d) [green trace] is multiplied tenfold for clarity. Interestingly, comparing the excitation of the emitter with the 675-nm laser [purple trace], and the co-excitation with the laser pair, i.e. 675-nm (300 μW) plus 532-nm (10 μW) [red trace], reveals a highly nonlinear behavior (Figure 6.1(d)). Specifically, upon co-excitation, the emission intensity increases by more than twofold, which is far greater than the 3.3% increase in total excitation power (from 300 μW to 310 μW). This behavior, highlighted in Figure 6.1(d), is attributed to repumping of the emitter by the 532-nm laser which repopulates the excited bright state from the intermediate state (see below). The emitter does not bleach for laser excitation powers as high as 60 mW, used to obtain the saturation curve in Figure 6.1(c). The same nonlinear behavior was observed on other – yet not all – emitters (6.5) with different ZPL energies $< 1.77eV$ (i.e. emission wavelengths $> 700nm$).

6.3 Photophysics of hBN emitter

Figure 6.2(a) shows long-time (up to milliseconds) second order autocorrelation measurements, $g^{(2)}(\tau)$, recorded for the reference quantum emitter introduced in Figure

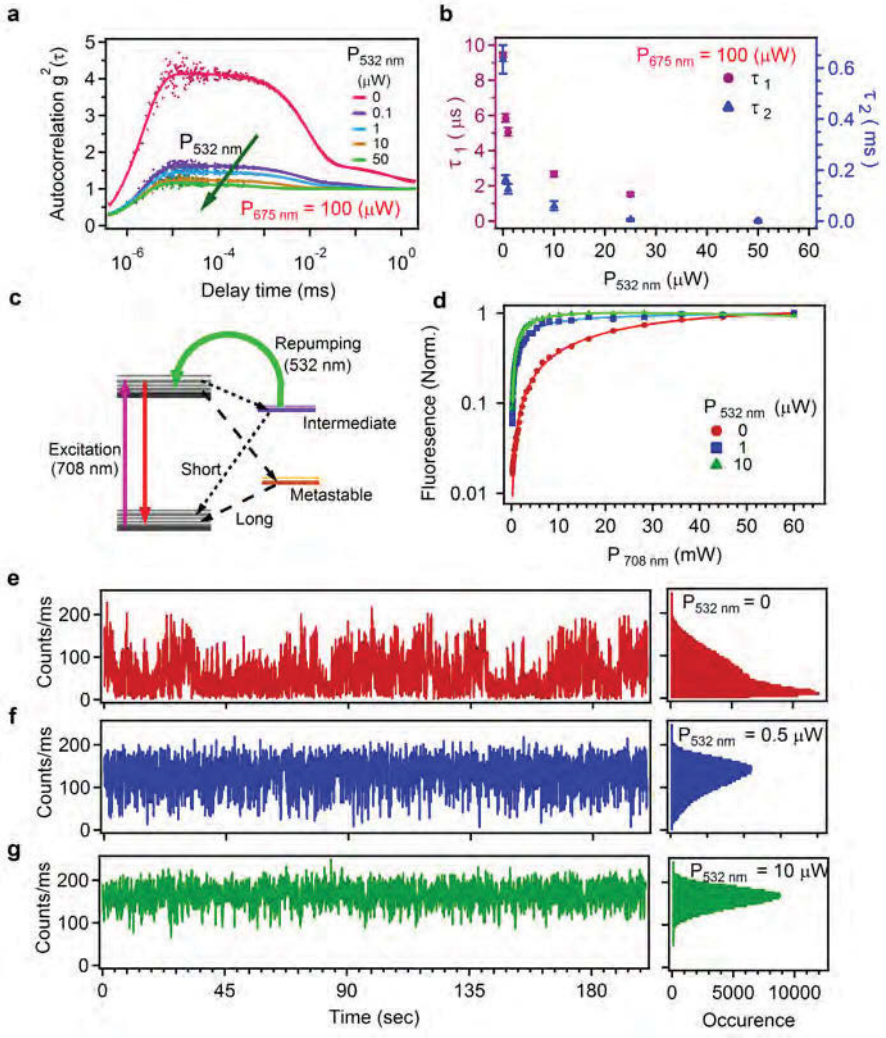

FIGURE 6.2: (a) Long autocorrelation measurements under excitation with a 675-nm laser (100 μW). The experimental data (points) are fitted (solid lines) using a four-level model. (b) Reduction in the time constants τ_1 and τ_2 associated with the intermediate/metastable states (extracted from the fits in (a). (c) Simplified level structure of the emitter (see main text). The emitter possesses a ground state and excited state(s), as well as a fast-decaying intermediate and a long-lived metastable state. Radiative transitions are indicated by straight, solid arrows, repumping via the 532-nm laser is indicated by the green arrow, and fast and slow non-radiative transitions are indicated by dashed arrows. (d) The repumping causes a reduction in the laser power that is needed to saturate the emitter. (e-f) Fluorescence time trajectories of the emitter sampled into 100-ms bins, under excitation with 708-nm (e) or co-excitation with 708-nm and 532-nm lasers (f, g). The power of the 708-nm laser was kept at 100 μW and the power of the 532-nm repumping laser was 0.5 μW and 10 μW in (f) and (g), respectively. The corresponding histogram of the photon distribution at each excitation condition is shown on the right.

6.1. The different datasets are collected under 675-nm laser excitation [pink trace], and upon co-excitation with the 675-nm laser (100 μW) and the 532-nm laser, the power of which was varied [purple, cyan, ochre and green traces] as emphasized in the figure by the green arrow. The dip in $g^{(2)}(\tau)$ at short (ns) time scales confirms that the emitter is a quantum emitter with sub-Poissonian statistics. The exponential decays at longer (ms) time scales reveal the presence of additional intermediate/metastable levels. The best fit to the data is achieved using a four-level model (Figure 6.2(c)), where two of the exponential decays observable in Figure 6.2(a) correspond to states whose photo-dynamics is non-trivial, as discussed below. The time constants (τ_1 and τ_2) for these two intermediate/metastable levels – as obtained from the fit – are plotted in Figure 6.2(b). Interestingly, the two-laser co-excitation measurements show that these states are depopulated by the addition of the 532-nm laser, even at a very low power, $\sim 0.1\mu W$. The relative time constants τ_1 and τ_2 indeed decrease (Figure 6.2(b)) for increasing excitation powers of the 532-nm laser (in the investigated range $\sim$ 0.1–50μW). This decrease is nonlinear, and it correlates consistently with the enhancement in photoluminescence intensity observed in Figure 6.1(d). Simultaneously – and remarkably – the addition of the 532-nm laser affects the saturation behavior of the emitter. Specifically, repumping via the 532-nm laser reduces the intensity required to saturate the emitter. This is highlighted in Figure 6.2(d) where the saturation curve upon sole 708-nm laser excitation [purple trace] is compared to two curves obtained upon co-excitation with the 708-nm and the 532-nm laser pair, with 532-nm laser powers being 1 and 10 μW [blue and green traces]. In brief, under 708-nm excitation the emitter saturates at $\sim$ 14 mW. Under co-excitation, the emitter saturates at $\sim$ 3 mW ($P_{532nm} = 1\mu W$) and $\sim$ 1.5 mW ($P_{532nm} = 10\mu W$), respectively – that is, the use of the laser pair reduces the saturation power by approximately one order of magnitude. The saturation under sole excitation with 532 nm laser would increase due to the lower cross section for this wavelength. Additionally, the emitter shows a peculiar fluorescence indeterminacy ('blinking') behaviour which is dependent, as well, on the 532-nm excitation. Figure 6.2(e)-(g) summarizes the main characteristics. Under excitation

with the sole 708-nm laser, the emitter exhibits two fluorescent thresholds (Figure 6.2(e), left) with the statistics for the photon distribution (Figure 6.2(e), right) showing the system to be mainly in the lower fluorescence one. Note that there appears not to be an off-threshold – which would correspond to a completely dark state with the number of detected photon counts equal to the background level. By adding the 532-nm laser of increasing power, the statistic of the photon distribution shifts towards the threshold of higher fluorescence (Figure 6.2(f) and (g)).

A possible model consistent with all our observation is presented in Figure 6.2(c). The long autocorrelation measurements show that the emitter essentially behaves like a four-level system with a fast-decaying intermediate and a long-lived metastable state (see below). Off-resonant excitation with either a 532-nm or a 675-nm (or 708-nm) laser leads to emission into the ZPL, with relative intensities in excellent agreement with recent reports [67]. Addition of the 532-nm to the 675-nm excitation laser suppresses the population of the intermediate state via repumping to the excited state(s), which results in the observed enhanced, nonlinear photoemission. This repumping effect is non-trivial: the nonlinear increase in photoluminescence is accompanied by a reduction in the intensity required to saturate the emitter (Figure 6.2(d)), which indicates the existence of a complex dynamics involving both the intermediate and the metastable states. My interpretation is that upon sole 675-nm (or 708-nm) excitation the system can undergo a transition to a dark state through the long-lived metastable state, with this dark state possibly being a different charge state of the emitter. This is consistent with the blinking data in Figure 6.2(e), where we see the emitter's photo-statistics being mainly at the low-fluorescence threshold upon sole 675-nm excitation. As a caveat, I deliberately use the word 'threshold' rather than 'state', as the binning average is oblivious to transitions of fast-dynamics – which is potentially the case in the hypothesis of transitions to a different charge state. Note that this is also consistent with the fact that we do not measure a non-fluorescent off-state in the blinking trace, indicating that we are indeed averaging over very fast-dynamics transitions. It also allows us to weaken the possibility that these transitions occur towards trap states with slow dynamics (as these would be

detected as a complete off-state in the fluorescence time trajectory). The blinking analysis also shows (Figure 6.2(f) and (g)) that the addition of the 532-nm repumping laser suppresses the probability for the emitter to be in the low-fluorescence threshold and allows us to infer about the relative dynamics between the fast-decaying intermediate and long-lived metastable state. Specifically, the repumping via the 532-nm laser reverts the system from the intermediate state to the excited state(s), thus inhibiting the otherwise faster non-radiative decay from the intermediate to the ground state – which would occur without repumping. This efficiently depopulates the ground state resulting in the observed reduction in excitation intensity required to saturate the emitter.

A detailed modeling and analysis of the photo-kinetics of the center and its dependence on the 532-nm laser repumping is presented in the Methods section of this chapter. As mentioned before, the same behaviour could be reproduced on an entire subclass of emitters with emission ZPLs $> 700nm$ (6.5).

6.4 Super-resolution imaging of the centers in hBN

As a demonstrative application, we show that the unique photo-physical properties of this class of hBN quantum emitters can be harnessed to realize a new modality of far-field, sub-diffraction fluorescence nanoscopy. Super-resolution nanoscopy methods grouped under the umbrella of Reversible Saturable Optical Fluorescence Transitions (RESOLFT) techniques rely on two key criteria: (1) the existence of controllable bright/dark-like transitions between the emitter's states, and (2) resilience of the emitters (and the enclosing environment) against high-power excitation, since the transition to the dark state is typically achieved via optical saturation. For instance, stimulated emission depletion (STED)[74] and ground state depletion (GSD)[75] methods exploit spatially-modulated (e.g. doughnut-shaped) light beams with ultrasharp bright/dark gradients to selectively image emitters. In STED techniques, this is achieved by 'switching off' the emitters around the doughnut null

(where the emitter to be imaged is located) by inducing stimulated emission (at saturation) between the first optically excited (S_1) and the ground (S_0) states. In GSD, the same outcome is achieved by shelving the system to a metastable, long-lived dark-state (T_1, usually accessible from S_1).

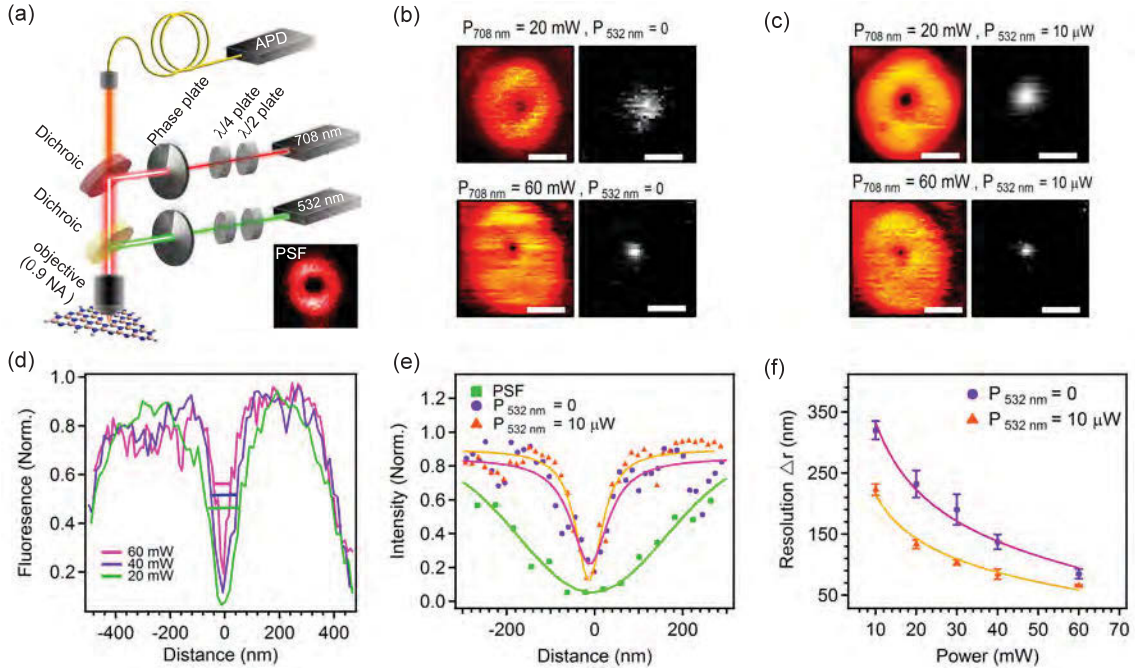

FIGURE 6.3: (a) Schematic of the setup used to perform GSD nanoscopy employing excitation lasers with doughnut-shaped intensity profiles. The system point spread function was determined by reflection of the lasers from a 50 nm gold nanosphere (inset, red circle). (b) Negative GSD images of the single defect under excitation with a single 708 nm, doughnut-shaped laser, and using laser powers of 20 mW and 60 mW as indicated. The direct GSD images on the right are obtained by linear deconvolution of the negative GSD images on the left. (c) Negative GSD images of the same emitter after addition of a 10 μW, 532 nm, doughnut-shaped re-pumping laser co-aligned with the 708 nm laser. The images on the right are linear deconvolutions of the negative ones. d) Photoluminescence intensity profiles of negative GSD in (b) showing a resolution improvement at higher excitation powers. Solid lines indicate the full width at half maximum (i.e. the resolution) of the emission null at the center of the doughnut. (e) Intensity profiles used to compare the resolution obtained from negative GSD performed at 40 mW of 708 nm laser using the single doughnut beam (circles, violet) and the co-incident laser pair (triangles, orange). For comparison, the intensity profile obtained from reflection of 50 nm gold nanoparticles (squares, green) is shown as point spread function of our setup. (f) Dependence of GSD resolution on the power of the 708 nm laser, with and without the co-incident 532 nm, 10 μW repumping laser. Scale bars in (b) and (c) are 300 nm

The class of hBN emitters presented in this work satisfy both criteria (1) and (2). I therefore used them to realize GSD imaging using the experimental setup shown in Figure 6.3(a). Briefly, a 532-nm and a 708-nm laser are co-aligned and simultaneously focused through an aberration-corrected objective (numerical aperture, NA = 0.95). The photons from the emitters under investigation are back-collected with the same objective, focused into the aperture of an optical fiber (used as a confocal-microscope pinhole) and directed to an avalanche photodetector. Depending on the excitation scheme (see below), I employed vortex phase masks to modulate both the 532-nm and the 708-nm excitation laser into having a spatial doughnut-shaped profile, with a near-zero intensity in the center (Figure 6.3(a) inset). I start by performing standard negative GSD nanoscopy using the 708-nm doughnut-shaped laser as the excitation source (Figure 6.3(b)). Negative GSD[90] is possible with this class of hBN emitters as photo-kinetics analysis revealed they possess at least one long-lived metastable dark-state (Criterion 1) and they are photostable at high excitation powers (Criterion 2). As the beam is scanned, the emitter experiences a doughnut-shaped excitation intensity profile which produces a corresponding 'high-null-high' emission pattern. With this configuration, in the confocal image the emitter's location coincides with the center of the emission null. Sub-diffraction resolution is achieved as at higher powers of the scanning doughnut beam the 'high-null' and 'null-high' PL emission gradients become steeper, which effectively narrows the full width at half maximum (FWHM) of the emission null. The minimum in intensity yields an inverse image of the emitter with a spatial resolution that exceeds the diffraction limit. The mathematical deconvolution[91] of the negative GSD image (Figure 6.3(b), left) yields a direct GSD image of the emitter (Figure 6.3(b), right). Figure 6.3(d) shows the GSD resolution (extracted from the FWHM of the null) that we can obtain by varying the power of the 708-nm doughnut-shaped laser. With the experimental parameters of our setup (NA = 0.95, $\lambda_{EXC} = 708nm$), we reach a resolution of (87 ± 10) nm at 60 mW – well below $\sim 460nm$, which is the diffraction-limited resolution measured for our confocal setup. The resolution Δr is given by[90]:

$$\Delta r \cong \lambda(\beta\pi n)^{-}1\sqrt{\epsilon + \frac{I_s}{I_m}} \tag{6.1}$$

where I_m is the maximum laser intensity in the crest of the doughnut, while ϵI_m is the minimum ('null') intensity in the center. The quantity n is the refractive index of the medium, and I_S is the laser intensity at which the emission intensity equals half of the maximum value in the limit of infinite excitation power. The parameter β is the 'steepness' of the point spread function (PSF) and depends both on the emitter properties and the 'crest-to-minimum' intensity gradient of the doughnut-shaped excitation source. For this purposes, it is hereby relevant to point out that GSD resolution is, in principle, non-diffraction-limited: it improves by increasing the excitation laser power beyond I_s, so as to minimize the ratio I_s/I_m. This usually translates in the need to use high laser powers to achieve high spatial resolution, which is the main drawback of GSD methods and the related suite of RESOLFT imaging techniques [91]. The high excitation powers needed to break the diffraction limit usually result in bleaching of most emitters, and thus restrict the robust use of RESOLFT methods to a limited number of systems such as the highly photostable color centres in diamond [81]. High excitation powers are undesirable for another reason: they induce heating and can damage the surrounding environment, which is particularly problematic for bio-imaging nanoscopy applications.

Remarkably, these problems are alleviated by the unique photophysics of the class of hBN emitters presented here. With reference to Equation 6.1, if I_s is reduced, the resulting decrease in the ratio I_s/I_m leads to an improvement of the GSD image resolution whilst maintaining a fixed laser power (i.e., a fixed value of I_m in Equation 6.1). The ability to reduce I_s in our system is evident from the PL saturation curves shown in Figure 6.2(c): the co-excitation of the emitter with a 708-nm laser plus a low-power 532-nm repumping laser causes I_S to decrease. Based on this observation, we thus expect the GSD resolution to improve if the imaging is performed using a coincident pair of excitation lasers. To verify this, we perform GSD with a low-power ($10\mu W$), doughnut-shaped 532-nm repumping laser co-aligned with the

708-nm main doughnut beam. The addition of the repumping beam indeed produces higher resolution images of the emitter, as shown in Figure 6.3(c), right (the corresponding direct images were again obtained via linear deconvolution: Figure. 6.3(c), left). The improvement is detailed in Figure 6.3(e) which compares the normalized intensity profile of the emitter excited by a 40 mW, 708-nm beam before [violet circles] and after [orange triangles] applying the $10 - \mu W$, repumping 532-nm laser, as well as the point spread function (PSF) of our conventional confocal setup [green squares], obtained from the reflection image of a 50-nm gold nanoparticle.

A plot of GSD image resolution versus power – up to the maximum power achievable with our experimental setup – is shown in Figure 6.3(f) for both the single (708-nm doughnut) excitation laser and the laser pair (708-nm doughnut + 532-nm doughnut) . The highest resolutions we achieve using the one and the two-laser excitation schemes are (87 ± 10) nm and (63 ± 4) nm, respectively. Noticeably, the power of the 708-nm laser needed to achieve a given target resolution is improved dramatically by the addition of the low power ($10\mu W$) 532-nm repumping laser. For reference, a resolution of 100 nm is achieved with 55 mW of excitation power when using the single doughnut versus the 30 mW ($+10$ μW of the 532-nm laser) of the laser pair. This reduction in laser power is highly desirable for super-resolution nanoscopy as it mitigates the power-induced heating and damage of the sample. Interestingly, there is no intrinsic limitation to extending this repumping scheme to other quantum emitters, provided they possess analogous nonlinear photo-kinetics. This could potentially spur the advancement of novel, alternative schemes for super-resolution imaging.

It is noted that current implementations of GSD imaging based on dual-beam schemes employ a coincident pair of a doughnut plus a Gaussian-shaped laser [90][92]. This configuration is inappropriate here: the low-power 532-nm laser is used to reduce I_S and this effect must be maximized in the crest of the doughnut-shaped, high power 708-nm beam, whilst maintaining an intensity null at the beam axis (i.e. in the center of the doughnut).

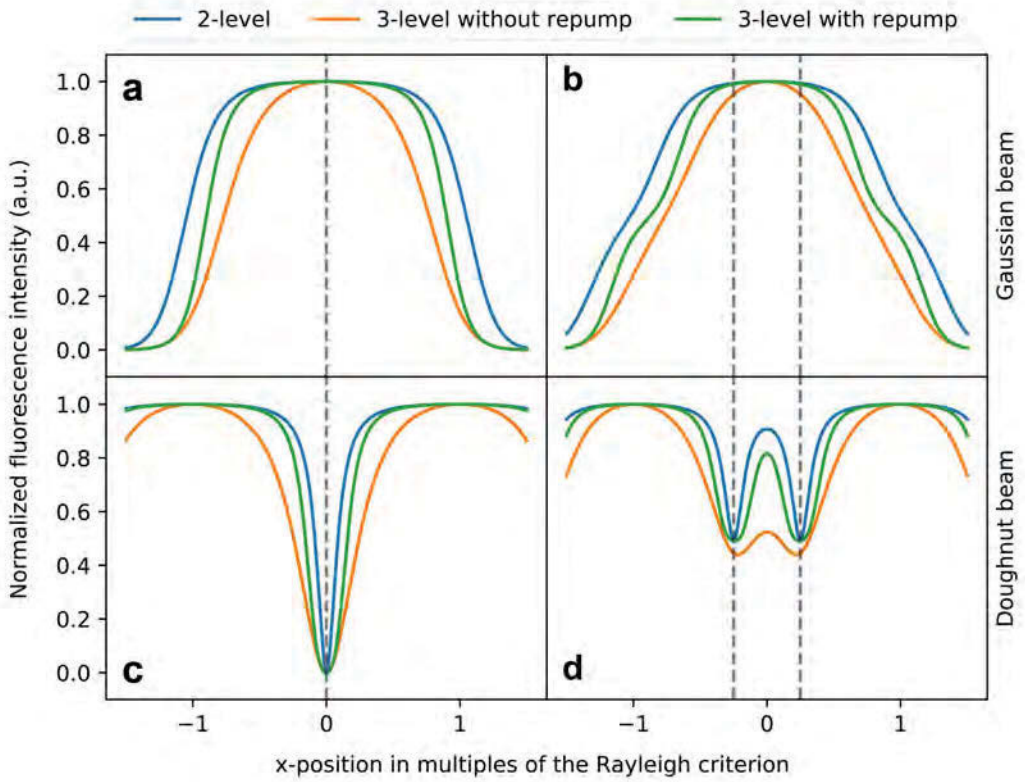

FIGURE 6.4: (a, b) Cross-section profile of a single emitter (a) and two closely-positioned emitters (b) excited with a Gaussian beam. (c, d) Cross section profile of a single emitter (c) and two closely-positioned emitters (d) excited with a doughnut beam. The blue (orange) lines correspond to emitters treated as two- (three-) level systems. The green line refers to the case where a second repumping laser is added – with Gaussian (a, b) and doughnut (c, d) profile, respectively. In (a–d) the x-axis represents the Rayleigh criterion, so that the distance between max and min of the doughnut is 1. The vertical dashed lines indicate the position of the emitter along the x-axis.

To further understand/enhance the effects of repumping on the obtained super-resolution images, the fluorescence profiles of the emitter for different beam shape configurations was calculated (Figure 6.4). For completeness, both the case of a single and that of two closely-positioned emitters are considered. The graph displays the calculated fluorescence of the quantum emitters considered as two-level systems [blue trace], and three-level systems with [green trace] and without [orange trace] the additional laser repumping. Figures 6.4(a) and (b) show that the excitation of the emitters with two superimposed Gaussian beams of different wavelength, does

not achieve resolutions beyond the diffraction limit. Conversely, when doughnut-shaped beams are employed, super-resolution can be obtained via negative GSD. Figure 6.4(c) and (d) show that the co-excitation of the emitters with two doughnut shaped beams (one employed for repumping purposes, as described above) results indeed in improved resolutions. These calculations match well with the experimental results recorded for the quantum emitter in this study (Figure 6.3(d)–(f)).
Interestingly, this calculation indicates that super-resolution imaging with a two-level system is also possible. However, this requires operating at saturation which, in practice, is only feasible under resonant excitation at cryogenic temperatures [174]. On the other hand, it has been shown that exploiting the level scheme and introducing a repumping laser, allow for super-resolution imaging at significantly lower laser excitation powers, at room temperature.

6.5 Emitters with nonlinear behavior in hBN

In this work I surveyed several hBN emitters. The nonlinear behavior presented in the thesis was observed in a number of cases, including both single emitters (Figure 6.5) and ensembles (Figure 6.6). Only emitters with a zero phonon line (ZPL) above 700 nm were investigated (due to experimental constraints). Figure 6.5(a) shows a typical confocal scan of the sample. The autocorrelation measurements from emitters (1) [violet] and (2) [orange] are shown in Figure 6.5(b). At zero delay time, $g^{(2)}(\tau = 0) = 0.21$ and 0.42 for (1) and (2), respectively, indicating that the emission is from single defects (the datasets in Figure 6.5(b) are not background-corrected). Both emitters showed the nonlinear behavior presented in the manuscript under co-excitation with a 675-nm (or 708-nm) and a 532-nm laser, as shown in Figures 6.5(c) and (d) (analogous to Figure 6.1(d). In both spectra, the emission intensity under co-excitation with the 532-nm and the 675-nm laser [red trace] is (nonlinearly) higher than the emission intensity obtained via independent excitation with the 675-nm [violet trace] or the 532-nm [green trace] lasers. The same nonlinear behavior

was also observed for other emitters which did not show photon antibunching in the autocorrelation measurements, $g^{(2)}(\tau = 0)$, hence referring to ensembles. Figure 6.6 shows the PL spectrum of four different emitters in hBN under various excitation conditions. Note that while the autocorrelation measurements for single emitters support the hypothesis of the repumping mechanism discussed earlier (which leads to the observed nonlinear behavior), the same claim could not – in principle – be made in the case of ensembles where other effects might be at play (e.g. difference in absorption cross sections of the emitters).

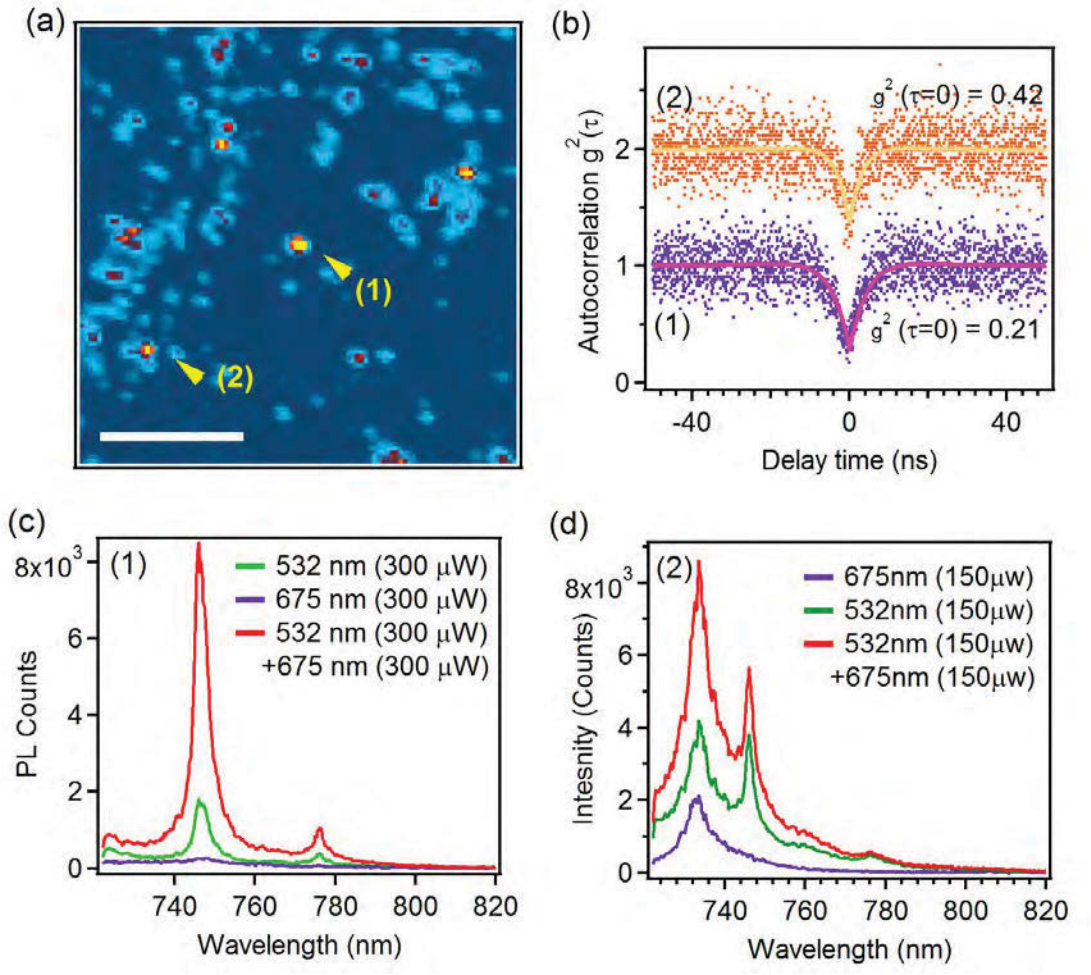

FIGURE 6.5: (a) confocal scan of $30 \times 30\mu m^2$ area of the sample revealing two quantum emitters. Scale bar is 10 μm. b) Autocorrelation measurements from emitter (1) and (2) (marked in the confocal map)with values of $g^2(\tau = 0)$ of 0.21 and 0.42, respectively. Data is not background corrected. (c) and (d) PL spectrum of emitter (1) and (2) under various power- and wavelength-dependent excitation highlighting the nonlinear behavior of the emitters (see main text).

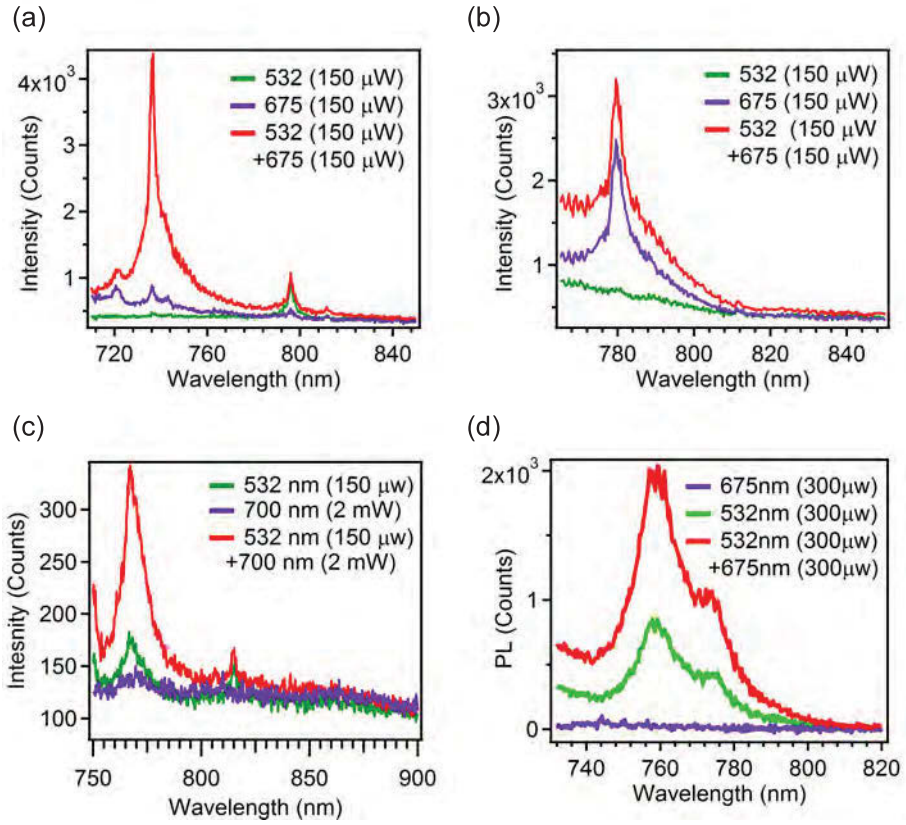

FIGURE 6.6: (a–d) PL spectrum of four different emitters in hBN under various excitation conditions. Note that the emission is recorded from ensembles.

6.6 Intermediate/Metastable states

The best fit to autocorrelation data in figure 6.2(a) was achieved using a four level structure as discussed earlier. The bunching time (τ_{exc}) correspond to excited state lifetime extracted from the fit is shown in figure 6.7.

To determine the relative dependence of the metastable states time constant (τ_1 and τ_2) on the excitation wavelength, two additional experiments were performed. First, the second-order autocorrelation function was measured using excitation from a single laser at a fixed value of power (300 μW), and with wavelength ranging from 675 nm to 740 nm (figure 6.8). Data was fitted considering a four-level structure consisting of two metastable states; the value for (τ_1 and τ_2) of the metastable

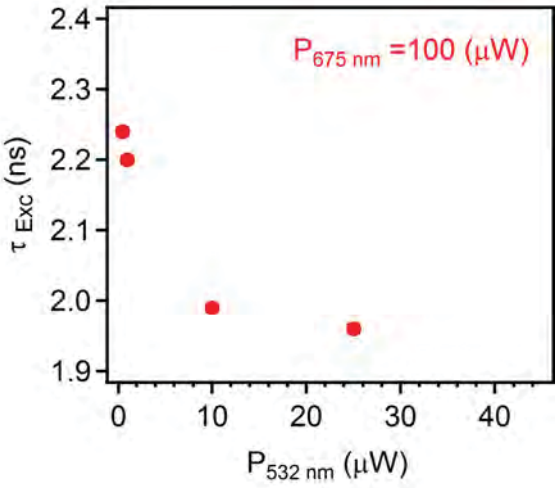

FIGURE 6.7: Bunching time values extracted from the fitting to autocorrelation data in figure 6.2(a).

states were extracted accordingly. Notably, for excitations at 710 nm and below, the population of the metastable states is relatively high.

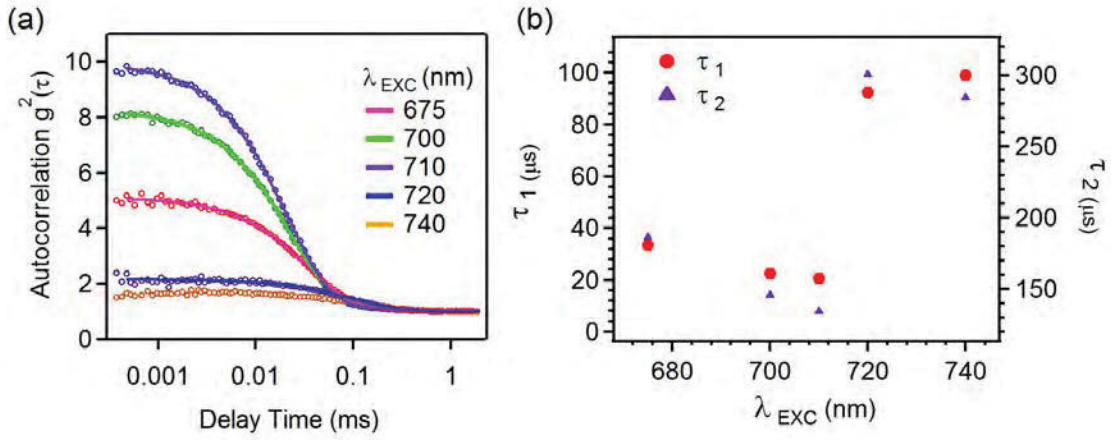

FIGURE 6.8: (a) Autocorrelation measurement on long delay times, up to 1 ms, under various excitations from 675 to 740 nm. Solid lines are the fit with the four-level model. (b) Values of (τ_1 and τ_2) extracted from the fit to data in (a).

Next, autocorrelation measurements were performed by varying the wavelength of the repumping laser, while continuous excitation with the 675 nm laser was maintained (figure 6.9). For all measurements the power of the 675 nm laser was 100 μW and the power of the repumping laser was kept as 10 μW. Under these conditions, the transition rate to the metastable state increased as the wavelength of the

repumping laser increased. The data, again, fits well with a four-level system. This bahvior of the emitter in hBN can be intuitively explained considering a four-level model with two metastable states.

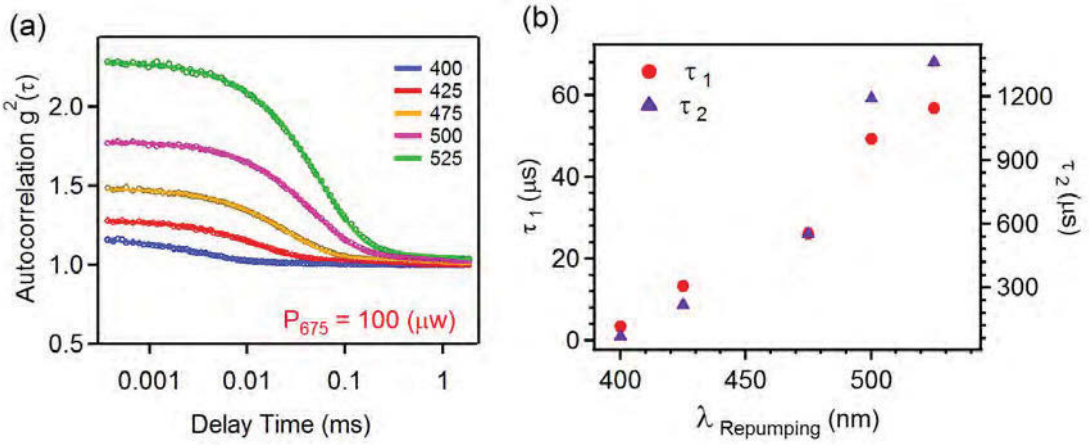

FIGURE 6.9: (a) Autocorrelation measurement on long delay times, up to 1 ms, under various repumping laser wavelengths, from 400 to 532 nm. The emitter was excited with 100 μW of the 675 nm laser in all measurements. Solid lines are the fit with a four-level model. (b) Change in (τ_1 and τ_2) extracted from the fit to the data in (a).

6.7 Methods

Photoluminescence (PL) measurements were carried out in a home-built confocal setup. The sample was mounted onto a XYZ piezo stage (Physik Instrumente-Nanocube P-611) with positioning resolution of 0.2 nm. Optical excitation was performed using different laser sources:

- 675-nm laser (PiL051XTM, Advanced Laser Diode Systems GmbH) – used for PL and autocorrelation measurements.
- 532-nm laser (Shanghi dreamlasers, 532nm low noise CW laser) – used as repumping laser for PL, autocorrelation and saturation measurements.

- Ti:Saph (M-squared, 700-750 nm) – used for saturation measurements, studying the effect of excitation wavelength and super-resolution imaging.
- Supercontinuum (NKT photonics, Fianium WhiteLase supercontinuum laser) equipped with Acousto-optic Tunable Filter (AOTF, 400-550 nm) – used for studying the effect of repumping.

The power of the lasers was measured in front of the objective. To make a doughnut-shaped beam, the laser was first linearly polarized via a polarizing beam splitter (Thorlabs AR coated Cube beam splitter) and then passed through a zero-order half, and a quarter phase plate (Thorlabs-Zero order waveplates) to achieve circular polarization. The beam was then directed through a vortex phase mask (RPCphotonics, VPP-1b for 708 nm and VPP-1c for 532 nm laser). The 708-nm and 532-nm lasers were guided to the sample using a long-pass filter (Semrock 785-nm EdgeBasic) and a dichroic mirror (Semrock 532 nm dichroic), respectively, and were focused on the sample through an aberration-corrected objective lens (Nikon 100X, NA = 0.95). The emission collected from the same objective was filtered using a notch filter (Semrock, 785-nm StopLin notch filter) and a 780-nm long-pass filter (Thorlabs, long-pass color filter) and then coupled to the fiber which was connected to a spectrometer (Acton Spectra ProTM, Princeton Instrument Inc.) equipped with a 300 lines/mm grating and a charge-coupled device (CCD) detector with a resolution of 0.14 nm, or splitted into 50:50 in a Hanbury Brown and Twiss (HBT) interferometer for autocorrelation measurement using two avalanche photon detectors (SPCM-AQRH-14-FC, Excelitas Technologies TM) and a time correlated counting module (Picoharp300TM, PicoQuantTM).

To retrieve the direct image from the negative GSD scan, linear deconvolution was applied using built-in functions in Matlab. First, the high-resolution details (mainly the center local minimum in the negative GSD image) was removed using a short-pass Gaussian filter to produce a blurred image. Then the direct image was extracted

by subtracting the GSD image from the blurred image. The blurred image from the application of the short-pass Gaussian filter (mathematical) method is preferred over the normal confocal scan of the image because of possible mismatch between confocal image and GSD image due to drifting during data acquisition. It is otherwise still possible to use the confocal map instead of the mathematical method [91].

Modeling of the fluorescence intensity profile was done based on a set of rate equations that describe the time evolution of a quantum emitter electronic state, with the four-level scheme shown in figure 6.2(c). It consists of a ground state S, an excited state e, a fast decaying intermediate state i and a long-lived metastable state m, which are connected via rates k_{ij}, with i and j being the levels to which the rates refer.

$$\begin{aligned}
\dot{n}_g(t) &= -k_{ge}n_g(t) + k_{eg}n_e(t) + k_{ig}n_i(t) + k_{mg}n_m(t) \\
\dot{n}_e(t) &= k_{ge}n_g(t) - (k_{eg} + k_{ei})n_e(t) + k_{ie}n_i(t) \\
\dot{n}_i(t) &= n_e(t) - (k_{ig} + k_{ei} + k_{im})n_i(t) \\
\dot{n}_m(t) &= k_{im}n_i(t) - k_{mg}n_m(t)
\end{aligned} \tag{6.2}$$

Here, n_i is the time dependent population of each state. A repump mechanism from the intermediate to the excited state is motivated by the measurements shown in figure 6.2 and reflected in the model via the transition rate k_{ie}. This repump rate is assumed (see below) to be proportional to the 532-nm laser intensity, while the rate excitation rate k_{ge} is assumed to be proportional to the 708-nm laser. Under continuous wave illumination the system reaches the steady state ($\dot{n}_g(t) = \dot{n}_e(t) = \dot{n}_i(t) = \dot{n}_m(t) = 0$), and the set of rate equation 6.2 can be solved. This gives the following average probability of the system to be in the excited state under continuous excitation:

$$< n_e >= \frac{k_{ge}k_{ig}(k_{me} + k_{mg} + k_{mi})}{k_{em}k_{mi}(k_{ge} + k_{ig}) + k_{ig}(k_{em}(k_{ge} + k_{mg}) + (k_{eg} + k_{ge})(k_{me}k_{mg}k_{mi}))} \quad (6.3)$$

Multiplying Equation 6.3 by the radiative decay rate k_{eg} provides a direct relation between the contributing rates and the maximum detectable fluorescence intensity. Based on the measurements shown in figure 6.2, it is justifiable to assume that the transition from the first excited optical state to the intermediate state and the subsequent relaxation towards the ground state are on a much shorter time scale than the radiative transition from the excited to the ground state. However, the intermediate state also provides a decay channel to a long-lived metastable state (possibly a different charge state of the emitter). Scanning an excitation or repump beam across a fixed emitter changes the corresponding transition rate proportionally to the local beam intensity. While keeping the rates of all relaxation channels constant ($k_{eg} = 1, k_{ei} = 10, k_{ig} = 100, k_{im} = 0.1, k_{mg} = 1$), we can qualitatively model the expected fluorescence intensity profile for the different scanning beam shapes and excitation/repump schemes presented in figure 6.4. Analogously to [74], we construct the doughnut beam intensity profile from two Airy functions, spaced apart so that their first minima perfectly overlap. In figure 6.4 the distance between one maximum and the center of the doughnut represents the Rayleigh criterion and is the scale of the x-axis. The Gaussian beam root mean square spot size was chosen to be 0.42: this is the length to approximate the shape of a single Airy profile. The intensities were scaled such that the maximum repump rate was$k_{(ie.max)} = 1000$, indicating a highly efficient repump mechanism, and the maximum excitation rate was $k_{(ge,max)} = 100$, in order to reach saturation at the beam profile maxima.

6.8 conclusion

To conclude, the existence of a class of hBN quantum emitters with a highly nonlinear optical behavior was reported. The emitters possess a fast-decaying intermediate and a long-lived metastable state accessible from the first excited electronic state and optically reversible to the excited state(s) by means of a two-laser repumping scheme. This results in a nonlinear photo-emission behavior of these emitters which produces enhanced photoluminescence and reduced saturation intensity. Beyond the intriguing photo-physics of these emitters, it was demonstrated that their unique properties can be harnessed to realize a new modality of far-field, super-resolution imaging with a dual-doughnut-beam configuration. Sub-diffraction resolution of $\sim (63 \pm 4)$ nm was achieved. It is envisioned that this technique could be extended to other stable single emitters in 1D, 2D and 3D material hosts, as well as other fluorophores used for super-resolution nanoscopy. The impact of these findings is twofold. They deepen the current understanding of the photo-physics of quantum emitters in layered hBN, as well as show new potential ways of harnessing their nonlinear optical properties for specific applications such as the hereby presented sub-diffraction nanoscopy.

Chapter 7

Conclusion and outlook

7.1 Summary

In this thesis quantum emitters in diamond and hBN have been investigated for sensing applications. In this regard, the presented works can be separated into two parts. Developing a nanofabrication technique for assembly of nanodiamonds containing NV centers which act as quantum sensors for magnetic measurement and study of single photon sources in hBN as a promising candidates for sensing and high resolution imaging.

The superiority of NV centers in magnetic sensing has been demonstrated in few studies and even their industrial applications are not very far ahead. However, methods for fabrication of devices based on nanodiamonds containing NV centers are extensively being pursued. To date, various approaches for assembly of nanodiamonds have been reported and here a facile, robust and generic assembly of nanodiamonds based on EBID and covalent crosslinking, has been demonstrated. This method offers a few benefits. As the position is defined through EBID, the immediate advantages come from the possibility of direct writing. This can be interpreted as simplicity of the method in assembly of nanodiamonds in specific position within the resolution limitation of the assembly. The other benefits is forming

the covalent bond between the nanodiamond and substrate which is very important when the positioned nanodiamonds need to withstand multiple fabrication steps to fabricate the device. In addition, although in this work, nanodiamonds were used for assembly, there is no limitation in implementing the method for other nanoparticles or substrate. As an example, the possibility of using Si_3N_4 as a substrate for assembly of nanodiamonds has been shown. It must be noted that the method yields more than 90 percents attachment efficiency.

In the other part of this thesis, quantum emitters in hBN have been used for sensing and high resolution imaging. It has been shown that the emitters are robust and can withstand temperatures as high as 800 K, the highest operating temperature reported for a quantum emitter. In order to do this measurement, a custom chamber setup was designed and built. The unique setup is capable of measuring PL above room temperature up to 1000 $°C$. Using this chamber, the photoluminescence of quantum emitters in hBN above room temperature has been studied extensively in this work. It was found that some emitters undergo permanent changes at high temperatures (i.e. bleaching or losing quantum characteristic). On the other hand, some emitters were quite robust and were fluorescent during heating or cooling cycle. The changes of the photoluminescence as a result of temperature was studied and modeled for these emitters. PL emission was red-shifted and the ZPL was broadened at higher temperature due to the lattice expansion and phonon interactions, respectively. Interestingly, the single photon purity of the quantum emitters remained constant within the measured temperatures. This in not expected in quantum emitters as often the deshelving process is facilitated at higher temperatures, preventing emission due to domination of non-radiative decay. The measurement conducted here, suggests that the energy barrier as well as rates into the deshelving state for emitters in hBN allows the operation at elevated temperatures. The results not only suggest the hBN quantum emitters for temperature sensing, but point out the potential application of these emitters at higher temperatures. The latter depends on behavior of the emitters in hBN with environment which has not been investigated here or elsewhere to the best of my knowledge.

Finally, the high resolution images of quantum emitters in hBN are shown for the first time in this thesis. The possibility of identifying the emitters in hBN is crucial in many applications such as photonic devices or sensing applications where the position of the emitters needs to be acquired beyond diffraction limit. So far, this was not considered a problem for quantum emitters in solid states as the host nanomaterials could be imaged with techniques such as electron microscopes. However, in case of hBN, device fabrication by simple transferring of the host 2D material, cannot be considered as an advantage for nano-size flakes. Hence, an alternative technique for determining the location of emitters is ideal. Although this can be in principle be done through image processing, direct imaging is more desirable. The study here confirms the possibility of far field high resolution optical imaging of quantum emitters in hBN which so far only has been shown with single NV center in diamond. Here, the photophysical properties of the emitters have been studied under different illumination conditions to achieve high resolution images from quantum emitters in hBN. The new modality of GSD microscopy technique has been proposed for obtaining better resolution based on photophysics of the emitters. In addition to necessity of high resolution imaging with hBN quantum emitters, the potential application of hbN emitters in biology is suggested, where the main application of high resolution techniques is proposed.

7.2 Future directions

In this section the possible future works are discussed. These suggestions are based on further extrapolation of the studies here in my opinion, otherwise one might come up with other directions.

In case of self-assembly technique, the main question that yet is to be answered is that how efficient the process is in single particle positioning. For the work here, nanodiamonds with ensembles of NV center were used which in practice made it impossible to reliably determine the single particle attachment efficiency. This is

very important in applications such as sensing or coupling into cavities where having a nanodiamond with single NV center is more favorable. If a nanodiamond contains single NV center, then the single particles attachment can be inferred from autocorrelation measurements conveniently. However, the difficulty in determining the single particle attachment is also limited by the number of nanodiamond particles with single NV center in the solution. The available nanodiamonds solutions contain mixture of nanodiamonds with 1 or more NV centers. As a result, single particle attachment cannot be obtained directly from autocorrelation measurement and other factors such as number of nanodiamonds with single NV in the solution must be taken into account. Moreover, the resolution of the technique is another crucial factor. Although EBID is capable of producing depositions down to tens of nanometer, the resolution of the assembly process might be limited to nanodiamond agglomeration, proximity effect from secondary electrons. It is also interesting to explore the assembly technique for other applications such as fluorescent particle attachment or attachment on a non flat surface where other techniques face difficulties.

For emitters in hBN, certainly more works needs to be done. The stability of the emitters at high temperature is a promising property indicating the suitability of using these emitters for sensing applications particularly above room temperature. More importantly, here only temperature sensing was proposed however, other physical quantities such as strain or magnetic field can be studied both fundamentally and experimentally in future. The first demonstration of high resolution imaging of quantum emitters in hBN will open up new avenue for employing them in fields such as biology and cell imaging. Still, the fundamental studies of the electronic structure and further improvement in the resolution are definitely on the checklist of high resolution imaging of these emitters. Obtaining the system inter crossing rates through pump-probe measurement gives the essential information needed for direct imaging of the emitters using a pulse sequence scheme such as the one used for NV centers [92]. It is also interesting to study imaging of ensembles of emitters in hBN and investigate the minimum possible resolvable distance of two emitters with

proposed supre-resolution technique. In this regard, the major issue to be solved first, is the variation in quantum emitters in hBN. These variations are attributed to the origin or the local environment of the defects which make it difficult to separate and study ensembles of same emitter. However, once the origin of the emitters are understood, one can further investigate the super-resolution imaging of ensembles in hBN.

Appendix A

Schematic of HT PL chamber

In order to perform the PL measurement at conditions other than ambient, a chamber was desined and build. The dimensions of the chamber is shown in figure A.1(a). Connection on the chamber is ISO NW standard for vacuum connections. Using a Tourbo molecular pump (TMP), base vacuum of $\sim 1 \times 10^{-6}$ mbar .In principle the chamber can be installed on any confocal setups on optical tables. Furthermore, it needs to be mounted on an XYZ translational stage if an specific spot on the sample needs to be measured. Although not tried in this thesis, it is possible to introduced various gases and investigate photoluminescence properties of a quantum emitter at different environment in-situ. Temperature in the chamber is measured and monitored with k-type thermocouple. Thermocouple is mounted on top of substrate to get accurate reading of temperature. This is very critical specially for measurement gaseous environment where the heat transfer by convection can affect the real temperature on the sample. Heating is provided by a boron nitride heater. The type of heater which is used, operates in vacuum condition up to 1000 $^{\circ}C$. .A thin quartz window mounted on the chamber is the pathway for optical excitation and collection of light. It must be noted that this is not the optimal solution as will distort the focal spot of the objective lens but the easiest way do the measurement. Figure A.1(b) shows the assembly of the environmental chamber.

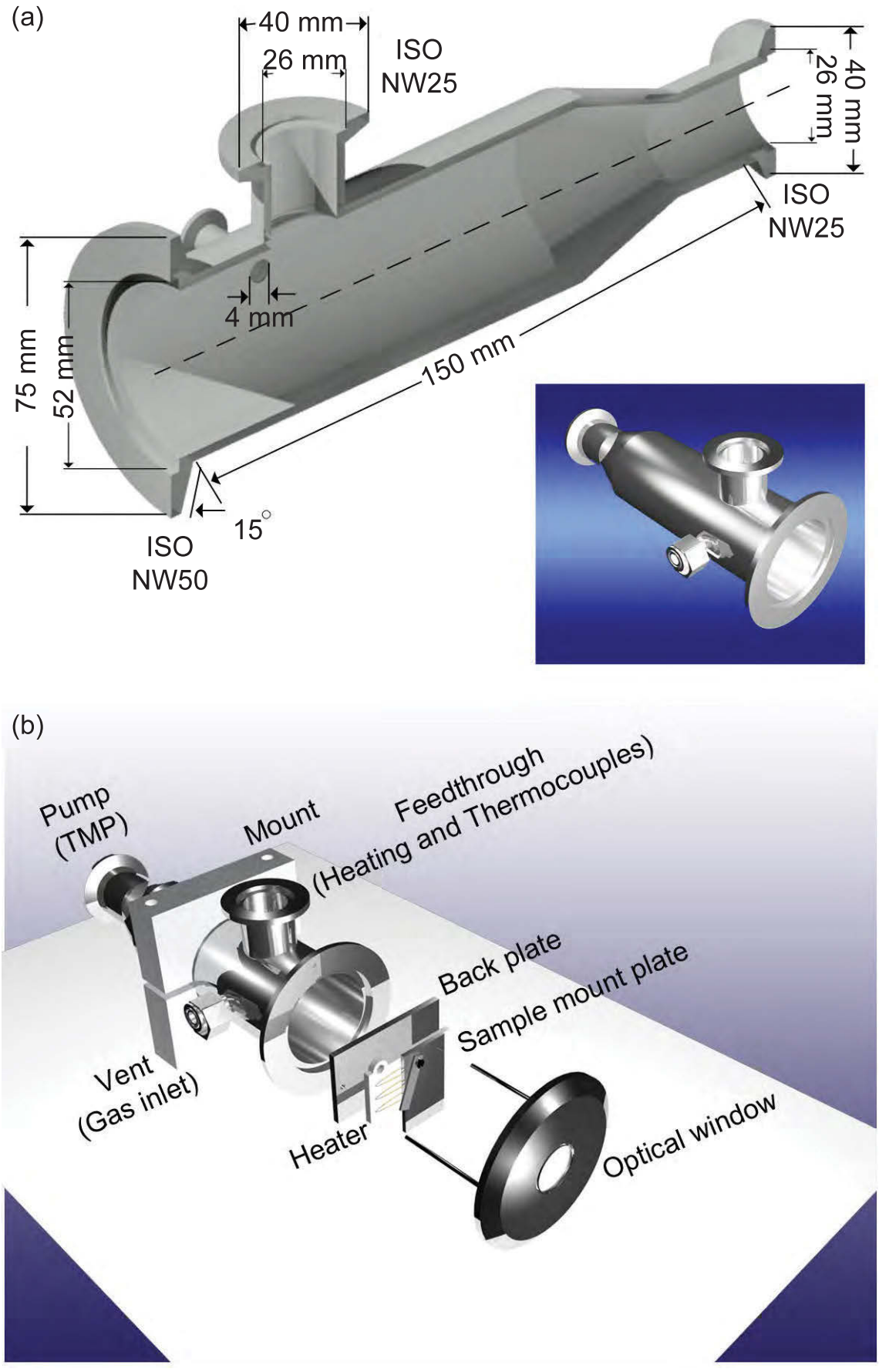

FIGURE A.1: high temperature chamber

Appendix B

Igor pro Procedures for data analysis

B.1 Loading PHD file from picoharp 300

The following procedure written in *Igor pro version 6* software, enable direct loading of the time tagged data from picoharp 300 (It has been converted from the *Matlab* code provided by the manufacturer). The graphic user interface (GUI) function will create a menu in the *Igor pro* software prompting the user whether the selected data is a correlation measurements or time-resolved data. After loading, data is normalized, fitted and plotted for further analysis if needed. In this procedure, autocorrelation data is fitted with a 3-level model and the fitting parameters will be displayed in the plot:

```
#pragma rtGlobals=3      // Use modern global access method
    and strict wave access.


Function/S LoadPHD(PHDfile)
String PHDfile
```

```
Variable refNum
String Ident, FormatVersion, CreatorName, CreatorVersion,
   FileTime
String CRLF, Comment
Variable NumberOfCurves, BitsPerHhistoBin, RoutingChannels,
    NumberOfBoards, ActiveCurve
Variable MeasurementMode, SubMode, RangeNo, OffSet, Tacq,
   StopAt, StopOnOvfl
Variable Restart, DispLinLog, DispTimeAxisFrom,
   DispTimeAxisTo, DispCountAxisFrom, DispCountAxisTo
String message = "Select a file"
String outputPath, fileHandle
#if(NumberByKey("IGORVERS",IgorInfo(0)) >= 6.1)
String fileFilters = "PicoHarp Data Files (*.phd):.phd;"
fileFilters += "All Files:.*;"
Open /D /R /F=fileFilters /M=message refNum
#else
Open /D /R /T=".phd" /M=message refNum
#endif

outputPath = S_fileName
printf "%s\r" outputPath
Open /R refNum as  outputPath
fileHandle = ParseFilePath(5, outputPath, ":", 0,0)
fileHandle = ParseFilePath(3, outputPath, ":", 0,0)
printf "%s\r" fileHandle

// Ascii file header

FReadLine /N=16 refNum , Ident
FreadLine /N=6 refNum, FormatVersion
FreadLine /N=18 refNum, CreatorName
FreadLine /N=12 refNum, CreatorVersion
FreadLine /N=18 refNum, FileTime
FreadLine /N=2 refNum, CRLF
FreadLine /N=256 refNum, Comment

// Binary file header
FBinRead /F=3 refNum, NumberOfCurves
```

```
FBinRead /F=3 refNum, BitsPerHhistoBin
FBinRead /F=3 refNum, RoutingChannels
FBinRead /F=3 refNum, NumberOfBoards
FBinRead /F=3 refNum, ActiveCurve
FBinRead /F=3 refNum, MeasurementMode
FBinRead /F=3 refNum, SubMode
FBinRead /F=3 refNum, RangeNo
FBinRead /F=3 refNum, OffSet
FBinRead /F=3 refNum, Tacq
FBinRead /F=3 refNum, StopAt
FBinRead /F=3 refNum, StopOnOvfl
FBinRead /F=3 refNum, Restart
FBinRead /F=3 refNum, DispLinLog
FBinRead /F=3 refNum, DispTimeAxisFrom
FBinRead /F=3 refNum, DispTimeAxisTo
FBinRead /F=3 refNum, DispCountAxisFrom
FBinRead /F=3 refNum, DispCountAxisTo

Variable i, DispCurveMapTo, DispCurveShow
for(i=1;i<=8;i+=1)
FBinRead /F=3 refNum, DispCurveMapTo
FBinRead /F=3 refNum, DispCurveShow

Variable j, ParamStart, ParamStep, ParamEnd
for(j=1;j<=3;j+=1)
FBinRead /F=3 refNum, ParamStart
FBinRead /F=3 refNum, ParamStep
FBinRead /F=3 refNum, ParamEnd
endfor

Variable RepeatMode, RepeatsPerCurve, RepeatTIme,
   RepeatWaitTime
String ScriptName
FBinRead /F=3 refNum, RepeatMode
FBinRead /F=3 refNum, RepeatsPerCurve
FBinRead /F=3 refNum, RepeatTIme
FBinRead /F=3 refNum, RepeatWaitTime
FReadLine /N=20 refNum, ScriptName
```

```
Variable k
String HardwareIdent, HardwareVersion
Variable HardwareSerial, SyncDivider, CFDZeroCross0,
   CFDLevel0, CFDZeroCross1, CFDLevel1, Resolution
Variable RouterModelCode, RouterEnabled, RtChan1_InputType,
    RtChan1_InputLevel, RtChan1_InputEdge
Variable RtChan1_CFDPresent, RtChan1_CFDLevel,
   RtChan1_CFDZeroCross
Variable RtChan2_InputType, RtChan2_InputLevel,
   RtChan2_InputEdge
Variable RtChan2_CFDPresent, RtChan2_CFDLevel,
   RtChan2_CFDZeroCross
Variable RtChan3_InputType, RtChan3_InputLevel,
   RtChan3_InputEdge
Variable RtChan3_CFDPresent, RtChan3_CFDLevel,
   RtChan3_CFDZeroCross
Variable RtChan4_InputType, RtChan4_InputLevel,
   RtChan4_InputEdge
Variable RtChan4_CFDPresent, RtChan4_CFDLevel,
   RtChan4_CFDZeroCross

for(k=1;k<=NumberOfBoards;k+=1)
FReadLine /N=16 refNum, HardwareIdent
FReadLine /N=8 refNum, HardwareVersion
FBinRead /F=3 refNum, HardwareSerial
FBinRead /F=3 refNum, SyncDivider
FBinRead /F=3 refNum, CFDZeroCross0
FBinRead /F=3 refNum, CFDLevel0
FBinRead /F=3 refNum, CFDZeroCross1
FBinRead /F=3 refNum, CFDLevel1
FBinRead /F=4 refNum, Resolution
FBinRead /F=3 refNum, RouterModelCode
FBinRead /F=3 refNum, RouterEnabled
//Router Ch1
FBinRead /F=3 refNum, RtChan1_InputType
FBinRead /F=3 refNum, RtChan1_InputLevel
FBinRead /F=3 refNum, RtChan1_InputEdge
FBinRead /F=3 refNum, RtChan1_CFDPresent
FBinRead /F=3 refNum, RtChan1_CFDLevel
```

```
FBinRead /F=3 refNum, RtChan1_CFDZeroCross
//Router Ch2
FBinRead /F=3 refNum, RtChan2_InputType
FBinRead /F=3 refNum, RtChan2_InputLevel
FBinRead /F=3 refNum, RtChan2_InputEdge
FBinRead /F=3 refNum, RtChan2_CFDPresent
FBinRead /F=3 refNum, RtChan2_CFDLevel
FBinRead /F=3 refNum, RtChan2_CFDZeroCross
//Router Ch3
FBinRead /F=3 refNum, RtChan3_InputType
FBinRead /F=3 refNum, RtChan3_InputLevel
FBinRead /F=3 refNum, RtChan3_InputEdge
FBinRead /F=3 refNum, RtChan3_CFDPresent
FBinRead /F=3 refNum, RtChan3_CFDLevel
FBinRead /F=3 refNum, RtChan3_CFDZeroCross
//Router Ch4
FBinRead /F=3 refNum, RtChan4_InputType
FBinRead /F=3 refNum, RtChan4_InputLevel
FBinRead /F=3 refNum, RtChan4_InputEdge
FBinRead /F=3 refNum, RtChan4_CFDPresent
FBinRead /F=3 refNum, RtChan4_CFDLevel
FBinRead /F=3 refNum, RtChan4_CFDZeroCross
endfor

//*****************************************
// Headers for each histogram (curve)
//Intialize temporary arrays (waves)
//*****************************************

Make /D /N=(NumberOfCurves) /O CurveIndexWave
Make /D /N=(NumberOfCurves) /O ResolutionWave
Make /D /N=(NumberOfCurves) /O ChannelsWave
Make /D /N=(NumberOfCurves) /O IntegralCountWave
Make /D /N=(NumberOfCurves) /O DataOffsetWave
Make /D /N=(NumberOfCurves) /O PeakWave

Variable l
Variable CurveIndex, TimeOfRecording, RoutingChannel,
   ExtDevices, MeasMode
```

```
Variable P1, P2, P3, Channels, StopAfter, StopReason,
   InpRate0, InpRate1, HistCountRate
Variable IntegralCount, IntegralCount2, Reserved,
   DataOffset, RtChan_InputType, RtChan_InputLevel,
   RtChan_InputEdge
Variable RtChan_CFDPresent, RtChan_CFDLevel,
   RtChan_CFDZeroCross

for(l=1;l<= NumberOfCurves;l+=1)
FBinRead /F=3 refNum, CurveIndex
CurveIndexWave[l-1] = CurveIndex

FBinRead /F=3 /U refNum, TimeOfRecording
TimeOfRecording = TimeOfRecording+2082844800
 Secs2Time(TimeOfRecording,1)
FReadLine /N=16 refNum, HardwareIdent
FReadLine /N=8 refNum, HardwareVersion
FBinRead /F=3 refNum, HardwareSerial
FBinRead /F=3 refNum, SyncDivider
FBinRead /F=3 refNum, CFDZeroCross0
FBinRead /F=3 refNum, CFDLevel0
FBinRead /F=3 refNum, CFDZeroCross1
FBinRead /F=3 refNum, CFDLevel1
FBinRead /F=3 refNum, Offset
FBinRead /F=3 refNum, RoutingChannel
FBinRead /F=3 refNum, ExtDevices
FBinRead /F=3 refNum, MeasMode
FBinRead /F=3 refNum, SubMode
FBinRead /F=4 refNum, P1
FBinRead /F=4 refNum, P2
FBinRead /F=4 refNum, P3
FBinRead /F=3 refNum, RangeNo
FBinRead /F=4 refNum, Resolution
printf "                Resolution: %2.6g ns\r" Resolution
ResolutionWave[l-1] = Resolution

FBinRead /F=3 refNum, Channels
ChannelsWave[l-1] = Channels
FBinRead /F=3 refNum, Tacq
```

```
FBinRead /F=3 refNum, StopAfter
FBinRead /F=3 refNum, StopReason
FBinRead /F=3 refNum, InpRate0
FBinRead /F=3 refNum, InpRate1
FBinRead /F=3 refNum, HistCountRate
FBinRead /F=3/U refNum, IntegralCount
FBinRead /F=3/U refNum, IntegralCount2

if(IntegralCount2 == 0)
printf "                Integral Count: %5.0f\r"
   IntegralCount
IntegralCountWave[l-1] = IntegralCount
else
IntegralCount2 = IntegralCount2 * (2.^32) + IntegralCount
printf "                Integral Count: %5.0f\r"
   IntegralCount2
IntegralCountWave[l-1] = IntegralCount2
endif

FBinRead /F=3 refNum, Reserved
FBinRead /F=3 refNum, DataOffset
DataOffsetWave[l-1] = DataOffset

FBinRead /F=3 refNum, RouterModelCode
FBinRead /F=3 refNum, RouterEnabled
FBinRead /F=3 refNum, RtChan_InputType
FBinRead /F=3 refNum, RtChan_InputLevel
FBinRead /F=3 refNum, RtChan_InputEdge
FBinRead /F=3 refNum, RtChan_CFDPresent
FBinRead /F=3 refNum, RtChan_CFDLevel
FBinRead /F=3 refNum, RtChan_CFDZeroCross
endfor

//************************************************
//Normalization and fitting with 3-level model
//************************************************

Variable m, dumCount,delaytime
Variable Startscale
```

```
String dummy
for(m=1; m <= NumberOfCurves; m+= 1)
dummy = fileHandle + "_"+ num2str(m-1)
dumCount = ChannelsWave[m-1]
delaytime=(ResolutionWave[m-1]*ChannelsWave[m-1])-95
Make /D /O /N=(dumCount) $dummy
FSetPos refNum, DataOffsetWave[m-1]
FBinRead /U /F=3 refNum, $dummy
wavestats/Q $dummy
String autocorr="G2"
String outputname
if(cmpstr(what,autocorr)==0)

if(m-1 == 0)
Variable cnt= ResolutionWave[m-1]/1000000000*InpRate0*
   InpRate1*StopAfter/1000
outputname =  fileHandle +"_norm"
Duplicate/O $dummy,$outputname
Wave output = $outputname
output = output/cnt
wavestats/Q output
startscale=V_minRowloc*ResolutionWave[m-1]*-1
SetScale /P x, Startscale, ResolutionWave[m-1], "", output
Display output as fileHandle+"_norm"
SetAxis bottom -95,95
ModifyGraph mirror=2,manTick(left)={0,0.5,0,1},manMinor(
   left)={0,50};DelayUpdate
ModifyGraph manTick(bottom)={0,40,0,0},manMinor(bottom)
   ={0,50};DelayUpdate
Label left "g\\S2\\M(\\F'Symbol't)"
Label bottom "Delaytime (ns)"
Make/O fitparameters={0.5,0.5,1,2,15}
FuncFit/N/Q g2, fitparameters, output[550,17000]/D
Legend/C/N=text0/F=0/S=1/A=MC
Variable/G g0=g2(fitparameters,0)
```

```
String Summary="Coefficient values\rA = "+num2str(
   fitparameters[0])+"\rB = "+num2str(fitparameters[1])+"\
   rC = "+num2str(fitparameters[2])+"\r\\F'Symbol't\M\F'
   Arial'\B1\M = "+num2str(fitparameters[3])+"\r\\F'Symbol'
   t\M\F'Arial'\B2\M = "+num2str(fitparameters[4])
Textbox/A=RB/C/N=text0 summary
String/G Summary2="g\S2\M(0) = "+num2str(g0)
Textbox/A=MB/C/N=text1/F=0 summary2
else
AppendToGraph $dummy
endif

#if(NumberByKey("IGORVERS",IgorInfo(0))>= 6.1)
PeakWave[m-1] = WaveMax($dummy)
#else
wavestats $dummy
PeakWave[m-1] = V_max
#endif

else

//*********************************************
//Reading and normilizing lifetime
//*********************************************

startscale=V_maxRowloc*ResolutionWave[m-1]*-1
SetScale /P x, startscale, ResolutionWave[m-1], $dummy
wavestats/Q output       //normalizing to max
Variable maximum=V_max
Variable Xmax=V_maxRowLoc
Variable endpnt=V_npnts
outputname= fileHandle +"_norm"
Duplicate/O $dummy,$outputname
Wave output = $outputname
output=output/maximum
output = output ==0  ? NaN : output
wavetransform zapNaNs output
wavestats/Q output
```

```
Display output as fileHandle+"_norm"
Label left "PL intensity (Norm.)"
Label bottom "Decey time (ns)"
SetAxis/A left
Curvefit /N/W=0 dblexp_XOffset output[Xmax,]  /D
ModifyGraph log(left)=1
Wave fitresult=w_coef
Variable tau1,tau2
tau1=fitresult[2]
tau2=fitresult[4]
String Summary1="\\F'Symbol't\M\F'Arial'\B1\M = "+num2str(
   tau1)+"\r\\F'Symbol't\M\F'Arial'\B2\M ="+num2str(tau2)
Textbox/A=RT/C/N=text0 summary1
ModifyGraph width=216,height=144
ModifyGraph mirror=2
endif
endfor

KillWaves /Z  CurveIndexWave, ResolutionWave, ChannelsWave,
    IntegralCountWave, DataOffsetWave, PeakWave
Close refNum
return outputPath
End

Function PicoharpLoader() //GUI for Picoharp
String chosendata
prompt chosendata, "Lifetime or G2",popup, Addlistitem ("
   Lifetime","G2")
doprompt "Picoharp  (*.PHD files only)", chosendata

if (V_flag)
Abort "Cancelled by user...."
else
LoadPHD(chosendata)
endif
End

Menu "Photonic"      //Creat a menu in Igor pro
"PicoharpLoader"
```

```
End
```

B.2 Igor procedure for Loading Spe file (datafile from spectrometer software)

The following procedure for *Igor Pro version 6*, will load .spe file. spe datafile is a common format for spectroscopy software (specifically *Winspec*). The GUI will add a menu in *Igor pro*. The other function in the procedure can be called to normalize the spectrum data.

```
Function SpeLoader()

Variable refnum
Variable exp_sec
Variable nx, ny, nframes, datatype
String wname
String wnameX, wnameY
String datestr, timestr, comment1, comment2, comment3,
   comment4, comment5
String notestr, wavenote=""

open/r/Z=2/M="Press cancel if you're finished"/t=".spe"
   refnum as ""
if (V_flag!=0)
abort "abort"
endif

FStatus refnum
wname=S_fileName[0,((strlen(S_fileName)-1)-4)]
wname = Cleanupname(wname,0)
FSetPos refnum, 10; FBinRead/B=3/F=4 refnum,exp_sec //
   exposure in seconds
FSetPos refnum, 42; FbinRead/B=3/F=2 refnum, nx //number of
    x pixels
```

```
FSetPos refnum, 656; FbinRead/B=3/F=2 refnum, ny //number
   of y pixels (=1 for graph)
FSetPos refnum, 1446; FbinRead/B=3/F=3 refnum, nframes //
   number of frames
FSetPos refnum, 108; FbinRead/B=3/F=2 refnum, datatype
FSetPos refnum, 20; FReadLine/N=10 refnum, datestr
FSetPos refnum, 172; FReadLine/N=6 refnum, timestr
FSetPos refnum, 200; Freadline refnum, comment1
FSetPos refnum, 280; Freadline refnum, comment2
FSetPos refnum, 360; Freadline refnum, comment3
FSetPos refnum, 440; Freadline refnum, comment4
FSetPos refnum, 520; Freadline refnum, comment5

Variable glue, offset, scalefactor, final
FSetPos refnum, 76; FBinRead/B=3/F=2 refnum,glue
FSetPos refnum, 78; FBinRead/B=3/F=4 refnum,offset
FSetPos refnum, 82; FBinRead/B=3/F=4 refnum,final
FSetPos refnum, 90; FBinRead/B=3/F=4 refnum,scalefactor

Variable center, xpix, grooves
FSetPos refnum, 72; FBinRead/B=3/F=4 refnum,center
FSetPos refnum, 6; FBinRead/B=3/F=2 refnum,xpix
FSetPos refnum, 650; FBinRead/B=3/F=4 refnum,grooves

Variable polyx,offsetx, scalex0, scalex1, scalex2
FSetPos refnum, 3101; FBinRead/B=3/F=1 refnum,polyx
FSetPos refnum, 3183; FBinRead/B=3/F=5 refnum,offsetx
FSetPos refnum, 3263; FBinRead/B=3/F=5 refnum,scalex0
FSetPos refnum, 3271; FBinRead/B=3/F=5 refnum,scalex1
FSetPos refnum, 3279; FBinRead/B=3/F=5 refnum,scalex2
Close refnum

switch(datatype)
case 0:
GBLoadWave/O/Q/B=3/S=4100/T={2,4}/U=(nx*ny*nframes)/W=(1)/N
   =WStemp (S_path+S_filename)
break
case 1:
```

```
GBLoadWave/O/Q/B=3/S=4100/T={32,4}/U=(nx*ny*nframes)/W=(1)/
   N=WStemp (S_path+S_filename)
break
case 2:
GBLoadWave/O/Q/B=3/S=4100/T={16+64,4}/U=(nx*ny*nframes)/W
   =(1)/N=WStemp (S_path+S_filename)
break
case 3:
GBLoadWave/O/Q/B=3/S=4100/T={16+64,4}/U=(nx*ny*nframes)/W
   =(1)/N=WStemp (S_path+S_filename)
break
default:
abort "Unknown datatype"
endswitch

Wave wstemp0
if (ny>1)
if (nframes == 1)
redimension/N=(nx,ny) WStemp0
else
redimension/N=(nx,ny, nframes) WStemp0
endif
endif
if (glue==1)
Setscale/P x, offset*1E-9, scalefactor*1E-9, "m", WStemp0
else
if(polyx==2)
String Calibx = wname + "_x"
Make/D/O/N = (xpix) $calibx = scalex0 + scalex1*(p+1) +
   scalex2*(p+1)^2
else
Print "Special Calibration - scale not made: polynomial
   order", polyx
endif
endif
Duplicate/O WStemp0, $wname
KillWaves/Z WStemp0
sprintf notestr, "File: %s\r", S_Filename ;wavenote+=
   notestr
```

```
sprintf notestr, "Path: %s\r", S_Path ;wavenote+=notestr
sprintf notestr, "Exposure: %g\r", exp_sec ;wavenote+=
   notestr
sprintf notestr, "Grating: %g\r", grooves ;wavenote+=
   notestr
sprintf notestr, "Frames: %g\r", nframes ;wavenote+=notestr
sprintf notestr, "Captured: %s %s\r", DateStr , TimeColon(
   Timestr) ;wavenote+=notestr
sprintf notestr, "Comment: %s -- %s -- %s -- %s -- %s\r",
   Comment1,Comment2,Comment3,Comment4,Comment5
wavenote+=notestr
Note $wname, wavenote
End

Menu "Photonic" \\Creat a menue in Igor
"SpeLoader"
End

Function Normalizespec(input,plot)       //Normalized an
   spectrum
Wave input
Variable plot
wavestats/Q input
Variable startpoint,endpoint
endpoint = v_npnts
startpoint = v_npnts - 100
wavestats/Q/R=[startpoint,endpoint] input
Variable avgvalue = V_avg
String outputname = nameofwave(input)+"_norm"
Duplicate/O input,$outputname
Wave output = $outputname
output = output-avgvalue
wavestats/Q output
output = output/V_max
String xwaves=wavelist("*wavelength*",";","")
String x_spec=stringfromlist(0,xwaves)
String Graphname="Spectrum0"
if(plot==1)  //graph in different plots
Display /N=$graphname output vs $x_spec
```

```
elseif(plot>1)  //graph in single plot
Appendtograph /W=Spectrum0 output vs $x_spec
endif
ModifyGraph width=216,height=144
ModifyGraph mirror=2,manTick(left)={0,0.5,0,1},manMinor(
   left)={0,50};DelayUpdate
ModifyGraph manTick(bottom)={0,40,0,0},manMinor(bottom)
   ={0,50};DelayUpdate
Label left "Normalised intensity (a.u.)"
Label bottom "Wavelength (nm)"
SetAxis/A bottom
SetAxis/A left 0,1.1
End
```

Bibliography

[1] Christian L Degen, F Reinhard, and P Cappellaro. "Quantum sensing". In: *Reviews of modern physics* 89.3 (2017), p. 035002.

[2] IK Kominis et al. "A subfemtotesla multichannel atomic magnetometer". In: *Nature* 422.6932 (2003), p. 596.

[3] M Brownnutt et al. "Ion-trap measurements of electric-field noise near surfaces". In: *Reviews of modern Physics* 87.4 (2015), p. 1419.

[4] JM Taylor et al. "High-sensitivity diamond magnetometer with nanoscale resolution". In: *Nature Physics* 4.10 (2008), pp. 810–816.

[5] RC Jaklevic et al. "Macroscopic quantum interference in superconductors". In: *Physical Review* 140.5A (1965), A1628.

[6] RA Hoebe et al. "Controlled light-exposure microscopy reduces photobleaching and phototoxicity in fluorescence live-cell imaging". In: *Nature biotechnology* 25.2 (2007), p. 249.

[7] Stefan W Hell. "Far-field optical nanoscopy". In: *science* 316.5828 (2007), pp. 1153–1158.

[8] Sungkun Hong et al. "Nanoscale magnetometry with NV centers in diamond". In: *MRS bulletin* 38.2 (2013), pp. 155–161.

[9] Zhiliang Yuan et al. "Electrically driven single-photon source". In: *science* 295.5552 (2002), pp. 102–105.

[10] N Mizuochi et al. “Electrically driven single-photon source at room temperature in diamond”. In: *Nature photonics* 6.5 (2012), pp. 299–303.

[11] Yi Sun et al. “Room-temperature continuous-wave electrically injected InGaN-based laser directly grown on Si”. In: *Nature Photonics* 10.9 (2016), pp. 595–599.

[12] Theodore H Maiman. “Stimulated optical radiation in ruby”. In: *nature* 187.4736 (1960), pp. 493–494.

[13] HJ Mamin et al. “Nanoscale nuclear magnetic resonance with a nitrogen-vacancy spin sensor”. In: *Science* 339.6119 (2013), pp. 557–560.

[14] Matthias Leifgen et al. “Evaluation of nitrogen-and silicon-vacancy defect centres as single photon sources in quantum key distribution”. In: *New journal of physics* 16.2 (2014), p. 023021.

[15] O Fedorych et al. “Room temperature single photon emission from an epitaxially grown quantum dot”. In: *Applied Physics Letters* 100.6 (2012), p. 061114.

[16] Satoshi Kako et al. “A gallium nitride single-photon source operating at 200 K”. In: *Nature materials* 5.11 (2006), pp. 887–892.

[17] Christian Kurtsiefer et al. “Stable solid-state source of single photons”. In: *Physical review letters* 85.2 (2000), p. 290.

[18] Chunlang Wang et al. “Single photon emission from SiV centres in diamond produced by ion implantation”. In: *Journal of Physics B: Atomic, Molecular and Optical Physics* 39.1 (2005), p. 37.

[19] A Lohrmann et al. “Single-photon emitting diode in silicon carbide”. In: *Nature communications* 6 (2015), ncomms8783.

[20] Anthony J Morfa et al. “Single-photon emission and quantum characterization of zinc oxide defects”. In: *Nano letters* 12.2 (2012), pp. 949–954.

[21] Xuedan Ma et al. “Room-temperature single-photon generation from solitary dopants of carbon nanotubes”. In: *Nature nanotechnology* 10.8 (2015), pp. 671–675.

[22] Toan Trong Tran et al. “Quantum emission from defects in single-crystalline hexagonal boron nitride”. In: *Physical Review Applied* 5.3 (2016), p. 034005.

[23] Fengnian Xia et al. “Two-dimensional material nanophotonics”. In: *Nature Photonics* 8.12 (2014), pp. 899–907.

[24] Junpeng Lu et al. “Light–Matter Interactions in Phosphorene”. In: *Acc. Chem. Res* 49.9 (2016), pp. 1806–1815.

[25] FJ Alfaro-Mozaz et al. “Nanoimaging of resonating hyperbolic polaritons in linear boron nitride antennas”. In: *Nature Communications* 8 (2017), ncomms15624.

[26] Siyuan Dai et al. “Efficiency of launching highly confined polaritons by infrared light incident on a hyperbolic material”. In: *Nano Letters* 17.9 (2017), pp. 5285–5290.

[27] Weigao Xu et al. “Correlated fluorescence blinking in two-dimensional semiconductor heterostructures”. In: *Nature* 541.7635 (2017), pp. 62–67.

[28] Philipp Tonndorf et al. “On-chip waveguide coupling of a layered semiconductor single-photon source”. In: *Nano Letters* 17.9 (2017), pp. 5446–5451.

[29] Peter Lodahl, Sahand Mahmoodian, and Søren Stobbe. “Interfacing single photons and single quantum dots with photonic nanostructures”. In: *Reviews of Modern Physics* 87.2 (2015), p. 347.

[30] TT Tran et al. “Quantum emission from hexagonal boron nitride monolayers”. In: *Nature Nanotechnology* 11.1 (2016), pp. 37–37.

[31] AM Zaitsev. “Vibronic spectra of impurity-related optical centers in diamond”. In: *Physical Review B* 61.19 (2000), p. 12909.

[32] WV Smith et al. “Electron-spin resonance of nitrogen donors in diamond”. In: *Physical Review* 115.6 (1959), p. 1546.

[33] T Gaebel et al. “Photochromism in single nitrogen-vacancy defect in diamond”. In: *Applied Physics B* 82.2 (2006), pp. 243–246.

[34] L Rondin et al. “Magnetometry with nitrogen-vacancy defects in diamond”. In: *Reports on progress in physics* 77.5 (2014), p. 056503.

[35] Jeremy L O’brien, Akira Furusawa, and Jelena Vučković. “Photonic quantum technologies”. In: *Nature Photonics* 3.12 (2009), pp. 687–695.

[36] Lilian Childress and Ronald Hanson. “Diamond NV centers for quantum computing and quantum networks”. In: *MRS bulletin* 38.2 (2013), pp. 134–138.

[37] Jörg Wrachtrup and Fedor Jelezko. “Processing quantum information in diamond”. In: *Journal of Physics: Condensed Matter* 18.21 (2006), S807.

[38] Alexios Beveratos et al. “Single photon quantum cryptography”. In: *Physical review letters* 89.18 (2002), p. 187901.

[39] Romana Schirhagl et al. “Nitrogen-vacancy centers in diamond: nanoscale sensors for physics and biology”. In: *Annual review of physical chemistry* 65 (2014), pp. 83–105.

[40] Chi-Cheng Fu et al. “Characterization and application of single fluorescent nanodiamonds as cellular biomarkers”. In: *Proceedings of the National Academy of Sciences* 104.3 (2007), pp. 727–732.

[41] Felix Neugart et al. “Dynamics of diamond nanoparticles in solution and cells”. In: *Nano letters* 7.12 (2007), pp. 3588–3591.

[42] Katja Beha et al. “Optimum photoluminescence excitation and recharging cycle of single nitrogen-vacancy centers in ultrapure diamond”. In: *Physical review letters* 109.9 (2012), p. 097404.

[43] LJ Rogers et al. “Infrared emission of the NV centre in diamond: Zeeman and uniaxial stress studies”. In: *New Journal of Physics* 10.10 (2008), p. 103024.

[44] NRS Reddy, NB Manson, and ER Krausz. “Two-laser spectral hole burning in a colour centre in diamond”. In: *Journal of Luminescence* 38.1-6 (1987), pp. 46–47.

[45] A Gruber et al. “Scanning confocal optical microscopy and magnetic resonance on single defect centers”. In: *Science* 276.5321 (1997), pp. 2012–2014.

[46] Nitin Mohan et al. “Sub-20-nm Fluorescent Nanodiamonds as Photostable Biolabels and Fluorescence Resonance Energy Transfer Donors”. In: *Advanced materials* 22.7 (2010), pp. 843–847.

[47] JR Maze et al. “Nanoscale magnetic sensing with an individual electronic spin in diamond”. In: *Nature* 455.7213 (2008), p. 644.

[48] Gopalakrishnan Balasubramanian et al. “Nanoscale imaging magnetometry with diamond spins under ambient conditions”. In: *Nature* 455.7213 (2008), p. 648.

[49] Steffen Steinert et al. “High sensitivity magnetic imaging using an array of spins in diamond”. In: *Review of scientific instruments* 81.4 (2010), p. 043705.

[50] VM Acosta et al. “Diamonds with a high density of nitrogen-vacancy centers for magnetometry applications”. In: *Physical Review B* 80.11 (2009), p. 115202.

[51] S Steinert et al. “Magnetic spin imaging under ambient conditions with subcellular resolution”. In: *Nature communications* 4 (2013), p. 1607.

[52] GD Fuchs et al. “A quantum memory intrinsic to single nitrogen-vacancy centres in diamond”. In: *Nature Physics* 7.10 (2011), pp. 789–793.

[53] Janik Wolters et al. “Coupling of single nitrogen-vacancy defect centers in diamond nanocrystals to optical antennas and photonic crystal cavities”. In: *physica status solidi (b)* 249.5 (2012), pp. 918–924.

[54] Richard J Warburton. “Self-assembled semiconductor quantum dots”. In: *Contemporary Physics* 43.5 (2002), pp. 351–364.

[55] Mingming Jiang et al. “Reusable inorganic templates for electrostatic self-assembly of individual quantum dots, nanodiamonds, and lanthanide-doped nanoparticles”. In: *Nano letters* 15.8 (2015), pp. 5010–5016.

[56] Tao Zhang et al. “DNA-based self-assembly of fluorescent nanodiamonds”. In: *Journal of the American Chemical Society* 137.31 (2015), pp. 9776–9779.

[57] Nathan Chejanovsky et al. “Structural Attributes and Photodynamics of Visible Spectrum Quantum Emitters in Hexagonal Boron Nitride”. In: *Nano letters* 16.11 (2016), pp. 7037–7045.

[58] Toan Trong Tran et al. “Robust multicolor single photon emission from point defects in hexagonal boron nitride”. In: *ACS nano* 10.8 (2016), pp. 7331–7338.

[59] Romain Bourrellier et al. “Bright UV single photon emission at point defects in h-BN”. In: *Nano letters* 16.7 (2016), pp. 4317–4321.

[60] Mehdi Abdi et al. “Color centers in hexagonal boron nitride monolayers: A group theory and *ab initio* analysis”. In: *arXiv preprint, arXiv:1709.05414* (2017).

[61] Sherif Abdulkader Tawfik et al. “First-principles investigation of quantum emission from hBN defects”. In: *Nanoscale* 9 (2017), pp. 13575–13582.

[62] Gabriele Grosso et al. “Tunable and high-purity room temperature single-photon emission from atomic defects in hexagonal boron nitride”. In: *Nature Communications* 8.1 (2017), p. 705.

[63] Wolfgang Becker. *Advanced time-correlated single photon counting techniques*. Vol. 81. Springer Science & Business Media, 2005.

[64] Zav Shotan et al. “Photoinduced modification of single-photon emitters in hexagonal boron nitride”. In: *ACS Photonics* 3.12 (2016), pp. 2490–2496.

[65] Sumin Choi et al. “Engineering and localization of quantum emitters in large hexagonal boron nitride layers”. In: *ACS applied materials & interfaces* 8.43 (2016), pp. 29642–29648.

[66] Annemarie L Exarhos et al. “Optical signatures of quantum emitters in suspended hexagonal boron nitride”. In: *ACS nano* 11.3 (2017), pp. 3328–3336.

[67] Nicholas R. Jungwirth and Gregory D. Fuchs. “Optical Absorption and Emission Mechanisms of Single Defects in Hexagonal Boron Nitride”. In: *Phys. Rev. Lett.* 119 (5 2017), p. 057401.

[68] Nicholas R Jungwirth et al. “Temperature dependence of wavelength selectable zero-phonon emission from single defects in hexagonal boron nitride”. In: *Nano letters* 16.10 (2016), pp. 6052–6057.

[69] Kun Huang and Avril Rhys. “Theory of light absorption and non-radiative transitions in F-centres”. In: *Proc. R. Soc. Lond. A*. Vol. 204. 1078. The Royal Society. 1950, pp. 406–423.

[70] Tony Wilson and Colin Sheppard. *Theory and practice of scanning optical microscopy*. Vol. 180. Academic Press London, 1984.

[71] Hans Blom and Jerker Widengren. “Stimulated Emission Depletion Microscopy”. In: *Chemical Reviews* 117 (2017), pp. 7377–7427.

[72] Stefan W Hell. “Improvement of lateral resolution in far-field fluorescence light microscopy by using two-photon excitation with offset beams”. In: *Optics communications* 106.1-3 (1994), pp. 19–24.

[73] Stefan W Hell. *Topics in Fluorescence Spectroscopy*. Ed. by JR Lakowicz. Vol. 5. Plenum, New York, 1997.

[74] Stefan W Hell and Jan Wichmann. “Breaking the diffraction resolution limit by stimulated emission: stimulated-emission-depletion fluorescence microscopy”. In: *Optics letters* 19.11 (1994), pp. 780–782.

[75] Stefan W Hell and Matthias Kroug. “Ground-state-depletion fluorscence microscopy: A concept for breaking the diffraction resolution limit”. In: *Applied Physics B: Lasers and Optics* 60.5 (1995), pp. 495–497.

[76] Comert Kural et al. “Kinesin and dynein move a peroxisome in vivo: a tug-of-war or coordinated movement?” In: *Science* 308.5727 (2005), pp. 1469–1472.

[77] Thomas A Klar, Egbert Engel, and Stefan W Hell. "Breaking Abbe's diffraction resolution limit in fluorescence microscopy with stimulated emission depletion beams of various shapes". In: *Physical Review E* 64.6 (2001), p. 066613.

[78] Albert Einstein. "On the quantum theroy of radiation". In: *Phys. Z.* 18 (1917), pp. 121–128.

[79] Volker Westphal and Stefan W Hell. "Nanoscale resolution in the focal plane of an optical microscope". In: *Physical review letters* 94.14 (2005), p. 143903.

[80] Stefan W Hell. "Toward fluorescence nanoscopy". In: *Nature biotechnology* 21.11 (2003), p. 1347.

[81] Katrin I Willig et al. "STED microscopy with continuous wave beams". In: *Nature methods* 4.11 (2007), p. 915.

[82] Janina Hanne et al. "STED nanoscopy with fluorescent quantum dots". In: *Nature communications* 6 (2015), p. 7127.

[83] Yujia Liu et al. "Amplified stimulated emission in upconversion nanoparticles for super-resolution nanoscopy". In: *Nature* 543.7644 (2017), pp. 229–233.

[84] Eva Rittweger et al. "STED microscopy reveals crystal colour centres with nanometric resolution". In: *Nature Photonics* 3.3 (2009), pp. 144–147.

[85] Kyu Young Han et al. "Three-dimensional stimulated emission depletion microscopy of nitrogen-vacancy centers in diamond using continuous-wave light". In: *Nano letters* 9.9 (2009), pp. 3323–3329.

[86] Stefan Bretschneider, Christian Eggeling, and Stefan W Hell. "Breaking the diffraction barrier in fluorescence microscopy by optical shelving". In: *Physical review letters* 98.21 (2007), p. 218103.

[87] Elke Neu, Mario Agio, and Christoph Becher. "Photophysics of single silicon vacancy centers in diamond: implications for single photon emission". In: *Optics express* 20.18 (2012), pp. 19956–19971.

[88] Martin Berthel et al. "Photophysics of single nitrogen-vacancy centers in diamond nanocrystals". In: *Physical Review B* 91.3 (2015), p. 035308.

[89] Stefan W Hell. "Strategy for far-field optical imaging and writing without diffraction limit". In: *Physics Letters A* 326.1 (2004), pp. 140–145.

[90] E Rittweger, D Wildanger, and SW Hell. "Far-field fluorescence nanoscopy of diamond color centers by ground state depletion". In: *EPL (Europhysics Letters)* 86.1 (2009), p. 14001.

[91] Joanna Oracz et al. "Ground State Depletion Nanoscopy Resolves Semiconductor Nanowire Barcode Segments at Room Temperature". In: *Nano Letters* 17.4 (2017), p. 2652.

[92] Kyu Young Han et al. "Metastable dark states enable ground state depletion microscopy of nitrogen vacancy centers in diamond with diffraction-unlimited resolution". In: *Nano letters* 10.8 (2010), pp. 3199–3203.

[93] Robert H Webb. "Confocal optical microscopy". In: *Reports on Progress in Physics* 59.3 (1996), p. 427.

[94] Brahim Lounis and Michel Orrit. "Single-photon sources". In: *Reports on Progress in Physics* 68.5 (2005), p. 1129.

[95] MO Scully. "MS Zubairy Quantum Optics". In: *CambridgePress, London* (1997).

[96] J Bernard et al. "Photon bunching in the fluorescence from single molecules: A probe for intersystem crossing". In: *The Journal of chemical physics* 98.2 (1993), pp. 850–859.

[97] Alexios Beveratos et al. "Bunching and antibunching from single NV color centers in diamond". In: *Quantum communication, computing, and measurement 3*. Springer, 2002, pp. 261–267.

[98] Erwin L Hahn. "Spin echoes". In: *Physical review* 80.4 (1950), p. 580.

[99] A Dréau et al. "Avoiding power broadening in optically detected magnetic resonance of single NV defects for enhanced dc magnetic field sensitivity". In: *Physical Review B* 84.19 (2011), p. 195204.

[100] MW Beijersbergen et al. "Helical-wavefront laser beams produced with a spiral phaseplate". In: *Optics Communications* 112.5-6 (1994), pp. 321–327.

[101] NR Heckenberg et al. "Generation of optical phase singularities by computer-generated holograms". In: *Optics letters* 17.3 (1992), pp. 221–223.

[102] Patrice Genevet et al. "Ultra-thin plasmonic optical vortex plate based on phase discontinuities". In: *Applied Physics Letters* 100.1 (2012), p. 013101.

[103] Takeshi Watanabe et al. "Generation of a doughnut-shaped beam using a spiral phase plate". In: *Review of scientific instruments* 75.12 (2004), pp. 5131–5135.

[104] Ivo Utke, Patrik Hoffmann, and John Melngailis. "Gas-assisted focused electron beam and ion beam processing and fabrication". In: *Journal of Vacuum Science & Technology B: Microelectronics and Nanometer Structures Processing, Measurement, and Phenomena* 26.4 (2008), pp. 1197–1276.

[105] Milos Toth et al. "Nanostructure fabrication by ultra-high resolution environmental scanning electron microscopy". In: *Microscopy and Microanalysis* 13.S02 (2007), p. 1470.

[106] Markus Deubel et al. "Direct laser writing of three-dimensional photonic-crystal templates for telecommunications". In: *Nature materials* 3.7 (2004), pp. 444–447.

[107] Marco Esposito et al. "Nanoscale 3D chiral plasmonic helices with circular dichroism at visible frequencies". In: *ACS Photonics* 2.1 (2014), pp. 105–114.

[108] Christopher Elbadawi et al. "Electron beam directed etching of hexagonal boron nitride". In: *Nanoscale* 8 (36 2016), pp. 16182–16186.

[109] R Lariviere Stewart. "Insulating films formed under electron and ion bombardment". In: *Physical review* 45.7 (1934), p. 488.

[110] WF Van Dorp and Cornelis W Hagen. "A critical literature review of focused electron beam induced deposition". In: *Journal of Applied Physics* 104.8 (2008), p. 10.

[111] Esther Böhler, Jonas Warneke, and Petra Swiderek. "Control of chemical reactions and synthesis by low-energy electrons". In: *Chemical Society Reviews* 42.24 (2013), pp. 9219–9231.

[112] James Bishop et al. "Role of activated chemisorption in gas-mediated electron beam induced deposition". In: *Physical review letters* 109.14 (2012), p. 146103.

[113] Toby W Shanley et al. "Localized chemical switching of the charge state of nitrogen-vacancy luminescence centers in diamond". In: *Applied Physics Letters* 105.6 (2014), p. 063103.

[114] W Ding et al. "Mechanics of hydrogenated amorphous carbon deposits from electron-beam-induced deposition of a paraffin precursor". In: *Journal of Applied Physics* 98.1 (2005), p. 014905.

[115] I-Chen Chen et al. "Fabrication of high-aspect-ratio carbon nanocone probes by electron beam induced deposition patterning". In: *Nanotechnology* 17.17 (2006), p. 4322.

[116] JP Badey et al. "A comparative study of the effects of ammonia and hydrogen plasma downstream treatment on the surface modification of polytetrafluoroethylene". In: *Polymer* 37.8 (1996), pp. 1377–1386.

[117] Huang-Chung Cheng, Fang-Shing Wang, and Chun-Yao Huang. "Effects of NH/sub 3/plasma passivation on N-channel polycrystalline silicon thin-film transistors". In: *IEEE Transactions on Electron Devices* 44.1 (1997), pp. 64–68.

[118] ME Jones, JR Shealy, and JR Engstrom. "Thermal and plasma-assisted nitridation of GaAs (100) using NH_3". In: *Applied physics letters* 67.4 (1995), pp. 542–544.

[119] KR Lee, KB Sundaram, and DC Malocha. "Deposition parameters studies of silicon nitride films prepared by plasma-enhanced CVD process using silane-ammonia". In: *Journal of Materials Science: Materials in Electronics* 4.4 (1993), pp. 283–287.

[120] SE Hicks and RAG Gibson. "A spectroscopic investigation of growth regimes in silane-ammonia discharges used for plasma nitride deposition". In: *Plasma chemistry and plasma processing* 11.4 (1991), pp. 455–472.

[121] Ellen R Fisher. "A Review of Plasma-Surface Interactions During Processing of Polymeric Materials Measured Using the IRIS Technique". In: *Plasma Processes and Polymers* 1.1 (2004), pp. 13–27.

[122] Patrick R McCurdy et al. "Surface interactions of NH_2 radicals in NH_3 plasmas". In: *The Journal of Physical Chemistry B* 103.33 (1999), pp. 6919–6929.

[123] Greg T Hermanson. *Bioconjugate techniques*. Third edition. Academic press, 2013.

[124] Yuan Gao and Ilias Kyratzis. "Covalent immobilization of proteins on carbon nanotubes using the cross-linker 1-ethyl-3-(3-dimethylaminopropyl) carbodiimide—a critical assessment". In: *Bioconjugate Chemistry* 19.10 (2008), pp. 1945–1950.

[125] Deepak Sehgal and Inder K Vijay. "A method for the high efficiency of water-soluble carbodiimide-mediated amidation". In: *Analytical biochemistry* 218.1 (1994), pp. 87–91.

[126] Weijie Huang et al. "Attaching proteins to carbon nanotubes via diimide-activated amidation". In: *Nano Letters* 2.4 (2002), pp. 311–314.

[127] PingAn Hu et al. "Ultrasensitive detection of biomolecules using functionalized multi-walled carbon nanotubes". In: *Sensors and Actuators B: Chemical* 124.1 (2007), pp. 161–166.

[128] Yoon-Mee Lee et al. “Immobilization of horseradish peroxidase on multi-wall carbon nanotubes and its electrochemical properties”. In: *Biotechnology letters* 28.1 (2006), pp. 39–43.

[129] M Asunción Alonso-Lomillo et al. “Hydrogenase-coated carbon nanotubes for efficient H_2 oxidation”. In: *Nano letters* 7.6 (2007), pp. 1603–1608.

[130] Kuiyang Jiang et al. “Protein immobilization on carbon nanotubes via a two-step process of diimide-activated amidation”. In: *Journal of Materials Chemistry* 14.1 (2004), pp. 37–39.

[131] Yuzhou Wu et al. “Diamond quantum devices in biology”. In: *Angewandte Chemie International Edition* 55.23 (2016), pp. 6586–6598.

[132] C Santori et al. “Nanophotonics for quantum optics using nitrogen-vacancy centers in diamond”. In: *Nanotechnology* 21.27 (2010), p. 274008.

[133] Vitor R Manfrinato et al. “Controlled placement of colloidal quantum dots in sub-15 nm clusters”. In: *Nanotechnology* 24.12 (2013), p. 125302.

[134] Weiqiang Xie et al. “Nanoscale and Single-Dot Patterning of Colloidal Quantum Dots”. In: *Nano letters* 15.11 (2015), pp. 7481–7487.

[135] Ying Wang et al. “Capturing and depositing one nanoobject at a time: Single particle dip-pen nanolithography”. In: *Applied physics letters* 90.13 (2007), p. 133102.

[136] Patrick Maletinsky et al. “A robust scanning diamond sensor for nanoscale imaging with single nitrogen-vacancy centres”. In: *Nature nanotechnology* 7.5 (2012), pp. 320–324.

[137] Saleem G Rao et al. “Directed assembly of nanodiamond nitrogen-vacancy centers on a chemically modified patterned surface”. In: *ACS applied materials & interfaces* 6.15 (2014), pp. 12893–12900.

[138] Ashwin Gopinath et al. “Engineering and mapping nanocavity emission via precision placement of DNA origami”. In: *Nature* 535.7612 (2016), pp. 401–405.

[139] Paolo Andrich et al. “Engineered micro-and nanoscale diamonds as mobile probes for high-resolution sensing in fluid”. In: *Nano letters* 14.9 (2014), pp. 4959–4964.

[140] Tim Schroder et al. “Fiber-integrated diamond-based single photon source”. In: *Nano letters* 11.1 (2010), pp. 198–202.

[141] Jean-Philippe Tetienne et al. “Scanning nanospin ensemble microscope for nanoscale magnetic and thermal imaging”. In: *Nano letters* 16.1 (2016), pp. 326–333.

[142] Georg Kucsko et al. “Nanometre-scale thermometry in a living cell”. In: *Nature* 500.7460 (2013), pp. 54–58.

[143] Philipp Neumann et al. “High-precision nanoscale temperature sensing using single defects in diamond”. In: *Nano letters* 13.6 (2013), pp. 2738–2742.

[144] LP McGuinness et al. “Quantum measurement and orientation tracking of fluorescent nanodiamonds inside living cells”. In: *Nature nanotechnology* 6.6 (2011), pp. 358–363.

[145] Andreas W Schell et al. “Single defect centers in diamond nanocrystals as quantum probes for plasmonic nanostructures”. In: *Optics express* 19.8 (2011), pp. 7914–7920.

[146] Oliver Benson. “Assembly of hybrid photonic architectures from nanophotonic constituents”. In: *Nature* 480.7376 (2011), pp. 193–199.

[147] Olga Shimoni et al. “Development of a templated approach to fabricate diamond patterns on various substrates”. In: *ACS applied materials & interfaces* 6.11 (2014), pp. 8894–8902.

[148] Igor Aharonovich et al. “Bottom-up engineering of diamond micro-and nanostructures”. In: *Laser & Photonics Reviews* 7.5 (2013).

[149] Reinier W Heeres, Leo P Kouwenhoven, and Valery Zwiller. “Quantum interference in plasmonic circuits”. In: *Nature nanotechnology* 8.10 (2013), pp. 719–722.

[150] Marie-Christine Dheur et al. “Single-plasmon interferences”. In: *Science advances* 2.3 (2016), e1501574.

[151] Fenglin Liu et al. “Nanoscale plasmonic stamp lithography on silicon”. In: *ACS nano* 9.2 (2015), pp. 2184–2193.

[152] Michelle L Steen, Kristen R Kull, and Ellen R Fisher. “Comparison of surface interactions for NH and NH_2 on polymer and metal substrates during NH_3 plasma processing”. In: *Journal of applied physics* 92.1 (2002), pp. 55–63.

[153] Yuejiang Liang, Masaki Ozawa, and Anke Krueger. “A general procedure to functionalize agglomerating nanoparticles demonstrated on nanodiamond”. In: *ACS nano* 3.8 (2009), pp. 2288–2296.

[154] Anke Krüger et al. “Surface functionalisation of detonation diamond suitable for biological applications”. In: *Journal of Materials Chemistry* 16.24 (2006), pp. 2322–2328.

[155] Shu-Jung Yu et al. “Bright fluorescent nanodiamonds: no photobleaching and low cytotoxicity”. In: *Journal of the American Chemical Society* 127.50 (2005), pp. 17604–17605.

[156] Thaddeus D Ladd et al. “Quantum computers”. In: *Nature* 464.7285 (2010), pp. 45–53.

[157] Igor Aharonovich, Dirk Englund, and Milos Toth. “Solid-state single-photon emitters”. In: *Nature Photonics* 10.10 (2016), pp. 631–641.

[158] S Castelletto et al. “A silicon carbide room-temperature single-photon source”. In: *Nature materials* 13.2 (2014), pp. 151–156.

[159] I Aharonovich et al. “Diamond-based single-photon emitters”. In: *Reports on progress in Physics* 74.7 (2011), p. 076501.

[160] Guillaume Cassabois, Pierre Valvin, and Bernard Gil. “Hexagonal boron nitride is an indirect bandgap semiconductor”. In: *Nature Photonics* 10.4 (2016), pp. 262–266.

[161] Yi Lin and John W Connell. "Advances in 2D boron nitride nanostructures: nanosheets, nanoribbons, nanomeshes, and hybrids with graphene". In: *Nanoscale* 4.22 (2012), pp. 6908–6939.

[162] Zheng Liu et al. "Ultrathin high-temperature oxidation-resistant coatings of hexagonal boron nitride". In: *Nature communications* 4 (2013), p. 2541.

[163] Carmen Palacios-Berraquero et al. "Atomically thin quantum light-emitting diodes". In: *Nature communications* 7 (2016).

[164] Ki Kang Kim et al. "Synthesis of monolayer hexagonal boron nitride on Cu foil using chemical vapor deposition". In: *Nano letters* 12.1 (2011), pp. 161–166.

[165] Alexios Beveratos et al. "Nonclassical radiation from diamond nanocrystals". In: *Physical Review A* 64.6 (2001), p. 061802.

[166] Mark J Holmes et al. "Room-temperature triggered single photon emission from a III-nitride site-controlled nanowire quantum dot". In: *Nano letters* 14.2 (2014), pp. 982–986.

[167] Mark J Holmes et al. "Single photons from a hot solid-state emitter at 350 K". In: *ACS Photonics* 3.4 (2016), pp. 543–546.

[168] Yatendra Pal Varshni. "Temperature dependence of the energy gap in semiconductors". In: *physica* 34.1 (1967), pp. 149–154.

[169] Stefano Lagomarsino et al. "Robust luminescence of the silicon-vacancy center in diamond at high temperatures". In: *AIP Advances* 5.12 (2015), p. 127117.

[170] KS Novoselov et al. "2D materials and van der Waals heterostructures". In: *Science* 353.6298 (2016), aac9439.

[171] DN Basov, MM Fogler, and FJ García de Abajo. "Polaritons in van der Waals materials". In: *Science* 354.6309 (2016), aag1992.

[172] Sanfeng Wu et al. "Monolayer semiconductor nanocavity lasers with ultralow thresholds". In: *Nature* 520.7545 (2015), pp. 69–72.

[173] Pasqual Rivera et al. “Observation of long-lived interlayer excitons in monolayer MoSe 2–WSe 2 heterostructures”. In: *Nature communications* 6 (2015), p. 6242.

[174] Bin Yang et al. “Optical nanoscopy with excited state saturation at liquid helium temperatures”. In: *Nature Photonics* 9.10 (2015), pp. 658–662.

Books only

[63] Wolfgang Becker. *Advanced time-correlated single photon counting techniques*. Vol. 81. Springer Science & Business Media, 2005.

[70] Tony Wilson and Colin Sheppard. *Theory and practice of scanning optical microscopy*. Vol. 180. Academic Press London, 1984.

[73] Stefan W Hell. *Topics in Fluorescence Spectroscopy*. Ed. by JR Lakowicz. Vol. 5. Plenum, New York, 1997.

[123] Greg T Hermanson. *Bioconjugate techniques*. Third edition. Academic press, 2013.